Titre: Title:	Modeling of Thin Water Films on Swept Wings in Icing Condition
Auteur: Author:	Pierre Lavoie
Date:	2017
Type:	Mémoire ou thèse / Dissertation or Thesis
Référence: Citation:	Lavoie, P. (2017). Modeling of Thin Water Films on Swept Wings in Icing Condition [Master's thesis, École Polytechnique de Montréal]. PolyPublie. https://publications.polymtl.ca/2558/

Document en libre accès dans PolyPublie
Open Access document in PolyPublie

URL de PolyPublie: PolyPublie URL:	https://publications.polymtl.ca/2558/
Directeurs de recherche: Advisors:	Éric Laurendeau
Programme: Program:	Génie aérospatial

UNIVERSITÉ DE MONTRÉAL

MODELING OF THIN WATER FILMS ON SWEPT WINGS IN ICING CONDITION

PIERRE LAVOIE

DÉPARTEMENT DE GÉNIE MÉCANIQUE

ÉCOLE POLYTECHNIQUE DE MONTRÉAL

MÉMOIRE PRÉSENTÉ EN VUE DE L'OBTENTION
DU DIPLÔME DE MAÎTRISE ÈS SCIENCES APPLIQUÉES
(GÉNIE AÉROSPATIAL)
AVRIL 2017

UNIVERSITÉ DE MONTRÉAL

ÉCOLE POLYTECHNIQUE DE MONTRÉAL

Ce mémoire intitulé :

MODELING OF THIN WATER FILMS ON SWEPT WINGS IN ICING CONDITION

présenté par : LAVOIE Pierre

en vue de l'obtention du diplôme de : Maîtrise ès sciences appliquées

a été dûment accepté par le jury d'examen constitué de :

M. REGGIO Marcelo, Ph. D., président

M. LAURENDEAU Éric, Ph. D., membre et directeur de recherche

M. FORTIN Guy, Ph. D., membre

DEDICATION

To the one person
who relentlessly
supported me through
this challenge. . .
AMB

ACKNOWLEDGEMENTS

RÉSUMÉ

Les outils de simulation numérique du givrage sont d'une importance significative pour une conception optimale de l'avion et sa sécurité en vol. Des logiciels de givrage de nouvelle génération sont en cours d'implantation au sein de l'industrie aéronautique, amenant des outils de prédiction précis et applicable à tout type de géométrie. Néanmoins, une modélisation adéquate des films d'eau caractéristique de la glace de type verglas est requise pour améliorer les prédictions actuelles et pour répondre aux récentes normes de certification concernant les gouttelettes surfondues de grande taille (communément nommées SLD).

Ce projet de recherche vise à modéliser correctement la glace de type verglas sur des profils d'ailes en condition de givrage. Pour atteindre cet objectif, trois aspects principaux sont considérés : l'évaluation adéquate du transfert de chaleur par convection, une bonne représentation des nuages de gouttelettes et une modélisation juste de la physique des films d'eau. De plus, les méthodes utilisées doivent être compatible pour la simulation sur des ailes en flèche infinies.

En premier lieu, le calcul du coefficient de transfert de chaleur convectif est étudié afin de remplacer les méthodes semi-empiriques actuellement utilisées. Une méthode basée sur la solution des équations de Navier-Stokes est proposée afin de rendre le calcul applicable à tout type géométrie et à tout type d'écoulement. De plus, afin d'obtenir une meilleure représentation du nuage de gouttelettes et du même coup une meilleure prédiction des limites de glace, une distribution de tailles de gouttelettes est ajouté. Il est démontré que cette modification est nécessaire autant pour les tailles standards que pour les grandes tailles de gouttelettes. Enfin, l'évaluation de la force de traînée appliquée sur les gouttelettes est modifiée pour considérer la déformation de la gouttelette puisque celle-ci n'est plus strictement sphérique en régime SLD, elle tend plutôt vers la forme d'un disque.

En second lieu, un modèle thermodynamique basé sur des équations aux dérivées partielles pour l'évaluation de l'épaisseur de glace, l'épaisseur du film d'eau et de la température de surface est implémenté. Ce modèle suppose un film d'eau se déplaçant selon l'effet de la friction de l'air et donne des résultats très similaires à un modèle algébrique. Le modèle est résolu de manière instationnaire permettant l'ajout de phénomènes transitoires dans la modélisation du film d'eau. Un cas pathologique est démontré sur une géométrie manufacturée comportant des zones de recirculations où une accumulation d'eau peut être observée. Cette situation est rencontrée autant pour le modèle algébrique que pour le modèle aux dérivées partielles.

Finalement, les développements sont validés sur une série de cas de givrage bi-dimensionnels montrant une très bonne correspondance entre les résultats numériques et expérimentaux. De plus, le logiciel de givrage est appliqué à des cas d'ailes en flèche infinies. Une comparaison avec une correction bi-dimensionnelle de l'aile illustre une amélioration du transfert de chaleur par convection dans la zone de stagnation. L'approche utilisée dans ce mémoire permet de modéliser l'effet de la ligne de stagnation ce qui n'est pas le cas avec les méthodes usuelles pour la simulation d'ailes en flèche à partir d'une coupe bi-dimensionnelle.

En conclusion, une bonne amélioration de la prédiction de l'accumulation de glace est observée autant sur les cas bi-dimensionnels que sur des ailes en flèche infinies. De plus, puisque le modèle thermodynamique est implémenté sous forme de dérivée partielle et est résolu de manière instationnaire, celui-ci est bien adapté pour modéliser plus de physique dans le processus d'accrétion de glace, incluant des phénomènes transitoires. Les résultats suggèrent qu'un nouveau modèle prenant en compte une rugosité de surface variant en fonction de la position sur le profil d'aile est requis. Ensuite, pour atteindre une modélisation adéquate des SLD, un modèle prenant en compte l'éclaboussement et le rebond des gouttelettes doit être implémenté.

ABSTRACT

Numerical tools for the prediction of in-flight ice accretion are valuable for the optimal design and the safe operation of aircraft in icing conditions. A new generation of tools are making their way into the industry, providing more general and accurate icing softwares. Besides, a good representation of water films characterizing the glaze ice condition is needed to improve the current predictions and to model the newly defined requirements for Supercooled Large Droplets (SLD).

The current research project focuses on the proper modeling of glaze ice accretion on airfoils. To meet this objective, three main aspects are covered: a proper evaluation of the convective heat transfer, a good representation of the droplets cloud and the correct modeling of the water film on the surface of the airfoil. Furthermore, the methods implemented must be compatible for the simulation of ice accretion on infinite swept wings.

First, the evaluation of the Convective Heat Transfer Coefficient (HTC) is studied in order to replace the semi-empirical approach currently used. A method based on the solution of the Reynolds Averaged Navier-Stokes (RANS) equations is suggested and proves to be applicable to any type of geometries and airflow conditions. Moreover, to obtain a better representation of the droplets cloud and at the same time an improved prediction of the ice limits, a droplets size distribution is implemented. It is shown that this modification is required for both the standard and large size droplets. Then, the droplets drag model is modified to account for the deformation of the droplets which tend to be more disk shaped as their size increases instead of simply spherical.

Second, a Partial Differential Equation (PDE) based model for the evaluation of the water thickness, the ice height and the surface temperature is implemented. The thermodynamic model assumes a skin friction driven water film and provides results similar to its algebraic counterpart. The PDE model is solved unsteady allowing the addition of transient phenomena for modeling the water film. A pathological case is demonstrated on a manufactured geometry where water accumulation is observed near the recirculation zones. This behavior is observed for both the PDE and algebraic models.

Finally, a validation is performed on two-dimensional icing cases demonstrating a very good agreement between the numerical and experimental results. The icing software is also tested for ice accretion on infinite swept wings. A comparison with a two-dimensional correction method for the simulation of swept wing shows a better evaluation of the convective heat transfer near the stagnation point. The current approach models the stagnation line which

is not the case for usual methods simulating swept wings from two-dimensional cuts.

To conclude, a fair improvement of the ice accretion prediction is achieved both for the two-dimensional and the infinite swept wings cases. Moreover, since the thermodynamic model is PDE-based and solves the unsteady equations, it is well suited for the modeling of additional ice accretion physics, including the transient phenomena. The results suggest that a new model representing a variable surface roughness depending on the location along the airfoil is needed to improve the ice shapes further. Then, to properly model the SLD, the splashing and rebound mechanisms have to be considered.

TABLE OF CONTENTS

LIST OF TABLES

LIST OF FIGURES

LIST OF SYMBOLS AND ABBREVIATIONS

$\bar{u}$	mean water film velocity
$\dot{m}$	mass rate
$\dot{Q}$	energy rate
$\vec{n}$	unit normal vector
c	chord length
C_D	droplet drag coefficient
C_f	skin friction coefficient
C_p	specific heat at constant pressure
Cp	coefficient of pressure
g	gravitational acceleration
h	height or thickness (water film, ice layer)
k	conductivity
k_s	equivalent sand grain roughness
L	latent heat
M	Mach number
n	time index
P	pressure
p_v	vapor pressure
Pr	Prandtl number
R	gaz constant for the air (287)
r	recovery factor
R_M	Macklin parameter
Rh	air relative humidity
s	curvilinear distance
St	Stanton number
T	temperature
t	time
T_v	vapor temperature
T_{rec}	recovery temperature
T_{ref}	temperature of fusion of water (freezing temperature), $273.15K$
U	velocity
We	droplet Weber number
Re_d	droplet Reynolds number

Subscripts

∞	freestream related variable
a	air related variable
$cond$	conduction
$conv$	convection
d	droplet related variable
e	variable at the edge of the boundary layer
ev	evaporation
ice	ice related variable
imp	impingement
in	inflow
kin	kinetic
L	left state
out	outflow
R	right state
rad	radiation
st	stagnation water or water accumulation
su	sublimation
w	water related variable
$wall$	variable at the wall

Greek Symbols

β	collection efficiency of the droplets
δ	boundary layer thickness
γ	heat capacity ratio of air (typically $\gamma = 1.4$)
Λ	sweep angle
λ	eigenvalues
μ	dynamic viscosity
ν	kinematic viscosity
ρ	density
σ_r	Stefan-Boltzmann constant
σ_w	surface tension of water
τ	shear stress
θ	momentum thickness
ε	radiative surface emissivity of ice

Abbreviations

AoA	Angle of Attack
CAR	Canadian Aviation Regulations
CFL	Courant-Friedrichs-Lewy
EASA	European Aviation Safety Agency
FAA	Federal Aviation Administration
FAR	Federal Airworthiness Regulations
FVM	Finite Volume Method
HTC	Convective Heat Transfer Coefficient
IBL	Integral Boundary Layer
LWC	Liquid Water Content
MVD	Median Volume Diameter
NURBS	Non-Uniform Rational B-Spline
PDE	Partial Differential Equation
RANS	Reynolds Averaged Navier-Stokes
RMS	Root Mean Square
SA	Spalart-Allmaras
SLD	Supercooled Large Droplets
SSD	Supercooled Standard Droplets
SWIM	Shallow Water Icing Model

LIST OF APPENDIXES

CHAPTER 1   INTRODUCTION

1.1   Theoretical Framework

As an aircraft flies through a cloud of supercooled droplets, ice accretion may occur on the exposed and unprotected surfaces (such as the wing, tail and engine nacelle). The ice buildup can lead to a serious degradation in aerodynamic performance via a decreased maximum lift coefficient and stall angle of attack, and an increased profile drag (Gent et al., 2000). The behavior of the control surfaces may also be affected, inducing a loss in maneuverability. Moreover, ice accretion on engine related components can reduce the propulsion efficiency and add to the aircraft drag. Thus for many reasons, in-flight icing poses a serious threat to aircraft safety and has lead to many aircraft accidents as listed by Cebeci et al. (2005). Recently, in 2009, the crash of Air France flight 447: Rio-Paris (BEA, 2012) was ice accretion related. One probable cause is the obstruction of a Pitot tube by ice crystals which lead to a non-recoverable stall and the loss of the airplane.

Since in-flight ice accretion is a potentially dangerous phenomenon, aircraft incorporate anti-icing and/or de-icing systems to protect critical components. For commercial aircraft, these systems typically use bleed air from the engines or electric heaters to melt the ice that may accumulate. However, as the industry strive for the most energy efficient aircraft, some areas are left unprotected. It allows a moderate ice accumulation that must be safely tolerated by the aircraft. Furthermore, in the certification process, the designers must demonstrate that the aircraft performs safely in specific icing conditions. It also must be proven that the aircraft can be safely flown for a specific period of time in the event of a failure of the ice protection systems. In the United-States The certification process follows the regulations of the Federal Aviation Administration (FAA), also known as the Federal Airworthiness Regulations (FAR), in Canada it is Transport Canada with the Canadian Aviation Regulations (CAR) and in Europe there is the European Aviation Safety Agency (EASA). For instance, Appendix C of FAR Part 25 (FAA, 2016a) describes the icing envelope and certification requirements for regular supercooled droplets cloud.

1.1.1   Supercooled Large Droplets

In 1994, the crash of the American Eagle Flight 4184 (NTSB, 1996) was caused by severe icing conditions known as Supercooled Large Droplets (SLD). SLD are quite a newfound phenomenon and are very dangerous for in-flight icing. The larger droplets characteristic of

SLD tend to travel following a straighter path leading to a wider impact area on the airfoil. The droplets impingement can even extend outside the region protected by anti-icing and de-icing systems. It can then lead to the formation of ice ridges which have a significant effect on aircraft performances and handling. The flight 4184 encountered icing conditions which were outside the certification range provided by the Appendix C of FAR Part 25. Following this incident, new regulations have been added to account for the SLD regime, the Appendix O of the FAR Part 25 (FAA, 2016b).

1.1.2 Numerical Simulation of Ice Accretion

To demonstrate that the aircraft can be operated safely in any icing conditions, the ice shape leading to the worst degradation of performance and maneuverability is sought. Ice accretion depends on many parameters: the ambient temperature, the airspeed, the altitude, the size and the geometry of the body, the liquid water content of the droplets cloud, the size of the droplets, the droplets size distribution in the cloud and the time. Hence, the search for the worst ice shape includes a wide range of icing scenarios. It is inconceivable to evaluate all of them using in-flight or wind tunnel tests since it would be too expensive and time consuming. It is also implausible to encounter all conditions of the Appendix C of part 25 in flight, because some conditions occurs rarely. Hence, numerical methods capable of predicting ice shapes in specific icing conditions have been developed. These numerical tools allow the evaluation of multiple scenarios at a lower cost and allow the prediction of the worst situations. The resulting ice shapes is then tested in a wind tunnel for development and in-flight to complete the certification process.

Numerical tools are also used in the design of ice protection systems. To provide the best ice protection with the lowest energy consumption, the ice shape and the energy required to remove it must be evaluated. Again, it can be performed experimentally via wind tunnel testing, but numerical simulation makes for a much faster and cost-efficient process considering the size of the test matrix. Thus, accurate and efficient ice prediction tools are needed for the design and optimization of de-icing/anti-icing systems.

The numerical prediction of the ice shape can be decomposed in two main phases. First, the amount of droplets impacting the surface must be determined (impingement rates, catch efficiency). Second, the ice accretion rate or ice thickness must be evaluated in order to obtain the ice shape. Both phases require knowledge of the airflow field in terms of velocity, pressure, shear stresses and temperature, as these parameters will influence the droplets trajectories and the surface heat balance. Thus the ice accretion tool must accurately solve the airflow, the droplets field or trajectories and the thermodynamic balance on the surface that in turn

determine the iced geometry.

1.2 Problem Statement

Ice accretion may occur when an aircraft flies through a cloud of supercooled water droplets (Kind et al., 1998). At relatively low temperatures, the droplets will freeze upon impact with the aircraft, creating rime ice. Rime ice shapes are fairly streamlined and are well predicted by usual ice accretion softwares. At warmer temperatures, only a fraction of the water impacting the airplane will freeze, forming glaze ice. The unfrozen water is driven away by the airflow to generate a water film known as runback water. Hence, in glaze ice conditions the water film can extend the icing limits and also generate more complex ice shapes such as ice horns (Figure 1.1). Glaze ice is the most dangerous type of ice for aircraft since it induces a larger degradation in aerodynamic performance.
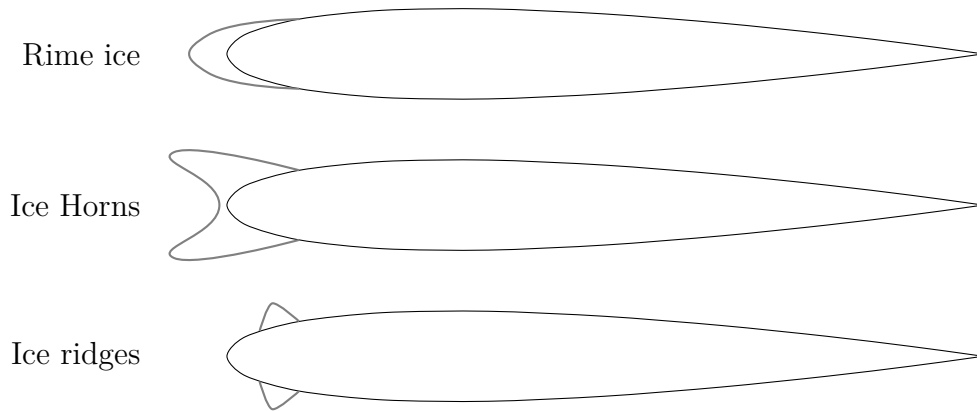
Figure 1.1 Rime ice, ice horns and ice ridges schematized on a NACA0012 airfoil

A water film can also appear in other situations. In protected regions where the de-icing/anti-icing system is activated, the system melts the ice creating a water film that can re-freeze when reaching an unprotected zone. It can then form an ice ridge which have again a strong and adverse effect on the aerodynamics of aircraft (Figure 1.1). SLD conditions may also be favorable for the formation of ice ridges. Typically, a wider region is impacted by the droplets which can extend the ice accretion outside the protected zone.

The aeronautic industry uses icing softwares to help with aircraft certification and the design of ice protection systems. However, these softwares generally poorly model the water films present in glaze ice, SLD, de-icing or running wet anti-icing conditions, although this phenomena often lead to the most dangerous icing scenarios.

1.2.1 Industrial State-of-the-art

The first icing softwares were developed as bi-dimensional low-fidelity tools. They use panel methods to solve the airflow, Lagrangian methods to track the droplets trajectories and impact points on the aircraft, and algebraic models to solve the mass and energy balances determining the ice thickness. These first generation icing softwares have been used for certification and provide a good estimate of the ice shape for many icing conditions. They are however often limited by the incompressible and non-viscous assumptions of their airflow solver. Additionally, it is not a simple task to apply these tools to complex geometries such as multi-element airfoils.

1.2.2 Research State-of-the-art

A new generation of tools have gradually emerged which tends to use the RANS equations for the airflow, an Eulerian formulation to compute the droplets trajectories and a PDE approach to solve the energy and mass balances. These second generation tools are easier to extend to three-dimensional simulations, can handle complex geometries more automatically and are more general than their predecessors as they model a compressible, viscous and turbulent flow (RANS). Designers strive for safer and more energy efficient aircraft, the increased accuracy from the 2nd generation softwares is thus of great interest.

1.3 Objectives

The current research project focuses on the modeling of glaze ice accretion on airfoils which is characterized by the simultaneous presence of an ice layer and a water film. The specific objectives comprise:

1. the implementation and analysis of proposed methods to evaluate the convective heat transfer;

2. the analysis of thermodynamic models capable of representing the water films;

3. an original extension of the previous two methods to allow simulation on swept wings.

The detection of the correct type of ice (glaze vs rime) is not straightforward. Various parameters influence the heat balance on the airfoil surface leading to the formation, or not, of a water film. The first specific objective will allow the formation of a water film only when there should be one. For instance, there should be no runback water in typical rime ice condition while a water film is present for glaze ice condition. Second, once the conditions

when a water film is present are correctly detected, the water film itself must be modeled via the use of a proper thermodynamic model. Third, an original method simulating the airflow on swept wings from a bi-dimensional solver is already implemented in NSCODE (Bourgault-Côté et al., 2017). Thus, the developments to the ice accretion modules must be extended to allow icing simulation on swept wings. The project will use NSCODE-ICE, a second generation icing software, as a development platform.

1.4 Structure of Thesis

To begin, a literature review relevant to general icing simulations, and more specifically to the convective heat transfer and to the thermodynamic modeling of ice accretion, is presented in Chapter 2. Then, Chapter 3 provides an overview of the icing software NSCODE-ICE, laying the basis of the current development environment. This chapter also details the method for the evaluation of the convective heat transfer and its validation. Since many improvements were incorporated in NSCODE-ICE, secondary features are also discussed in this chapter. Then, Chapter 4 describes the implementation of a new thermodynamic model including an analysis of the water film behavior. A validation of the icing software is presented in Chapter 5 with icing results on multiple rime ice and glaze ice cases. Results for ice accretion on swept wings are also discussed. Finally, the conclusion (Chapter 6) completes an overview of the research project, highlighting the important results and drawbacks. Recommendations will be given on how to further improve the implementations presented in this thesis and NSCODE-ICE.

CHAPTER 2   LITERATURE REVIEW

2.1   Icing Softwares

Several icing softwares have been developed through the years for both two-dimensional and three-dimensional simulations. These software differ slightly in the method used but they follow the same logic (Kind et al., 1998). They are typically divided in four modules. Although some developments have been made for fully coupled method (Naterer (2003), Aliaga et al. (2011)), they are usually assumed to be weakly coupled. Thus allowing to sequentially solve each module for a steady state, in the order listed below.

1. The airflow solution is computed around the geometry.
2. The amount of water droplets impinging the body is evaluated (catch efficiency).
3. The ice accretion rates are evaluated via mass and heat balances.
4. The resulting ice shape is evaluated on the geometry.

The airflow can be computed using panel methods as used by many of the early icing softwares: NASA LEWICE, ONERA and DRA TRAJICE softwares (Wright et al., 1997), CANICE (Brahimi et al., 1994), CIRA MULTICE (Mingione and Brandi, 1998), etc. This method is suitable for relatively low Mach numbers ($Mach < 0.2$) and for moderate angle of attacks (smaller than the stall angle due to the assumption of incompressible and inviscid flow). Some icing softwares model the airflow by panel method including compressibility correction or coupled with compressible boundary layer methods. More recent codes tend to use higher fidelity methods. For instance, Euler equations coupled with a boundary layer code for the heat transfer computation (Hedde and Guffond, 1995) or using the RANS equations as used by FENSAP-ICE (Beaugendre, 2003) and NSMB-ICE (Pena et al., 2016a) to name a few. LEWICE (e.g. LEWICE 3.5) can also be coupled with RANS solvers. This allow the use of a general flow solver applicable to a wider range of scenarios since it accounts for compressibility, viscosity and turbulence.

Droplets catch rates on the geometry can be evaluated following two main approaches: Lagrangian or Eulerian (Gent et al. (2000), Bourgault et al. (1999)). For the former, droplets trajectories are integrated in time from seeding points to the impact on the geometry. Although the process can be automated, an algorithm or an experienced user is often required to determine the range of seeding points needed to obtain the catch limits on the geometry. With this method each droplets are followed individually to determine the catch efficiency.

For the Eulerian approach, a droplets velocity and density field is solved similar to a Navier-Stokes solver. The droplets catch limits are computed automatically since the field is solved all at once. Typically the computational grid for the flow solver is re-used to solve the droplet field. This method has gained popularity in second generation icing codes like FENSAP-ICE, NSMB-ICE and many others, although each approach has it pros an cons.

To determine the ice accretion rates, runback water behavior and surface temperatures, a thermodynamic model is required. A variety of algebraic and PDE models have been developed and successfully implemented. Second generation icing softwares again tend to use the PDE approaches since it is more general. A more detailed review is given in §2.3.

The evaluation of the new iced geometry is generally done by simple node displacement technique (e.g. Beaugendre (2003)), where the nodes are displaced normal to the surface by a distance corresponding to the ice thickness. This method does not ensure mass conservation in the presence of convex or concave geometry and may lead to geometry clashes in some cases. The iced geometry can also be evaluated via a PDE formulation using for instance the level-set equation (Pena et al., 2016b), which automatically avoid geometry clashes but does not inherently ensure mass conservation. Although the methods are not well documented, corrections can be applied to obtain a mass conservative ice growth scheme.

2.1.1 Multi-Layer Icing and Predictor-Corrector Methods

Ice accretion is inherently an unsteady problem. The airflow influences the droplets trajectories and the mass and heat balances. Ice accumulates, affecting the effective geometry and in turn, it impacts the airflow. The motivation behind multi-layer icing simulations is to approach the solution of the unsteady phenomenon by assuming that if the ice growth is small enough, the airflow and droplets field solution are only slightly affected (Verdin et al., 2009). Then, the idea is to divide the total ice accretion time in small steps (layers) to solve the uncoupled problem in quasi-steady state.
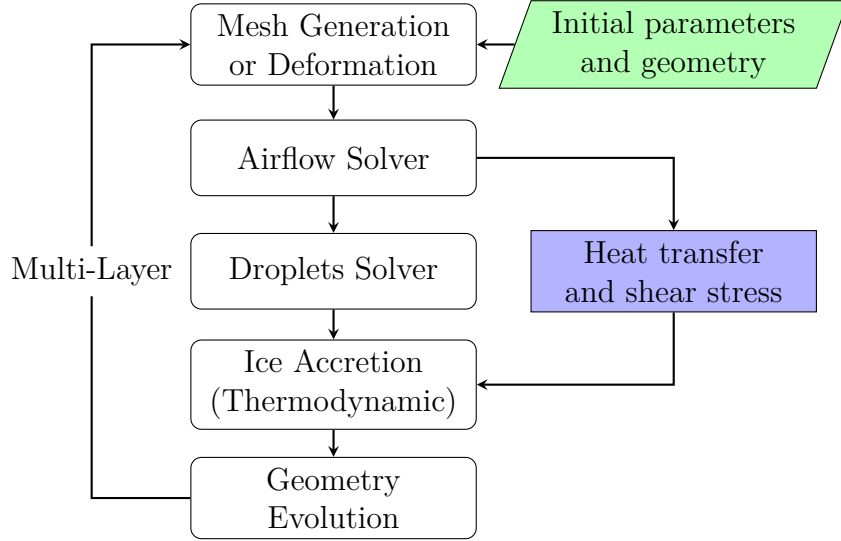
Figure 2.1 Typical multi-layer icing simulation

The structure of a typical multi-layer icing simulation is shown in Figure 2.1. The general process goes as follows. The user inputs the icing parameters then the mesh is generated using the initial geometry (clean airfoil) or an initial mesh is inputted. The airflow field is then solved to obtain knowledge about the velocity and pressure distribution around the body. From this solution the convective heat transfer coefficient can be computed. The droplets field is solved using the solution from the flow field. Then the thermodynamic balance is performed to compute the runback water, surface temperature and ice accretion rates. The new iced geometry is created and supplied to a mesh generator or a mesh deformation tool to produce the new mesh for the next layer. The process is repeated until the required number of ice layers is achieved.

Typically, once the new mesh is generated, everything is reset so the next layer is solved like if it was a clean geometry (no ice nor water). When using a thermodynamic model like the Messinger model (Messinger, 1953), this is a correct assumption. However, for models like the SWIM (Bourgault et al., 2000) or for models considering the conduction through ice (Myers, 2001), this is not entirely true. For such models, the solution of the current layer depends on the solution of the last one in terms of ice thickness, water film height and surface temperature. Hence, parameters are sometimes interpolated from the old geometry onto the new mesh to ensure mass conservation and correctness of the models.

The predictor-corrector method follows a slightly different philosophy (Wright et al. (1997), Mingione and Brandi (1998), (Verdin et al., 2009)). The ice accretion for the full icing time is first performed. This is known as the predictor step. Then the airflow and droplets catch

efficiencies are computed on the new iced geometry. By assuming a linear variation of the parameters between the solution of the clean airfoil and the iced geometry, the airflow and droplets solutions can be interpolated in time. The ice accretion is then integrated in time from the clean geometry to obtain a corrected iced geometry. This last step is known as the corrector step. The flow and droplets solution can then be re-evaluated on the corrected ice shape, a new linear interpolation can be computed and a new corrector step can be performed. This process can be repeated until a convergence is reached (i.e. when the difference between two corrector steps is deemed negligible). Typically, the method is used with one predictor step and one corrector step. The following list summarizes the predictor-corrector approach:

1. evaluate a single ice layer spanning the full icing time (predictor step);

2. compute the parameters on the new iced geometry (airflow, droplets, etc.);

3. evaluate a new ice shape based on the interpolated time-dependent parameters and assume a linear variation of the parameters between the clean geometry and the iced shape (corrector step);

4. repeat steps 2 and 3 until the desired convergence is achieved.

When performing a multi-layer icing simulation, more than two layers are usually employed. On the other hand, the predictor-corrector method generally requires only two ice accretion simulations and a correction step and is therefore faster. As for the accuracy of the methods, a code comparison was performed by the DRA, ONERA and NASA (Wright et al., 1997). Numerical ice shapes were compared to experimental results. From this data, one can observe that the icing code from the ONERA, which is a method similar to a predictor-corrector approach, generate ice shapes very similar to the code from the DRA or NASA. Sometimes one method gives better results and sometimes the other is more accurate. Thus, the predictor-corrector approach seems as good as the multi-layer approach, at least when compared to a four layers simulation. Also, a comparison of the multi-layer icing method and the predictor-corrector approach was performed by Huang et al. (2016). They concluded that the predictor-corrector method provide fair results on the rime ice cases while being faster than the multi-layer simulations. For the glaze ice cases, the multi-layer approach is preferred since it best captures the features in the stagnation area and the ice horns. Hence, in the presence of runback water the multi-layer icing procedure is more suitable. Verdin et al. (2009) reached a similar conclusion associating the predictor-corrector method with rime ice cases and preferring the multi-layer approach for glaze ice cases.

2.2 Surface Roughness

The convective heat transfer is very sensitive to surface roughness and in turn, greatly influences the ice shape. Surface roughness is present on the body itself in the form of surface finish or contaminants. It also takes the form of irregularities on the body and the ice shape. The roughness varies as the ice accretion process begins. For glaze ice, a relatively smooth zone is present in the stagnation area (Hansman, 1989). As the water film travels downstream, water beads and rivulets can form, increasing the effective surface roughness. Since it is directly related to convective heat transfer, surface roughness influences the size and location of ice horns, and determines the icing limits. Thus, proper estimation of this parameter is paramount to obtain a sensible ice shape.

Little experimental data is available on surface roughness. Icing softwares take the roughness as an input parameter and thus, an experienced user can provide its own estimation. For a more automatic approach, various methods have been developed to estimate its value. Shin et al. (1991) suggest an empirical relation as a function of temperature, airspeed, Liquid Water Content (LWC), Median Volume Diameter (MVD) and chord length. With this model, a constant roughness is assumed on the entire surface. The relation was reversed engineering from ice predictions to provide the best ice shape in comparison with experimental results. LEWICE 1.0 (Wright et al., 1997) uses an analytical relation based on the problem's physics, where a bead height is evaluated and used as an equivalent sand grain roughness. The relation depends on surface tension, the viscosity and density of water, the surface shear stress and the wetted surface fraction. The latter is related to the contact angle of the impinging droplets. This analytical model allows the roughness to vary with the location on the geometry. LEWICE 2.2 (Wright, 2002) uses a simple relation equating the surface roughness to the freezing fraction at the stagnation point. The relation was developed from experimental measurements of roughness.

Fortin et al. (2004) provide an analytical model based on the maximum bead height. It evaluates a local roughness value instead of a global one. Ice predictions with this model are in close accordance with wind-tunnel experiments. FENSAP-ICE (Croce et al., 2010) also developed a roughness model based on bead height and rivulets. Their model allows the evaluation of the surface roughness in space and time. The estimation of surface roughness based on bead height and rivulets provides a roughness distribution and reduces the empiricism of the more classical methods.

2.3 Convective Heat Transfer

The convective heat transfer ($\dot{Q}_{conv}$) is one of the most important term in the heat balance and also one of the most difficult to evaluate accurately (Gent et al., 2000). There are two main approaches to evaluate the HTC which depends on the flow solver employed. When using a potential flow solver (e.g. panel method), the viscous effects are not considered and hence one must approximate the boundary layer characteristics. However when using a boundary layer code or a Navier-Stokes solver, it is possible to compute the HTC, using the correct assumptions. These two approaches are reviewed below by describing four techniques.

2.3.1 Integral Boundary Layer (IBL)

The IBL method, not to be confused with the Interactive Boundary Layer method (Cebeci and Cousteix, 2005), is common use in combination with potential flow solvers (e.g. panel method). A description of the method is given by Fortin et al. (2006), Özgen and Canibek (2009) and many others. The main elements are presented below. With this method, an integral is evaluated from the stagnation point towards the trailing edge in order to compute the characteristics of the boundary layer. For the laminar region, the HTC is given by:

$$HTC = \frac{0.296 k_s U_e^{1.435}}{\sqrt{\nu \int_0^s U_e^{1.87} ds}} \tag{2.1}$$

where U_e is the velocity at the edge of the boundary layer.

The transition from laminar to turbulent is defined by the roughness Reynolds number.

$$Re_k = \frac{U_k k_s}{\nu} \tag{2.2}$$

$$Re_k \begin{cases} \leq 600 & laminar\,flow \\ > 600 & turbulent\,flow \end{cases} \tag{2.3}$$

where U_k is the flow velocity at the roughness height (k_s).

$$\frac{U_k}{U_e} = 2\frac{k_s}{\delta} - 2\left(\frac{k_s}{\delta}\right)^3 + \left(\frac{k_s}{\delta}\right)^4 + \frac{1}{6}\frac{\delta^2}{\nu_a}\frac{dU_e}{ds}\frac{k_s}{\delta}\left(1 - \frac{k_s}{\delta}\right)^3 \tag{2.4}$$

The boundary layer thickness is given by:

$$\delta = \frac{315}{37}\theta_l \tag{2.5}$$

and the laminar momentum thickness (θ_l) is computed using Thwaite's equation:

$$\theta_l^2 = \frac{0.45\nu}{U_e^6} \int_0^s U_e^5 ds. \tag{2.6}$$

For the turbulent region, HTC is computed from:

$$HTC = St\rho_e U_e C_p \tag{2.7}$$

$$St = \frac{C_f/2}{Pr_t + \frac{\sqrt{C_f/2}}{St_k}} \tag{2.8}$$

$$St_k = 1.92 Re_{tk}^{-0.45} Pr^{-0.8} \tag{2.9}$$

$$Re_{tk} = \frac{U_t k_s}{\nu} \tag{2.10}$$

$$U_t = U_e\sqrt{C_f/2} \tag{2.11}$$

$$\frac{C_f}{2} = \frac{0.1681}{[ln(864\theta_t/k_s + 2.568)]^2} \tag{2.12}$$

$$\theta_t = \frac{0.036\nu^2}{U_e^{3.29}} \left(\int_0^s U_e^{3.86} \right)^{0.8} + \theta_{tr} \tag{2.13}$$

with $Pr_t = 0.9$ (the turbulent Prandtl number) and θ_{tr} the momentum thickness at the transition location.

The IBL method provides fairly good results and has been widely employed in icing softwares. However, it is a semi-empirical method depending on the correct detection of the stagnation point, which is not always simple to achieve. Moreover, in case of multiple stagnation points, one must decide where to start the integration and it can get difficult to automatize. Also, to extend the method to 3D simulations, a slightly different approach is needed as the integration process must follow the streamlines.

2.3.2 Fully Turbulent Assumption

When the coefficient of friction (C_f) is available (RANS or boundary layer code), the integration process is avoided and the location of the stagnation point is no longer needed. Hence,

the method reduces to:

$$HTC = St\rho U_e C_p \tag{2.14}$$

$$St = \frac{C_f/2}{Pr_t + \frac{\sqrt{C_f/2}}{St_k}} \tag{2.15}$$

$$St_k = 1.92 Re_{tk}^{-0.45} Pr^{-0.8} \tag{2.16}$$

$$Re_{tk} = \frac{U_t k_s}{\nu} \tag{2.17}$$

$$U_t = U_e \sqrt{C_f/2} \tag{2.18}$$

with $Pr_t = 0.9$ (the turbulent Prandtl number), where St is the Stanton number and C_f is available from the flow solver. However, with this approach the choice of turbulence model and the quality of the mesh influences the value of C_f and in turn, the HTC. Also, this method tends to overestimate the convective heat transfer. Finally, the roughness height becomes an input of the flow solver since it is used in the turbulence model. This method was previously used by Bourgault-Côté (2015) as an attempt to avoid the limitation of locating the stagnation point.

2.3.3 FENSAP-ICE Method

FENSAP-ICE (Beaugendre, 2003) solves the RANS equations and evaluate the HTC from the airflow solution. The usual adiabatic wall boundary condition is replaced by a fixed wall temperature, thus a wall heat flux $(\dot{Q}_{wall})$ can be evaluated. Then the HTC can be computed using Newton's law of cooling.

$$\dot{Q}_{wall} = HTC(T_{wall} - T_\infty) \rightarrow HTC = \frac{\dot{Q}_{wall}}{T_{wall} - T_\infty} \tag{2.19}$$

where $\dot{Q}_{wall}$ is computed by using the temperature gradient at the wall:

$$\dot{Q}_{wall} = k_a \left. \frac{dT}{d\vec{n}} \right|_{wall} \tag{2.20}$$

Where k_a is the air thermal conductivity and $\vec{n}$ is the normal to the wall. The results from this method highly depend on the accuracy of the turbulence model, the roughness height evaluation and the mesh quality, especially close to the wall. A proper evaluation of the wall distance is also important to get the correct wall temperature gradient. The computed Convective Heat Transfer Coefficient also depends on the temperature imposed at the wall

but only slightly. This method is valid for any geometries and does not depend on the location of the stagnation point. Moreover, depending on the turbulence model used, it can model both laminar and turbulent heat transfer.

2.3.4   ONERA Method

This method developed by the ONERA (Montreuil et al., 2009) is similar to the approach of FENSAP-ICE (§2.3.3). One difference is the definition of the HTC which depends on T_{rec}, the recovery temperature or the adiabatic wall temperature.

$$HTC = \frac{\dot{Q}_{wall}}{T_{wall} - T_{rec}} \tag{2.21}$$

where $\dot{Q}_{wall}$ is computed from Eq. (2.20). Thus, the method accounts for pressure gradients and compressibility effects, which is more general. Since there are two unknowns (T_{rec} and HTC), two airflow solutions are solved by imposing two wall temperatures.

$$\dot{Q}_{wall1} = HTC(T_{wall1} - T_{rec}) \tag{2.22}$$

$$\dot{Q}_{wall2} = HTC(T_{wall2} - T_{rec}) \tag{2.23}$$

so that T_{rec} and HTC are computed from:

$$HTC = \frac{\dot{Q}_{wall2} - \dot{Q}_{wall1}}{T_{wall2} - T_{wall1}} \tag{2.24}$$

$$T_{rec} = T_{wall1} - \frac{\dot{Q}_{wall1}}{HTC} = T_{wall2} - \frac{\dot{Q}_{wall2}}{HTC} \tag{2.25}$$

The main advantage of this method is that the recovery temperature is not computed from a theoretical relation. It is evaluated directly from the numerical solution, hence slightly more accurate. However, the method is more costly since it requires two airflow solutions (two complete runs of the Navier-Stokes solver). The method also suffers from the same limitations as FENSAP-ICE's approach since it depends on the turbulence model, grid quality, etc.

2.4   Thermodynamic Modeling

Messinger (1953) is one of the precursor of ice accretion modeling. Messinger's model rely on a mass balance and a heat balance. Additionally, it models the presence of a water film on the airfoil surface by assuming it starts from the stagnation point and flows downstream until reaching the trailing edge or until it freezes. This model was initially developed for two

dimensional simulations, hence the surface is discretized using one-dimensional cells (panels). The simulation begins at the stagnation cell where the inlfow is set to zero. Then, the heat and mass balances are evaluated to determine the ice accretion rate ($\dot{m}_{ice}$), the amount of unfrozen water exiting the cell ($\dot{m}_{out}$) and the surface temperature (T_{surf}). The outflow from the current cell becomes the inflow for the next cell and the process is repeated.

Many icing softwares are using the Messinger model or some of its derivatives to evaluate the ice accretion on airfoils. For instance, early versions of NASA, DRA and ONERA softwares (Wright et al., 1997), CANICE (Brahimi et al., 1994) are using a similar model.

2.4.1   Heat and Mass Balances

A general mass and energy balances are respectively written in algebraic form as:

$$\dot{m}_{in} + \dot{m}_{imp} + \dot{m}_{st} = \dot{m}_{ice} + \dot{m}_{es} + \dot{m}_{out} \tag{2.26}$$

$$\dot{Q}_{kin} + \dot{Q}_{ice} + \dot{Q}_f + \dot{Q}_{in} + \dot{Q}_{st} = \dot{Q}_{conv} + \dot{Q}_{rad} + \dot{Q}_{es} + \dot{Q}_{imp} + \dot{Q}_{out} \tag{2.27}$$

These equations are typically solved by a trial and error method where each cell is tested to determine whether it is in a glaze, rime or liquid state.

The mass and heat balances are illustrated on Figure 2.2. Mass is added to the cell by the incoming droplets known as the droplet impingement rate ($\dot{m}_{imp}$) and by the inflow of water from the neighboring cell(s) ($\dot{m}_{in}$). This water can freeze leading to an ice accretion rate ($\dot{m}_{ice}$). Mass is lost either by evaporation ($\dot{m}_{ev}$) or sublimation ($\dot{m}_{su}$) which is combined in a term called $\dot{m}_{es}$. Finally, the remaining unfrozen water is denoted as $\dot{m}_{out}$, which turns into $\dot{m}_{in}$ for the next downstream cell. The outflow is generally referred to as runback water. The water accumulation rate or stagnation water ($\dot{m}_{st}$) represents the water remaining in the cell. It is not applicable to the Messinger model, but it is considered in the SWIM for instance.

The terms of the energy balance (Table 2.1) can be separated in two groups: cooling and heating effects. There is cooling by convective heat transfer ($\dot{Q}_{conv}$) and radiation ($\dot{Q}_{rad}$). The cooling by either evaporation or sublimation is denoted by $\dot{Q}_{es}$. For glaze ice or a liquid state, $\dot{Q}_{es}$ represents the evaporation term $\dot{Q}_{ev}$, while for rime ice it will be sublimation ($\dot{Q}_{es} = \dot{Q}_{su}$). There is also cooling by the impinging droplets ($\dot{Q}_{imp}$) which is caused by the temperature change of the incoming droplets to the reference temperature. $\dot{Q}_{out}$ represents the internal energy for the water outflow to the next cell.

For the heating effects, there is the kinetic heating ($\dot{Q}_{kin}$) which is due to the change in momentum of the impacting droplets. The release of latent heat while the water turns to ice is denoted by $\dot{Q}_{ice}$. $\dot{Q}_f$ represents the aerodynamic heating of the surface which is related

to the effect of compressibility and friction. Finally, $\dot{Q}_{in}$ and $\dot{Q}_{st}$ represent respectively the change in internal energy for the water inflow from the previous cell and for the water accumulating into the cell.

(a) Mass balance   (b) Energy balance
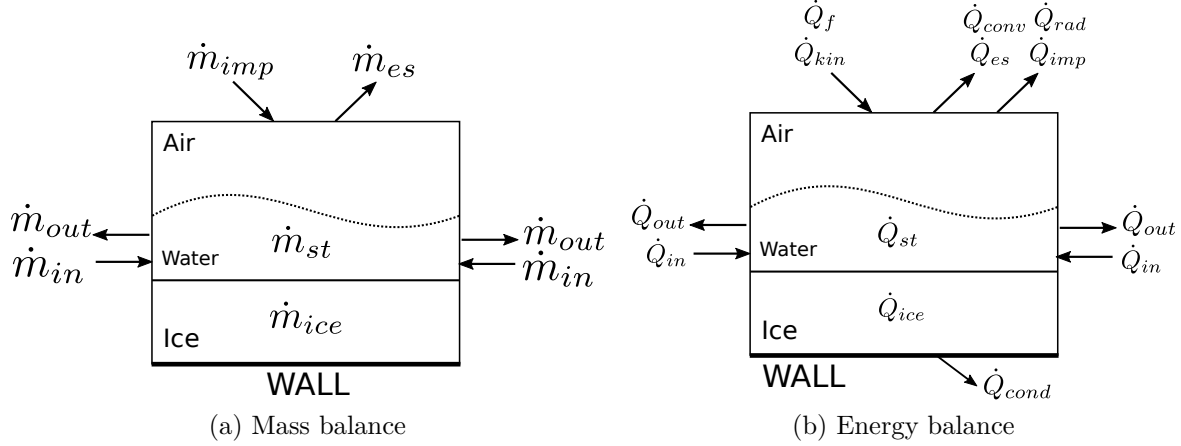
Figure 2.2 Diagrams for the mass and energy balances

The energy terms are defined in Table 2.1, where $\dot{m}_{imp} = U_\infty (LWC)\beta$ and $T_{ref} = 273.15$ K is the temperature of fusion for water (used as a reference temperature). The mass rate of evaporation $(\dot{m}_{ev})$ and sublimation $(\dot{m}_{su})$ depend on the ambient vapor pressure. The relations are given by Macarthur et al. (1982) and Özgen and Canibek (2009).

$$\dot{m}_{es} = \frac{0.7}{C_{p,a}} HTC \left(\frac{p_{v,surf} - Rh \cdot p_{v,e}}{P_e} \right) \tag{2.28}$$

The vapor pressure (p_v) is estimated with:

$$p_v = 3386(0.0039 + 6.8096 \times 10^{-6}T_v^2 + 3.5579 \times 10^{-7}T_v^3) \tag{2.29}$$

$$T_v = 72 + 1.8(T - T_{ref}) \tag{2.30}$$

Where T is taken respectively as T_{surf} and T_e to compute $p_{v,surf}$ and $p_{v,e}$.

Table 2.1 Definition of the energy terms for the heat balance

Variable	Description	Equation
$\dot{Q}_{conv}$	Convective heat transfer	$HTC(T_{surf} - T_e)$
$\dot{Q}_{ev}$	Evaporation heat loss	$\dot{m}_{ev}L_{ev}$
$\dot{Q}_{su}$	Sublimation heat loss	$\dot{m}_{su}L_{su}$
$\dot{Q}_{imp}$	Cooling by incoming droplets	$\dot{m}_{imp}C_{p,w}(T_{ref} - T_d)$
$\dot{Q}_{kin}$	Kinetic energy of incoming droplets	$\dot{m}_{imp}U_d^2/2$
$\dot{Q}_{ice}$	**Glaze**: release of latent heat	$L_{fus}\dot{m}_{ice}$
	Rime: release of latent heat + cooling of ice	$(\dot{m}_{ice} + \dot{m}_{su})(L_{fus} - C_{p,ice}\bar{T})$
$\dot{Q}_f$	Aerodynamic heating	$HTC\,rU_e^2/(2C_{p,a})$
$\dot{Q}_{in}$	Energy of water entering the control volume	$\dot{m}_{in}C_{p,w}(T_{in} - T_{ref})$
$\dot{Q}_{rad}$	Radiative heat transfer	$\sigma_r\varepsilon(T_{surf}^4 - T_\infty^4)$
	or a linear approximation	$4\sigma_r\varepsilon T_\infty^3(T_{surf} - T_\infty)$
$\dot{Q}_{out}$	Energy of water exiting the control volume	$(\dot{m}_{out} + \dot{m}_{ev})C_{p,w}(T_{surf} - T_{ref})$
$\dot{Q}_{st}$	Enthalpy change for stagnation water	$\dot{m}_{st}C_{p,w}(T_{surf} - T_{ref})$

2.4.2 Thermodynamic Models

Apart from the classic method presented by Messinger (1953), other thermodynamic models have been developed. Zhu et al. (2012) generalized Messinger's model to three-dimensional cases by embedding the model into an iterative loop allowing an automatic evaluation of the runback water direction. The shear stress and pressure gradients are used as the main driving forces for the water film and the formulation does not rely on the location of the stagnation point. Myers (2001) developed an extended Messinger model based on a Stefan problem which lead to a Messinger-like model. It has however one major difference, it considers the conduction through the ice layer by evaluating the temperature difference between the airfoil and the ice surface. This formulation is very interesting for anti-icing/de-icing applications where a temperature is specified on the airfoil surface. For standard icing simulations where the substrate temperature is unknown, one must assume this temperature, leading to arguable results. In fact, it may generate an unrealistic and thicker ice layer. It has however been used with a multi-layer approach by Özgen and Canibek (2009) and resulted in sensible ice shapes. Cao and Huang (2015) used a iterative version of Myers' model allowing a stagnation point independent method. The water film is driven by shear stress and the conduction through the ice layer is considered.

Similar to the Iterative Messinger model of Zhu et al. (2012), the Shallow Water Icing Model presented by Bourgault et al. (2000) automatically evaluates the water runback direction using the air shear stress as the main driving force. This model is based on lubrication theory

and uses a PDE formulation which is easily applicable to 3D icing simulations. It performs very much alike its algebraic counterpart, the Iterative Messinger model. Myers et al. (2002) published a PDE version of their Extended Messinger model to avoid the dependency on the stagnation point. In this new model, the water film is driven by the air shear stress, the pressure gradient in the water layer and the gravity forces which make for a more complete model. Myers and Charpin (2004) generalized their model to account for the curvature in the iced geometry, hence making it more suitable for airfoil. Cao and Hou (2016) used the model presented by Myers and Charpin (2004) which is formulated in orthogonal coordinates and adapted it to non-orthogonal general coordinates. They claim that this formulation is necessary for body fitted structured grids when the orthogonality at the wall is not ensured.

Thermodynamic models based on the PDE model of Myers and Charpin (2004) or following the same ideas have been widely used in the literature: Verdin et al. (2009), Yanxia et al. (2010), Wright et al. (2015), Chauvin (2015) to name a few. These models are more general, PDE based, hence following the current philosophy of the second generation ice accretion frameworks, and designed for three-dimensional applications.

2.5 Swept Wing Ice Accretion

In-flight ice accretion is inherently a three-dimensional phenomenon. For instance, the presence of the fuselage and the wing tip affects the ice accretion on the wing. Also, typical commercial aircraft are designed with swept wings that can include twist, dihedral and even a change of wing section along the span. Hence an accurate simulation of ice accretion requires the use of three-dimensional tools to account for the complex geometry and the three-dimensional nature of the flow. These type of simulations are however time consuming and costly which is not suitable when a large variety of cases are to be evaluated (e.g. early design phases, optimization, etc.). Therefore the industry requires an alternative approach which is fast and provides a fair solution compared to the full 3D methodology.

Ice accretion simulations are often focused on wings and a common approach is to perform a two-dimensional ice accretion simulation corrected for the sweep angle. Various methods have been developed to account for swept wings and the 2D correction of Dorsch and Brun (1953) is usually applied. With this method, a bi-dimensional simulation is performed on a cut normal to the leading edge of the wing by applying a change of coordinates. This correction affects the geometry but also the droplet catch efficiency, the velocity and the angle of attack

following Eq. (2.31). Moreover, Figure 2.3 represents the system of coordinates.

$$x' = x \cos(\Lambda)$$
$$y' = y$$
$$U'_\infty = U_\infty \cos(\Lambda)$$
$$\beta' = \beta \cos(\Lambda) \tag{2.31}$$
$$c' = c \cos(\Lambda)$$
$$AoA' = \frac{AoA}{\cos(\Lambda)}$$
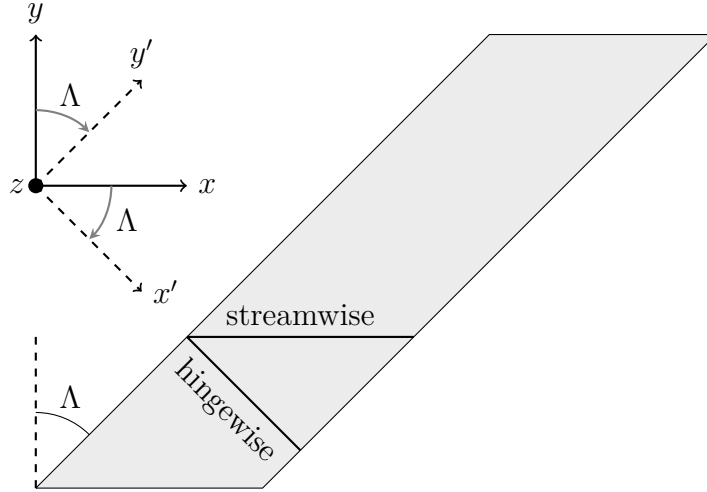
Figure 2.3 System of coordinates for the swept wing

Pueyo (2013) suggests a method similar to Dorsch and Brun (1953) but the simulation is performed on a streamwise cut of the wing, avoiding the change of coordinates. A correction Eq. (2.32) is still applied to the collection efficiency since the effective area for the droplet impingement must include the effect of the sweep angle.

$$\beta_{3D} = \frac{dA}{dS_\Lambda} = \frac{dA}{dS_0}\frac{dS_0}{dS_\Lambda} = \beta\frac{\sqrt{dx^2 + dz^2}}{\sqrt{dx^2 + \frac{dz^2}{\cos^2(\Lambda)}}} \tag{2.32}$$

where S_Λ is the impacted area for the swept wing, S_0 is the impacted area for the unswept wing, A is the droplet flux area upstream of the wing and β_{3D} is the streamwise collection efficiency corrected for geometrical 3D effects. The pressure coefficients on the streamwise cut are also matched with the solution from a 3D simulation to account for three-dimensional effects. The method of Dorsch and Brun (1953) assumes small AoA to derive Eq. (2.31).

Pueyo (2013) provides the exact relation for the hingewise method to ensure a more accurate solution at larger *AoA*.

$$U'_\infty = U_\infty \sqrt{1 - \cos^2(AoA)\sin^2(\Lambda)} \tag{2.33}$$

$$AoA' = \tan^{-1}\left(\frac{\tan(AoA)}{\cos(\Lambda)}\right) \tag{2.34}$$

Another approach to simulate swept wings has been recently presented by Bourgault-Côté et al. (2017) where the system of coordinates is rotated about the leading to obtain a hingewise cut on the wing.

$$\begin{bmatrix} x' \\ y' \end{bmatrix} = \begin{bmatrix} \cos(\Lambda) & -\sin(\Lambda) \\ \sin(\Lambda) & \cos(\Lambda) \end{bmatrix} \begin{bmatrix} x \\ y \end{bmatrix} \tag{2.35}$$

The spanwise derivatives are assumed null ($\partial/\partial y' = 0$), leading to a constant crossflow in the spanwise direction for the airflow, droplets field and runback water. For consistency, the farfield boundary conditions are also rotated:

$$u'_\infty = U_\infty \cos(AoA)\cos(\Lambda) \tag{2.36}$$

$$v'_\infty = U_\infty \cos(AoA) \tag{2.37}$$

$$w'_\infty = U_\infty \cos(AoA)\sin(\Lambda) \tag{2.38}$$

Apart from the two-dimensional correction methods, a quasi-3D approach can be used. These methods rely on the coupling of a three-dimensional inviscid low fidelity simulations to 2D viscous solutions. For instance, Silva et al. (2015) use a non-linear vortex lattice method for the 3D simulation and a RANS solver for the 2D viscous database. It allows to account for the effect of a finite wing, the sweep, the twist, etc.

CHAPTER 3   HEAT TRANSFER AND DROPLETS PROPERTIES

Before addressing the issue of the water film motion on the airfoil surface, it is important that the ice accretion software properly detects the presence of such a water film. The surface heat balance determines whether the droplets will completely freeze upon impact, partially freeze or stay entirely in liquid state. One of the dominant terms is the convective heat transfer which in turn is strongly affected by surface roughness.

Furthermore, in order to obtain the correct ice limits, the droplets collection efficiency must be evaluated properly. The assumption that the droplets are of a single size defined by the MVD is fair when the droplet sizes are of the order of $25\mu m$ (Supercooled Standard Droplets (SSD) regime). However, when the droplets diameter increase towards the SLD regime, the simulation of a droplet size distribution become more significant.

At Polytechnique Montreal, a second generation two-dimensional icing software has been under development since 2012, NSCODE-ICE. It uses a multi-layer approach to the ice accretion problem by re-meshing the geometry at each layer. The icing simulations are structured in five modules, which are sequentially solved for a steady state:

1. a mesh generator, NSGRID2D, developed by Hasanzadeh et al. (2016) at Polytechnique Montreal;

2. a RANS airflow solver, NSCODE (Pigeon et al., 2014), (Lévesque et al., 2015);

3. an Eulerian droplets field solver (Bourgault-Côté, 2015);

4. an algebraic thermodynamic module;

5. a geometry evolution solver.

As of 2015, NSCODE-ICE was only able to simulate a mono-dispersed droplet size distribution. It was using an algebraic thermodynamic model based on the work of Zhu et al. (2012) to evaluate the ice accretion and a simple node displacement method to grow the new geometry. Also, the HTC was evaluated using an IBL-derived method (§2.3.2). These aspects of convective heat transfer and droplet modeling will be addressed in this chapter as to build a decent basis for the development of the thermodynamic solver presented in the next chapter.

3.1 Convective Heat Transfer

By considering the different methods presented in §2.3, it is desirable to evaluate the Convective Heat Transfer Coefficient using a method which is:

- not stagnation point dependent;

- applicable to any type of geometries;

- computationally efficient.

The IBL methods are fast, but depend on the location of the stagnation point as it is needed to begin the integration process. NSCODE-ICE was using the Fully Turbulent Assumption approach of §2.3.2 which has proven to underestimate the HTC near the stagnation area and overestimate it elsewhere. A more accurate but still general method is required. FENSAP-ICE and ONERA methods are good candidates since they can be directly implemented as an extension of the RANS solver used in NSCODE-ICE. Both methods are very similar, the former being faster and the latter being slightly more accurate.

Since FENSAP-ICE method requires only one flow solution, it is more efficient computationally. It satisfies all the other requirements and hence, a generalized version of FENSAP-ICE method is selected for implemention in NSCODE-ICE. A description of the method is presented in the next section.

Note that FENSAP-ICE and ONERA methods require a fixed wall temperature boundary condition which was not available in NSCODE-ICE. Hence the new boundary condition was implemented, along with a new fixed heat flux boundary condition. The detail of this work is presented in Appendix B.

3.1.1 Improved HTC model

The method proposed for FENSAP-ICE is not always valid. By definition, if an adiabatic wall is assumed ($\dot{Q}_{wall} = 0$), the wall temperature is the recovery temperature or adiabatic wall temperature ($T_{wall} = T_{rec}$). However, applying an adiabatic wall to Eq. (2.19)

$$\dot{Q}_{wall} = HTC(T_{wall} - T_{\infty}) \rightarrow HTC = \frac{\dot{Q}_{wall}}{T_{wall} - T_{\infty}} \qquad \text{(2.19 revisited)}$$

gives

$$T_{wall} = T_{\infty}. \qquad (3.1)$$

This is only true for negligible viscous dissipation and zero pressure gradient. In the presence of a curved body (e.g. an airfoil) and with negligible viscous dissipation, one must use the temperature at the edge of the boundary layer (T_e), not the freestream temperature (T_∞). Eq. (2.19) becomes:

$$HTC = \frac{\dot{Q}_{wall}}{T_{wall} - T_e} \tag{3.2}$$

If viscous dissipation cannot be neglected, then the recovery temperature must be used, Eq. (2.19) becomes:

$$HTC = \frac{\dot{Q}_{wall}}{T_{wall} - T_{rec}} \tag{3.3}$$

where

$$T_{rec} = T_e + r\frac{U_e^2}{2C_p} = T_e\left(1 + r\frac{\gamma - 1}{2}M_e^2\right) \tag{3.4}$$

and r is the recovery factor.

Thus in NSCODE-ICE, $\dot{Q}_{wall}$ is computed from Eq. (3.5) and the Convective Heat Transfer Coefficient is computed from Eq. (3.3).

$$\dot{Q}_{wall} = k_a \left.\frac{dT}{d\vec{n}}\right|_{wall} = Cp\left(\frac{\mu_l}{Pr_l} + \frac{\mu_t}{Pr_t}\right)\left.\frac{dT}{d\vec{n}}\right|_{wall} \tag{3.5}$$

The recovery temperature is evaluated by Eq. (3.4) with r taken as a fully turbulent recovery factor ($r = Pr^{1/3}$). U_e and M_e are computed from the isentropic relations (Anderson, 2011):

$$U_e = M_e\sqrt{\gamma R T_e} \tag{3.6}$$

$$M_e = \sqrt{\frac{2}{\gamma - 1}\left(\left(\frac{P_0}{P_e}\right)^{\frac{\gamma-1}{\gamma}} - 1\right)} \tag{3.7}$$

$$T_e = T_0\left(\frac{P_e}{P_0}\right)^{\frac{\gamma-1}{\gamma}} \tag{3.8}$$

where P_0 and T_0 are the total conditions and P_e is the pressure at the edge of the boundary layer which is taken equal to the wall pressure ($\frac{\partial P}{\partial \vec{n}} = 0$ in the boundary layer).

$$P_0 = P_\infty\left(1 + \frac{\gamma - 1}{2}M_\infty^2\right)^{\frac{\gamma}{\gamma-1}} \tag{3.9}$$

$$T_0 = T_\infty\left(1 + \frac{\gamma - 1}{2}M_\infty^2\right) = T_\infty\left(\frac{P_0}{P_\infty}\right)^{\frac{\gamma-1}{\gamma}} \tag{3.10}$$

Finally, the convective heat flux used in the thermodynamic model is computed from:

$$\dot{Q}_{conv} = HTC(T_{surf} - T_{rec}) \tag{3.11}$$

This new formulation is similar to the ONERA method, the main difference being that the recovery temperature is computed from the analytical relation (3.4) instead of evaluated from the two flow solutions.

3.1.2 Correction to the Energy Balance

With the current method, the convective heat transfer is computed using the recovery temperature (T_{rec}) whereas the classic heat balance uses the freestream temperature (T_∞). The classic energy balance is recalled to be:

$$\dot{Q}_{kin} + \dot{Q}_{ice} + \dot{Q}_f + \dot{Q}_{in} + \dot{Q}_{st} = \dot{Q}_{conv} + \dot{Q}_{rad} + \dot{Q}_{es} + \dot{Q}_{imp} + \dot{Q}_{out} \tag{2.27 revisited}$$

using:

$$\dot{Q}_{conv} = HTC(T_{surf} - T_\infty) \tag{3.12}$$

$$\dot{Q}_f = HTC\frac{rU_\infty^2}{2C_{p,a}} \tag{3.13}$$

These relations are based on a flat plate assumption, hence $T_e = T_\infty$ and $U_e = U_\infty$. Combining the aerodynamic heating ($\dot{Q}_f$) and the heat transfer by convection ($\dot{Q}_{conv}$), the convective heat flux based on T_{rec} is found:

$$\dot{Q}_{conv} - \dot{Q}_f = HTC\left(T_{surf} - T_e - \frac{rU_e^2}{2C_{p,a}}\right) \tag{3.14}$$

$$\dot{Q}_{conv} - \dot{Q}_f = HTC\left(T_{surf} - T_{rec}\right) \tag{3.15}$$

It is observed that Eq. (3.15) is equivalent to Eq. (3.11). With the current method, $\dot{Q}_{conv}$ already accounts for the aerodynamic heating ($\dot{Q}_f$), hence $\dot{Q}_f$ is removed from the energy balance.

$$\dot{Q}_{kin} + \dot{Q}_{ice} + \dot{Q}_{in} + \dot{Q}_{st} = \dot{Q}_{conv} + \dot{Q}_{rad} + \dot{Q}_{es} + \dot{Q}_{imp} + \dot{Q}_{out} \tag{3.16}$$

3.1.3   Verification and Validation for the HTC

The evaluation of the convective heat transfer coefficient is highly dependent on the accuracy of the flow solution and on the surface roughness. Hence the flow solver has been validated on a laminar flat plate (Blasius solution) and the turbulence model (Spalart-Allmaras (SA)) has been verified on a fully turbulent smooth flat plate using the NASA Turbulence Modeling Resource (NAS). For conciseness, these results are not presented in this thesis. Instead, this section demonstrates the validity of the turbulence model for the evaluation of the convective heat transfer on rough surfaces. Results are presented for a fully turbulent rough flat plate and compared against experimental and empirical data. A verification against LEWICE is also presented for an airfoil.

Turbulent Flat Plate – Empirical Correlation

In order to validate the SA turbulence model with rough wall treatment, the friction coefficient is first verified against an empirical correlation derived by Mills and Hang (1983) which holds for a fully rough flat plate ($k_s^+ \geq 60$).

$$C_f = \left[3.476 + 0.707 ln\left(\frac{x}{k_s}\right)\right]^{-2.46} \tag{3.17}$$

where k_s is the equivalent sand grain roughness height and $k_s^+ = \mu_t k_s/\nu$.

The test case is a zero incidence, zero pressure gradient flat plate with a rough surface. The flat plate is $2m$ long and there is a $0.25m$ buffer zone in front of the plate. The fluid domain is $1m$ high and the grid used has 253 in i and 145 nodes in j with $y^+ \approx 0.1$. The same results were achieved with a finer mesh (721×385 nodes).

For the boundary conditions, there is an engine inlet with a specified total pressure ratio $P_{tot}/P_\infty = 1.02828$ and total temperature ratio $T_{tot}/T_\infty = 1.008$. The outlet boundary condition is a pressure outlet with $P/P_\infty = 1$. The flat plate has a viscous wall boundary condition and the buffer zone has a symmetry boundary condition in front of the plate. The upper edge of the fluid domain is set as a farfield (inflow/outflow).

Figure 3.1 shows the friction coefficient for various roughness heights. Note that the k_s^+ as shown in the legend is the minimum over the range $x \in [0,1]$. The results are presented for two types of boundary conditions. Figure 3.1a uses a subsonic inlet ($P_{tot}/P_\infty = 1.02828$ and $T_{tot}/T_\infty = 1.008$) and a pressure outlet ($P/P_\infty = 1.0$). However, better results are achieved with inflow/outflow farfield condition at the inlet and outlet (Figure 3.1b). The flow density residual is reduced by 5 orders of accuracy. It is concluded that the evaluation

of friction coefficient according to a variation of surface roughness is good as it closely follows the empirical relation.
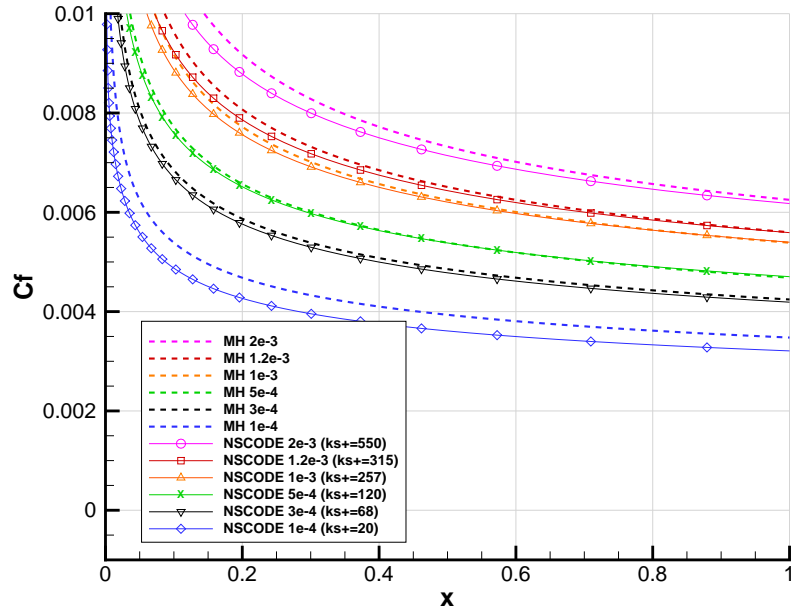
(a) Subsonic inflow and pressure outlet
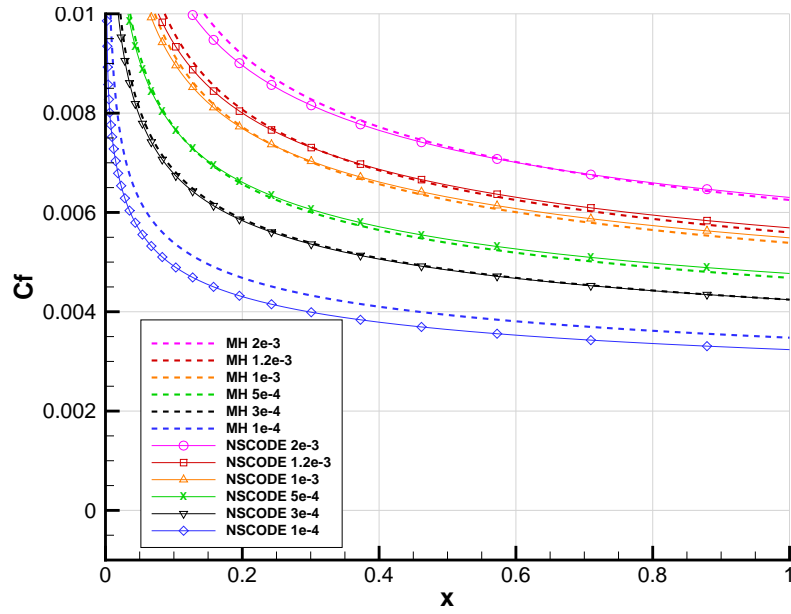
(b) Farfield (Inflow/outflow)

Figure 3.1 C_f on a fully rough flat plate for two types of boundary conditions

Turbulent Flat Plate – Experimental Results

Second, the Stanton number is validated against the experimental data of Hosni et al. (1991) and verified against the numerical results of Aupoix and Spalart (2003). The numerical results of Aupoix and Spalart (2003) are presented for the SA model with the roughness extension of Boeing and ONERA. The equivalent sand grain roughness (k_s) is evaluated from Dirling's correlation as summarized by Aupoix and Spalart (2003). The simulation parameters are listed in Table 3.1. For this test case, $T_{wall} = 1.05T_\infty$ is used.

Table 3.1 Simulation parameters for a fully rough flat plate (roughness spacing ratio $L/d = 4$ and $U_\infty = 58m/s$)

Re	$Mach$	$T\ [K]$	$P\ [Pa]$	$k_s\ [m]$
3.698E06	0.167	300	101325	1.89e-04

The Stanton number is defined as:

$$St = \frac{HTC}{\rho_\infty U_\infty C_p} \tag{3.18}$$

and is computed using $U_\infty = 58\,m/s$, $\rho_\infty = 1.177\,kg/m^3$ and $Cp = 1005\,J/(kg\,K)$ for this test case. The Convective Heat Transfer Coefficient is an output of the Navier-Stokes flow solver. Also, an empirical relation is provided by Hosni et al. (1991) to obtain the results for the smooth flat plate:

$$St = 0.185\,(log_{10}Re_x)^{-2.584}\,Pr^{-0.4} \tag{3.19}$$

where the Prandtl number is taken as $Pr = 0.729$.

The results are presented in Figure 3.2. Note that NSCODE uses the SA model with Boeing's extension. In Figure 3.2a, the grid used is 625×289 nodes for a $2.4m$ long flat plate, a $1m$ high fluid domain and a $0.25m$ long buffer zone forward of the flat plate. Also, the flow density residual reduced by 6 orders of accuracy. The solution is in good agreement with the experimental and numerical data for both the rough and smooth case with a maximum error of $\approx 4.5\%$.

In Figure 3.2b, y_{wall} was increased to obtain $y^+ \approx 1$. This resulted in a grid with 529×225 nodes and a solution with a maximum error of $\approx 6.0\%$. Usually when computing airflow solution around airfoil, we aim for $y^+ < 3$. However, when evaluating the heat transfer at the wall, a gain in accuracy is achieved if $y^+ \leq 0.1$ as can be seen by comparing Figure 3.2a and Figure 3.2b.
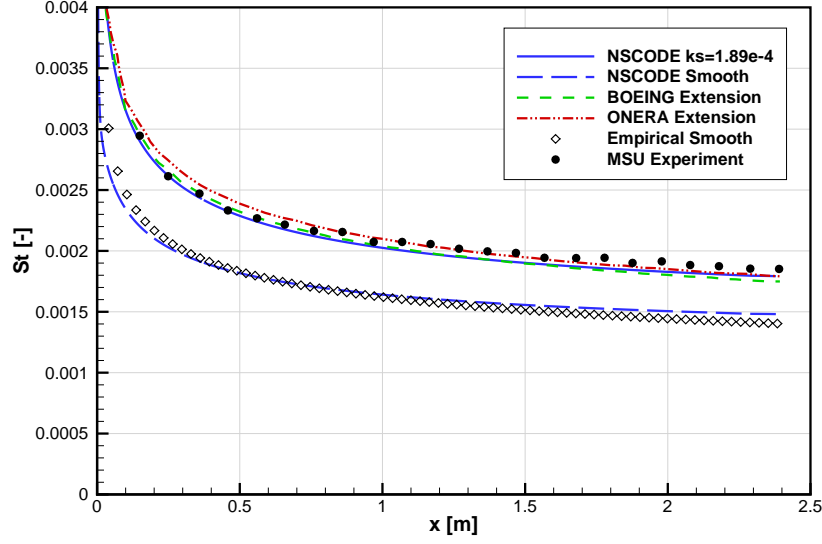
(a) $y^+ \approx 0.1$
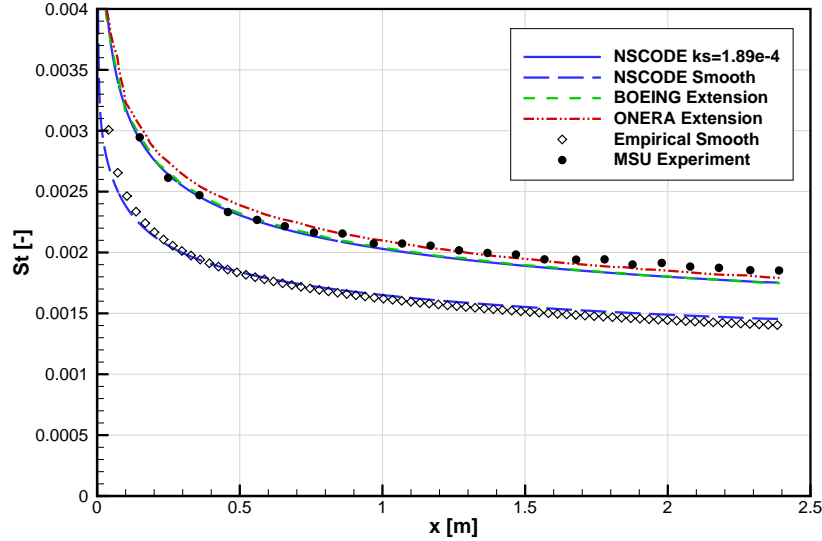
(b) $y^+ \approx 1$

Figure 3.2 Stanton number for a fully rough flat plate

Verification on an Airfoil

Validation data is available from the two supplementary CD-ROMs containing the experimental data and numerical results for LEWICE 2.0 (Wright and Rutkowski, 1999). Select test cases and their parameters are presented in Table A.1. All cases are run using the SA one-equation turbulence model and Boeing's extension to account for the wall roughness (Spalart (2000), Aupoix and Spalart (2003)). Note that for the case 421 and 425 presented in Figures 3.4 and 3.3, the equivalent sandgrain roughness is used as given in the CD-ROMS

to allow a fair comparison with the HTC curves. k_s is respectively $701.6\mu m$ and $335.4\mu m$ for case 421 and 425.

The numerical Convective Heat Transfer Coefficient from LEWICE is compared to NSCODE-ICE in Figure 3.3. Since the current method requires that a temperature is imposed at the wall, the figure also exhibits the effect from a variation of T_{wall} (ranging from $0.85T_\infty$ to $1.15T_\infty$). The curve in light orange, labeled $T_{wall} = 1.01T_\infty$ for the case 421 and case 425, does not follow the general trend compared to the other curves. Interestingly, the recovery temperature is approximately $270K$ and $246K$ respectively for case 421 and 425, which is within 0.4% of the fixed wall temperature. It suggests that the fixed wall temperature should not be too close to the recovery temperature to provide a good estimate of the HTC. Furthermore, T_{wall} should not be too far from T_{rec} since the purpose is to estimate the HTC of an adiabatic wall. For the current method, the wall temperature is typically fixed to $T_{wall} = 1.05T_\infty$ as to respect both constraints. Results using this boundary conditions follow the same trend as LEWICE (Figure 3.3) and match with the experimental results for the rough flat plate tested earlier (Figure 3.2). The fixed wall temperature is still case dependent since it seems to be linked with T_{rec} and should be adjusted by the user if needed.

Figure 3.4 illustrates the ice shape variation corresponding to the wall temperatures imposed. The effect on the rime ice shape is negligible while a slight variation is observed for the glaze ice shape. Again, the light orange curve differs from the other ice shape since its wall temperature is too close to the recovery temperature.
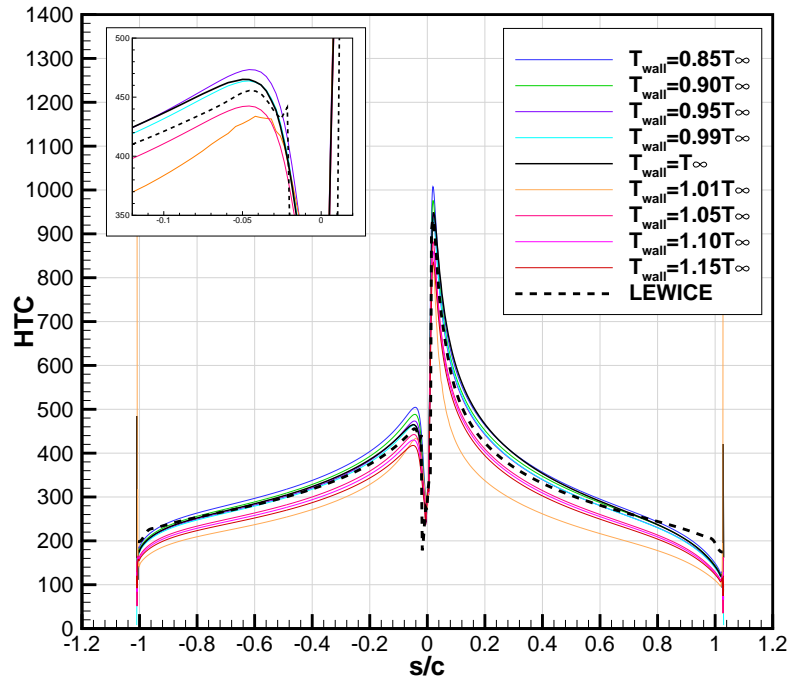
(a) Case 421 – glaze ice
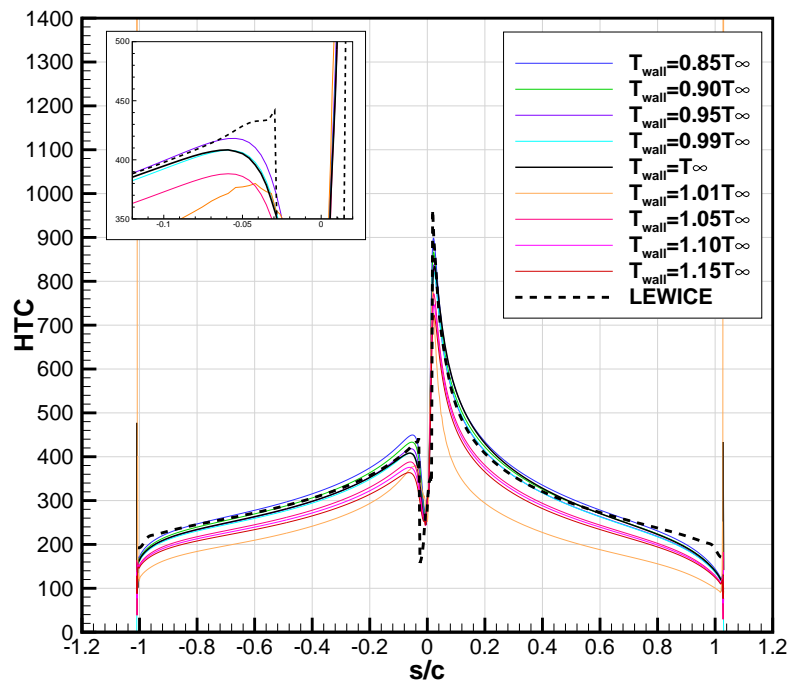
(b) Case 425 – rime ice

Figure 3.3 Convective heat transfer coefficient compared to LEWICE results (Wright and Rutkowski, 1999)
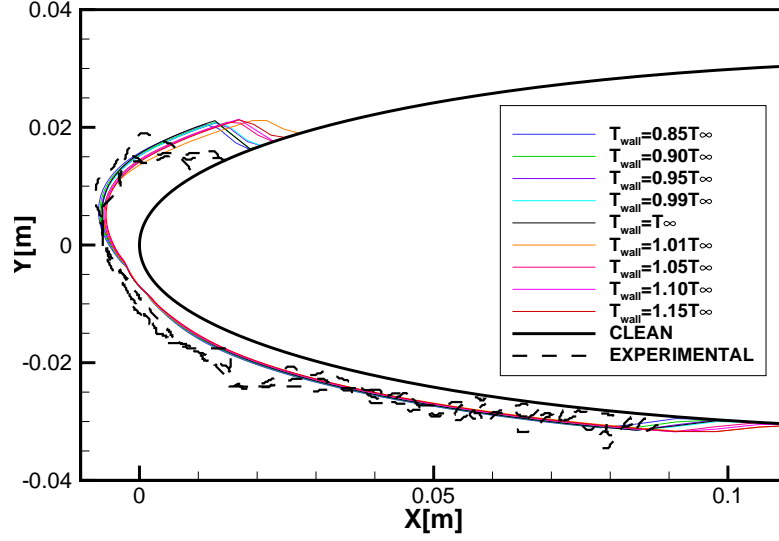
(a) Case 421 – glaze ice
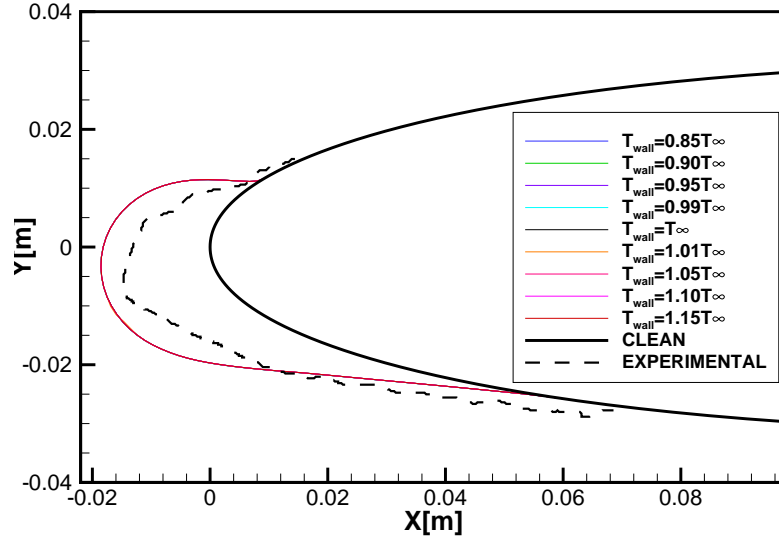
(b) Case 425 – rime ice

Figure 3.4 Predicted ice shapes for various fixed wall temperatures (Case 421 and 425) – Single Layer

3.1.4 Infinite Swept Wing Effects

The airflow on airfoils is characterized by the presence of a stagnation point in the leading edge region. At this point the velocity is null and a positive pressure peak is present. Close to the wall, the air is typically flowing from the stagnation point towards the trailing edge. It is difficult to evaluate the HTC at the stagnation point using IBL methods where a special treatment is required. The newly implemented RANS based method handle the stagnation

area automatically if a good mesh is provided.

On swept wings, the stagnation point is replaced by a stagnation line, where there is an airflow component in the spanwise direction, a crossflow. Hence, the non-zero velocity at the stagnation line induce a higher HTC compared to a stagnation point. Usual methods to simulate ice accretion on swept-wings (e.g. the correction of Dorsch and Brun (1953)) do not account for the effect of the stagnation line on the HTC. A purely two-dimensional method has no information about the crossflow component and thus the correction methods lack a fair modeling of the HTC. This is evidenced by Hedde and Guffond (1995) who state that the HTC is the missing part of the puzzle while simulating ice accretion on swept wings using a 2D solver.
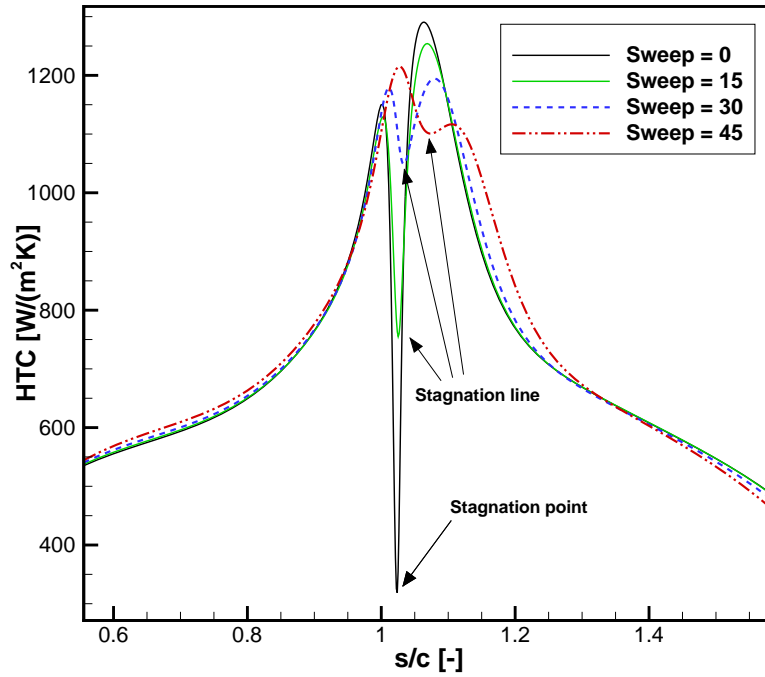
Figure 3.5 HTC comparison on the MS317 infinite swept wing for $\Lambda = 0°$, $15°$, $30°$ and $45°$ (case 3)

The 2.5D approach has one significant advantage over typical correction methods. The stagnation line is simulated and, by using the 2.5D approach combined with the current RANS-based convective heat transfer coefficient evaluation model, the HTC is directly evaluated accounting for the crossflow component. Figure 3.5 demonstrates the increase in HTC from a purely 2D simulation with a stagnation point to a $45°$ swept-wing simulation with a stagnation line (2.5D approach).

3.2 Roughness Model

Ideally, an icing software is fully automatic and the user only have to provide the geometry and the ambient conditions. However, the surface roughness is generally not a given parameters for icing simulations. In NSCODE-ICE, as of 2015, the surface roughness was user defined only, implying that an experienced user was needed to correctly estimate the required roughness. As an attempt to automatize the process, a simple empirical surface roughness model is implemented. The equivalent sand grain roughness model of Shin et al. (1991) provides a constant roughness over the surface given the Liquid Water Content (LWC), the air temperature (T_∞), the airspeed (U_∞), the Median Volume Diameter (MVD) and the chord (c). The empirical relation is as follows:

$$k_s = \left[\frac{k_s/c}{(k_s/c)_{base}}\right]_{LWC} \cdot \left[\frac{k_s/c}{(k_s/c)_{base}}\right]_{T_\infty} \cdot \left[\frac{k_s/c}{(k_s/c)_{base}}\right]_{U_\infty} \cdot \left[\frac{k_s/c}{(k_s/c)_{base}}\right]_{MVD} \cdot \left(\frac{k_s}{c}\right)_{base} \cdot c \quad (3.20)$$

where

$$
\begin{aligned}
\left(\frac{k_s}{c}\right)_{base} &= 0.001177 \\
\left[\frac{k_s/c}{(k_s/c)_{base}}\right]_{LWC} &= 0.5714 + 0.2457(LWC) + 1.2571(LWC)^2 \\
\left[\frac{k_s/c}{(k_s/c)_{base}}\right]_{T_\infty} &= 0.047T_\infty - 11.27 \\
\left[\frac{k_s/c}{(k_s/c)_{base}}\right]_{U_\infty} &= 0.4286 + 0.0044139U_\infty \\
\left[\frac{k_s/c}{(k_s/c)_{base}}\right]_{MVD} &= \begin{cases} 1 & MVD \le 20 \\ 1.667 - 0.0333(MVD) & MVD > 20 \end{cases}
\end{aligned}
\quad (3.21)
$$

As stated by Shin et al. (1991), best results are achieved by using $k_{s,corr} = 2k_s$. NSCODE-ICE currently uses the corrected surface roughness value ($k_{s,corr}$). The software also takes user defined roughness values. Although this is not a sophisticated model, this is a significant improvement for the software. The ice shapes generated using the roughness from this model are generally in good agreement with the experimental shapes. If required, the roughness can be adapted knowing the initial guess provided by the current model.

3.3 Supercooled Large Droplets

To adequately represent the physics of Supercooled Large Droplets many new features are required. First, the droplets field is often assumed to be composed of a single size of droplets defined by the MVD for icing simulations. However, as the MVD increases, the contribution of the smaller and larger droplets forming the cloud become important. The spectrum of droplets sizes widen as well. Second, when the droplets sizes or diameters increase, they can no longer be considered as a spherical droplets. Thus, their deformation have to be considered. Third, as the droplets sizes increase, additional phenomena appear such as breakup of the larger droplets into smaller ones, splashing of the droplets impacting the surface where not all the water sticks to the wall, rebound and spreading. As observed by Hospers (2013), the features having the largest impact for the modeling of SLD are, from the most significant to the least:

1. droplet size distribution;
2. splashing;
3. droplet deformation;
4. rebound.

In NSCODE-ICE, the droplet size distribution is implemented first since it has a significant influence on the catch efficiency, even for SSD regime (MVD of the order of $25\mu m$). Then a droplet deformation model is added to make the code more general. A basic splashing model is still needed to account for the second most important effect, as well as a rebound model.

3.3.1 Droplets Size Distribution

To handle a given distribution of droplet sizes, the droplet field is solved for each droplet size. For each run, the collection efficiency (β), the droplets impingement rate ($\dot{m}_{imp}$) and the droplets impacting velocity (U_d) are saved. Then, the global solution is obtained by a weighted average of each solution (Papadakis et al., 2007).

$$\beta = \frac{1}{LWC} \sum_{i=1}^{Ndrop} (\beta_i \, \omega_i) \tag{3.22}$$

$$\dot{m}_{imp} = \beta \, LWC \, U_\infty \, ds \tag{3.23}$$

$$\dot{Q}_{imp} = \sum_{i=1}^{Ndrop} \left(\beta_i \omega_i U_\infty \, ds \frac{U_{di}^2}{2} \right) \tag{3.24}$$

where ω_i is a weighting factor representing the fraction of LWC for a specific droplet size. The distribution is usually defined by the droplets sizes, either in dimensional or non-dimensional form, and the fraction of Liquid Water Content (%LWC) of each drop size. The %LWC represents the concentration of water of a specific droplet size compared to the bulk water concentration of the droplets cloud ($100\omega_i/LWC$). The number of droplet diameters in the distribution is denoted by $Ndrop$ and the distributions are usually labeled as $Ndrop-bin$. The Langmuir D distribution (Table 3.2) is widely used to represent the droplets distribution when it is not specified and/or no knowledge is available about the distribution. It is used as a generic distribution in NSCODE-ICE.

Table 3.2 Definition of the Langmuir D distribution in term of the LWC fraction (%LWC) and the non-dimensional droplet size

%LWC	D/MVD
5.00	0.31
10.00	0.52
20.00	0.71
30.00	1.00
20.00	1.37
10.00	1.74
5.00	2.22

3.3.2 Droplets Drag Model

In SLD regime, the assumption that the droplets remain spherical is no longer valid. To account for the droplets deformation a new droplet drag model is implemented. The drag coefficient of the deformed droplet can be evaluated by interpolating the drag for a sphere and an oblate disk (Honsek et al., 2008):

$$C_D = \begin{cases} (1-f)C_{Dsphere} + fC_{Ddisk} & We \leq 12 \\ C_{Ddisk} & We > 12 \end{cases} \tag{3.25}$$

with

$$f = 1.0 - \left(1.0 + 0.07\sqrt{We}\right)^{-6}. \tag{3.26}$$

The drag coefficient for the sphere and the oblate disk are summarized from Clift et al. (1978):

$$C_{Ddisk} = \begin{cases} \frac{64}{\pi Re_d}\left(1 + \frac{Re_d}{2\pi}\right) & if \quad Re_d \leq 0.01 \\ \frac{64}{\pi Re_d}\left(1 + 10^{(-0.883+0.906w-0.025w^2)}\right) & if \quad 0.01 < Re_d \leq 1.5 \\ \frac{64}{\pi Re_d}\left(1 + 0.138Re_d^{0.792}\right) & if \quad 1.5 < Re_d < 133 \\ 1.17 & if \quad Re_d \geq 133 \end{cases}$$ (3.27)

$$C_{Dsphere} = \begin{cases} 0.1875 + \frac{24}{Re_d} & if & Re_d \leq 0.01 \\ \frac{24}{Re_d}\left(1 + 0.1315Re_d^{(0.82-0.05w)}\right) & if & 0.01 < Re_d \leq 20 \\ \frac{24}{Re_d}\left(1 + 0.1935Re_d^{0.6305}\right) & if & 20 < Re_d \leq 260 \\ 10^{(1.6435-1.1242w+0.1558w^2)} & if & 260 < Re_d \leq 1500 \\ 10^{(-2.4571+2.5558w-0.9295w^2+0.1049w^3)} & if & 1500 < Re_d \leq 1.2 \times 10^4 \\ 10^{(-1.9181+0.6370w-0.0636w^2)} & if & 1.2 \times 10^4 < Re_d \leq 4.4 \times 10^4 \\ 10^{(-4.3390+1.5809w-0.1546w^2)} & if & 4.4 \times 10^4 < Re_d \leq 3.38 \times 10^5 \\ 29.78 - 5.3w & if & 3.38 \times 10^5 < Re_d \leq 4 \times 10^5 \\ 0.1w - 0.49 & if & 4 \times 10^5 < Re_d \leq 10^6 \\ 0.19 - \frac{8 \times 10^4}{Re_d} & if & Re_d > 10^6 \end{cases}$$ (3.28)

where $w = \log(Re_d)$ and Re_d is the droplet Reynolds number:

$$Re_d = \frac{\rho_a ||\vec{u}_a - \vec{u}_d|| MVD}{\mu_a}.$$ (3.29)

The Weber number is defined as:

$$We = \frac{\rho_a ||\vec{u}_a - \vec{u}_d||^2 MVD}{\sigma_w}$$ (3.30)

where σ_w is the surface tension at the water-air interface.

3.3.3 Validation and Verification

A validation of the implementations can be made by comparing with the experimental data of Papadakis et al. (2007) who also provide the numerical results of LEWICE without SLD model (splashing and rebound are not modeled). The MS-317 airfoil is chosen for this validation where the parameters used for the simulation are summarized in Table 3.3 below.

Table 3.3 Parameters for the validation of the droplets distribution

Geometry	MS(1)-317 (sharp trailing edge)
Chord	0.9144 m
Reynolds	4.83×10^6
Mach	0.23
MVD	11 μm to 168 μm
Bin Size	1 and 27
Freestream Pressure	97.0 kPa
Freestream Temperature	283.15 K
Sweep angle	0°

The results are presented in Figure 3.6, where both the droplet distribution and extended drag model were activated. The Langmuir D distribution is used throughout this thesis since for most cases, no knowledge of the cloud of droplets is available. In this section, the droplets distribution as provided by Papadakis et al. (2007) are used to provide a fair comparison.

It is observed that the use of a droplets distribution increases the width of the impingement limits, as expected. In the leading edge region, the maximum catch efficiency (β) is reduced. Both these behaviors improve the solution compared to experimental results, especially for a MVD of $11\mu m$ and $21\mu m$. For larger droplet diameters, the catch limits are too wide and the maximum catch efficiency (β) is too high compared to the experiment. This is expected since the SLD effects such as splashing and rebound of the droplets are not considered. Moreover, NSCODE-ICE performs in a similar manner than LEWICE for all the cases tested (see Table 3.3), verifying the implementation.

In terms of computation time, the addition of droplet sizes implies running the droplets solver for each drop size. The solution are obtained sequentially, with the next simulation initialized with the previous solution. In theory, this process slightly reduces the computation time compared to resetting the solution for each drop size. However, numerically, the computation time for 27 droplet sizes is roughly 27 times longer than for a single droplet size as shown in Table 3.4. Hence, more work would be required to optimize the solving process.

Table 3.4 CPU times comparison for the droplets distributions

MVD [μm]	1-bin	27-bin	Ratio
11	32.11s	726.83s	22.64
21	27.55s	655.63s	23.79
79	25.11s	775.25s	30.87
137	27.65s	759.88s	27.48
168	29.01s	821.62s	28.32

The use of a droplets distribution instead of a mono-dispersed droplets size does not only affect the SLD regime ($MVD > 40\mu m$) but also the smaller droplets cloud (e.g. $MVD = 11\mu m$ and $MVD = 21\mu m$). For the remainder of this thesis, the Langmuir D distribution will be used to account for the variation of droplets diameter in typical icing clouds and experimental apparatus. The extended drag model will also be used as it is valid for both SLD and SSD regimes.
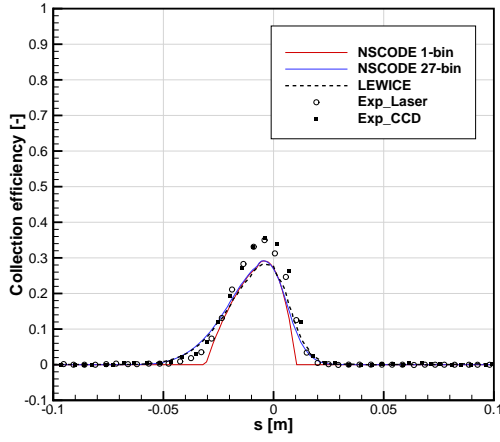
(a) MVD = 11μm
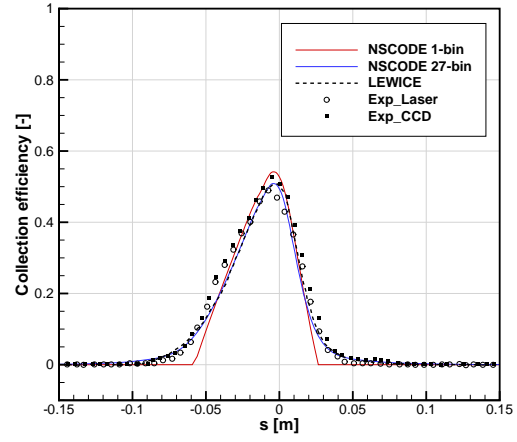
(b) MVD = 21μm
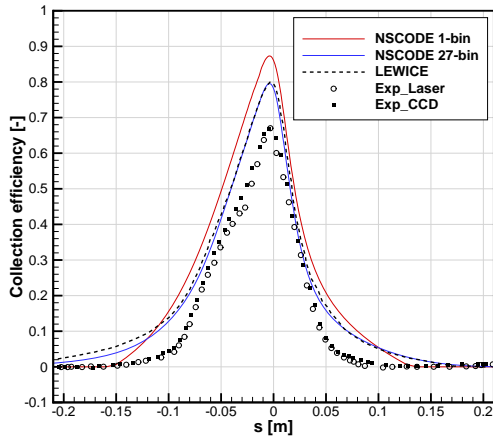
(c) MVD = 79μm
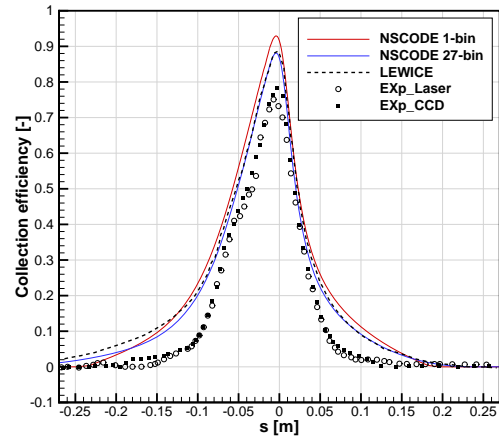
(d) MVD = 137μm
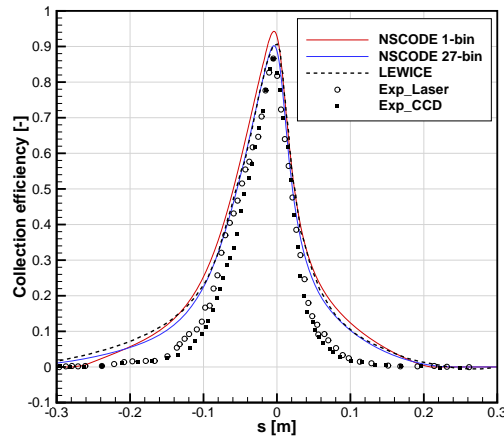
(e) MVD = 168μm

Figure 3.6 Validation of the droplets distribution implementation

CHAPTER 4   THERMODYNAMIC MODEL

The thermodynamic module is responsible for evaluating the ice thickness, the water film height and the temperature of the surface. The first thermodynamic model added to NSCODE-ICE (in 2015) is based on the work of Zhu et al. (2012). In this thesis, it is referred to as the Iterative Messinger model. It is derived from the classical Messinger model and differs by the addition of an iterative loop to solve for the runback water directions. The runback water is driven by the air shear stress at the surface of the water film and its motion is not dependent on the location of the stagnation point. However, it does not consider water accumulation into the control cell, there is no modeling of the conduction through the ice and water layer and the model uses an algebraic formulation.

In this research, it is intended to implement a thermodynamic model which is:

- applicable to any geometries (not stagnation point dependent);

- easily extensible to a three-dimensional formulation;

- accurately models the physics of water films, particularly for in-flight icing;

- time dependent to allow more flexibility in the physics modeled.

Four thermodynamic models were implemented in NSCODE-ICE and compared under different aspects (Lavoie et al., 2017). A summary of the features for each model is presented in Table 4.1. In terms of runback water the Messinger (Messinger, 1953) and Extended Messinger models (Myers, 2001) use the location of the stagnation point to determine the water runback direction. With these models the water film flows from the stagnation point towards the trailing edge of the airfoil. On the other hand, the SWIM (Bourgault et al., 2000) and Iterative Messinger model (Zhu et al., 2012) use the wall shear stress to determine the direction of the water film. This approach is more automatic and more adequate for a parallel implementation. It is also easier to extend these models for three-dimensional applications.

Table 4.1 Thermodynamic Models Comparison

	Messinger	Iterative Messinger	Extended Messinger	SWIM
Conduction Through Ice	no	no	yes	no
Water Accumulation	no	yes	no	yes
Runback Water Direction	stagnation point	shear stress	stagnation point	shear stress
Formulation	Algebraic	Algebraic	ODE	PDE
State	steady	steady	unsteady	unsteady

The Shallow Water Icing Model (SWIM) is selected for the final implementation since it provides most of the desired features. Also, it is PDE-based which follows the trend of the recent development in the field and is in line with the philosophy of second generation icing software. In this chapter, a description of the model is presented first, along with details about its implementation in NSCODE-ICE. Further developments are also presented to improve the SWIM according to recent literature findings.

4.1 Implementation of the Shallow Water Icing Model

The SWIM is a Partial Differential Equation based model introduced by Bourgault et al. (2000) and follows lubrication theory. It assumes that the water film velocity (u) is a function of τ_{wall} and y (the direction normal to the wall). In order to simplify the model, a linear velocity profile is assumed in y with a no slip condition at the wall ($y = 0$):

$$u(\mathbf{x}, y) = \frac{y}{\mu_w} \tau_{wall}(\mathbf{x}).$$

where $\mathbf{x} = (x_1, x_2)$ represent the curvilinear coordinates on the surface and y is in the direction normal to the wall. The velocity is averaged in y to give $\bar{u}$:

$$\bar{u}(\mathbf{x}) = \frac{h_w}{2\mu_w} \tau_{wall}(\mathbf{x}). \tag{4.1}$$

The mass and energy conservation equations in PDE formulation become:

$$\rho_w \left[\frac{\partial h_w}{\partial t} + \text{div}(\bar{u} h_w) \right] = \dot{m}_{imp} - \dot{m}_{ice} - \dot{m}_{es} \tag{4.2}$$

$$\rho_w \left[\frac{\partial h_w C_{p,w} \bar{T}}{\partial t} + \text{div}(\bar{u} h_w C_{p,w} \bar{T}) \right] = \dot{Q}_{kin} + \dot{Q}_{ice} - \dot{Q}_{imp} - \dot{Q}_{es} - \dot{Q}_{rad} - \dot{Q}_{conv} \tag{4.3}$$

where $\bar{T} = T_{surf} - T_{ref}$ and

$$
\dot{Q}_{es} = \begin{cases} \dot{Q}_{ev} & if \quad T_{surf} >= 0 \\ \dot{Q}_{su} & if \quad T_{surf} < 0 \end{cases} \tag{4.4}
$$

$$
\dot{Q}_{rad} = \sigma_r \varepsilon (T_{surf}^4 - T_\infty^4) \tag{4.5}
$$

The energy terms were defined earlier in Table 2.1. Finally the following compatibility relations complete the model:

$$
\left. \begin{array}{cc} h_w \geq 0 & \dot{m}_{ice} \geq 0 \\ h_w \bar{T} \geq 0 & \dot{m}_{ice} \bar{T} \leq 0 \end{array} \right\} \tag{4.6}
$$

These compatibility relations ensure that the solution has a positive water film thickness h_w and no melting of the ice. This condition does not hinder anti-icing simulations where ice accumulation is prevented. However, for de-icing simulations, the condition imposing a non-melting ice would need to be adapted. Next, if there is a water film, the surface temperature is greater or equal to the fusion temperature of water (T_{ref}). Finally, if ice accretion occurs, the surface temperature must be below or equal to T_{ref}.

The SWIM can be written in a more compact form:

$$
\frac{\partial \mathbf{W}}{\partial t} + \nabla \cdot \mathbf{F} = \mathbf{S} \tag{4.7}
$$

where

$$
\mathbf{W} = \rho_w \begin{pmatrix} h_w \\ h_w C_{p,w} \bar{T} \end{pmatrix}, \quad \mathbf{F} = \rho_w \begin{pmatrix} \bar{u} h_w \\ \bar{u} h_w C_{p,w} \bar{T} \end{pmatrix} \tag{4.8}
$$

$$
\mathbf{S} = \begin{pmatrix} \dot{m}_{imp} - \dot{m}_{ice} - \dot{m}_{es} \\ \dot{Q}_{drop} + \dot{Q}_{ice} + \dot{Q}_f - \dot{Q}_{es} - \dot{Q}_{rad} - \dot{Q}_{conv} \end{pmatrix} \tag{4.9}
$$

In NSCODE-ICE, the SWIM is solved for the water height (h_w), the ice height (h_{ice}) and the scaled surface temperature ($\bar{T}$). Since h_{ice} is hidden in the source terms $\dot{m}_{ice}$ and $\dot{Q}_{ice}$, they are developed:

$$
\dot{m}_{ice} = \rho_{ice} \frac{\partial h_{ice}}{\partial t} \tag{4.10}
$$

$$
\dot{Q}_{ice} = \rho_{ice} \frac{\partial h_{ice} (L_{fus} - C_{p,ice} \bar{T})}{\partial t}. \tag{4.11}
$$

Then the source term is split in $\mathbf{S} = \frac{\partial \mathbf{S}_{ice}}{\partial t} + \mathbf{S}_0$, with:

$$\mathbf{S}_{ice} = \rho_{ice} \begin{pmatrix} -h_{ice} \\ h_{ice}(L_{fus} - C_{p,ice}\bar{T}) \end{pmatrix} \quad and \quad \mathbf{S}_0 = \begin{pmatrix} \dot{m}_{imp} - \dot{m}_{es} \\ \dot{Q}_{drop} + \dot{Q}_f - \dot{Q}_{es} - \dot{Q}_{rad} - \dot{Q}_{conv} \end{pmatrix}$$
(4.12)

Finally, Eq. (4.7) is recast by defining $\mathbf{W}^* = \mathbf{W} - \mathbf{S}_{ice}$.

$$\frac{\partial \mathbf{W}}{\partial t} + \nabla \cdot \mathbf{F} = \frac{\partial \mathbf{S}_{ice}}{\partial t} + \mathbf{S}_0 \quad \rightarrow \quad \frac{\partial \mathbf{W}^*}{\partial t} + \nabla \cdot \mathbf{F} = \mathbf{S}_0$$
(4.13)

The system is discretized using a cell-centered Finite Volume Method (FVM) which use the integral form of the conservative law. The computational domain is divided in control volumes (Ω_i) where the volume is assumed to be constant over time. In addition, the properties are assumed to be constant over a control volume, which means $\mathbf{W}^*$, $\mathbf{F}$ and $\mathbf{S}_0$ are constant per control volume. Eq. (4.13) is integrated for each control volume to give:

$$\int_\Omega \frac{\partial \mathbf{W}^*}{\partial t} d\Omega + \int_\Omega \nabla \cdot \mathbf{F} d\Omega = \int_\Omega \mathbf{S}_0 d\Omega$$
(4.14)

$$\Omega \frac{\partial \mathbf{W}^*}{\partial t} + \int_\Omega \nabla \cdot \mathbf{F} d\Omega = \Omega \mathbf{S}_0$$
(4.15)

The divergence theorem is applied to the flux term:

$$\int_\Omega \nabla \cdot \mathbf{F} d\Omega = \oint_{d\Omega} \mathbf{F} \cdot \mathbf{n}\, dS$$
(4.16)

$$\Omega \frac{\partial \mathbf{W}^*}{\partial t} + \oint_{d\Omega} \mathbf{F} \cdot \mathbf{n}\, dS = \Omega \mathbf{S}_0$$
(4.17)

where dS represent the area of a faces for the control volume. For a control volume i, the system becomes:

$$\frac{d\mathbf{W}^*_i}{dt} + \frac{1}{\Omega_i} \sum_{m=1}^{N_{face}} (\mathbf{F} \cdot \mathbf{n}\, S)_m = \mathbf{S}_{0i}$$
(4.18)

The SWIM is solved in curvilinear coordinates on the surface of the geometry and is implemented in NSCODE-ICE, a two-dimensional solver. Therefore, Eq. (4.18) is essentially solved on a one-dimensional domain (1D) with s the curvilinear distance, $S_m = 1$ a unit face area and Δs the length of a control volume. $N_{faces} = 2$ since there are only a left and right neighbors to cell i. The left and right faces are denoted respectively by $i - \frac{1}{2}$ and $i + \frac{1}{2}$.

$$\frac{d\mathbf{W}^*_i}{dt} + \frac{\mathbf{F}_{i+\frac{1}{2}} - \mathbf{F}_{i-\frac{1}{2}}}{\Delta s_i} = \mathbf{S}_{0,i}$$
(4.19)

Hence, using a forward Euler method for the temporal discretization, the system becomes:

$$\frac{\mathbf{W}_i^{n+1} - \mathbf{W}_i^n}{\Delta t} - \frac{\mathbf{S}_{ice,i}^{n+1} - \mathbf{S}_{ice,i}^n}{\Delta t} + \frac{\mathbf{F}_{i+\frac{1}{2}}^n - \mathbf{F}_{i-\frac{1}{2}}^n}{\Delta s_i} = \mathbf{S}_{0\,i}^n \tag{4.20}$$

$$\mathbf{W}_i^{n+1} - \mathbf{S}_{ice,i}^{n+1} = \mathbf{W}_i^n - \mathbf{S}_{ice,i}^n + \Delta t \frac{\mathbf{F}_{i-\frac{1}{2}}^n - \mathbf{F}_{i+\frac{1}{2}}^n}{\Delta s_i} + \Delta t \mathbf{S}_{0,i}^n \tag{4.21}$$

However, a purely explicit method has been found to be unstable to solve the equations of the SWIM since the source term is stiff. The source term ($\mathbf{S}_0$) is then solved implicitly to stabilize the system (Blazek, 2005), leading to:

$$\mathbf{W}_i^{n+1} - \mathbf{S}_{ice,i}^{n+1} = \mathbf{W}_i^n - \mathbf{S}_{ice,i}^n + \Delta t \frac{\mathbf{F}_{i-\frac{1}{2}}^n - \mathbf{F}_{i+\frac{1}{2}}^n}{\Delta s_i} + \Delta t \mathbf{S}_{0,i}^{n+1} \tag{4.22}$$

The fluxes are evaluated using a first-order Roe scheme presented in §4.1.6.

4.1.1   Solution Method

The SWIM is composed of two equations (Eq. (4.2) and Eq. (4.3)), three unknowns (h_w, h_{ice} and $\bar{T}$) and four compatibility relations to close the system (Eq. (4.6)). The method used to solve the SWIM is inspired from the Messinger model. A typical method to solve Messinger-like thermodynamic models is to use a changing boundary condition via a trial and error method to assume the state of the water on the surface (dry surface, glaze ice, rime ice or wet surface). It reduces the problem to two unknowns since one out of the three variables is specified depending on the water state. Assuming a glaze ice state first and ignoring the dry case, the process for a cell is outlined as follows:

1. A glaze ice state is assumed (water and ice layers)

   (a) set $T_{surf} = T_{ref}$

   (b) evaluate the heat and mass balance

   (c) verify the compatibility relations

2. if the compatibility relations are not verified, assume a rime ice state (ice only)

   (a) set $h_w^{n+1} = 0$

   (b) evaluate the heat and mass balance

   (c) verify the compatibility relations

3. if the compatibility relations are not verified, assume a liquid state (water only)

(a) set $h_i^{n+1} = 0$

(b) evaluate the heat and mass balance

(c) verify the compatibility relations

4. if the compatibility relations are not verified, return an error, else go to the next cell.

The solving process for the SWIM is also illustrated in Figure 4.1. The first state to be tested is chosen based on the surface temperature computed at the last time step (T_{surf}^n). If the temperature is below the temperature of fusion (T_{ref}), the ice is first assumed to be in rime ice state. If it is above T_{ref}, the surface is first assumed to be in liquid state. Otherwise, the glaze ice case is tested. This first test is intended to reduce the number of operations to solve the SWIM. It relies on the observation that a cell is most likely to remain at the same state than its previous time step, therefore solving the correct ice state the first time.

Each time a state is assumed, the heat and mass balances are evaluated and the compatibility relations are verified. If the compatibility is not verified, the next state is tested. For each cell and each time-step, the process is repeated until either all the compatibility relations are verified or all the state have been tested. In the event that the compatibility relations are not verified for all states (dry, rime, glaze and wet), it is most likely that the airflow or the droplets are not converged properly, inducing a difficult/non-physical system to solve.
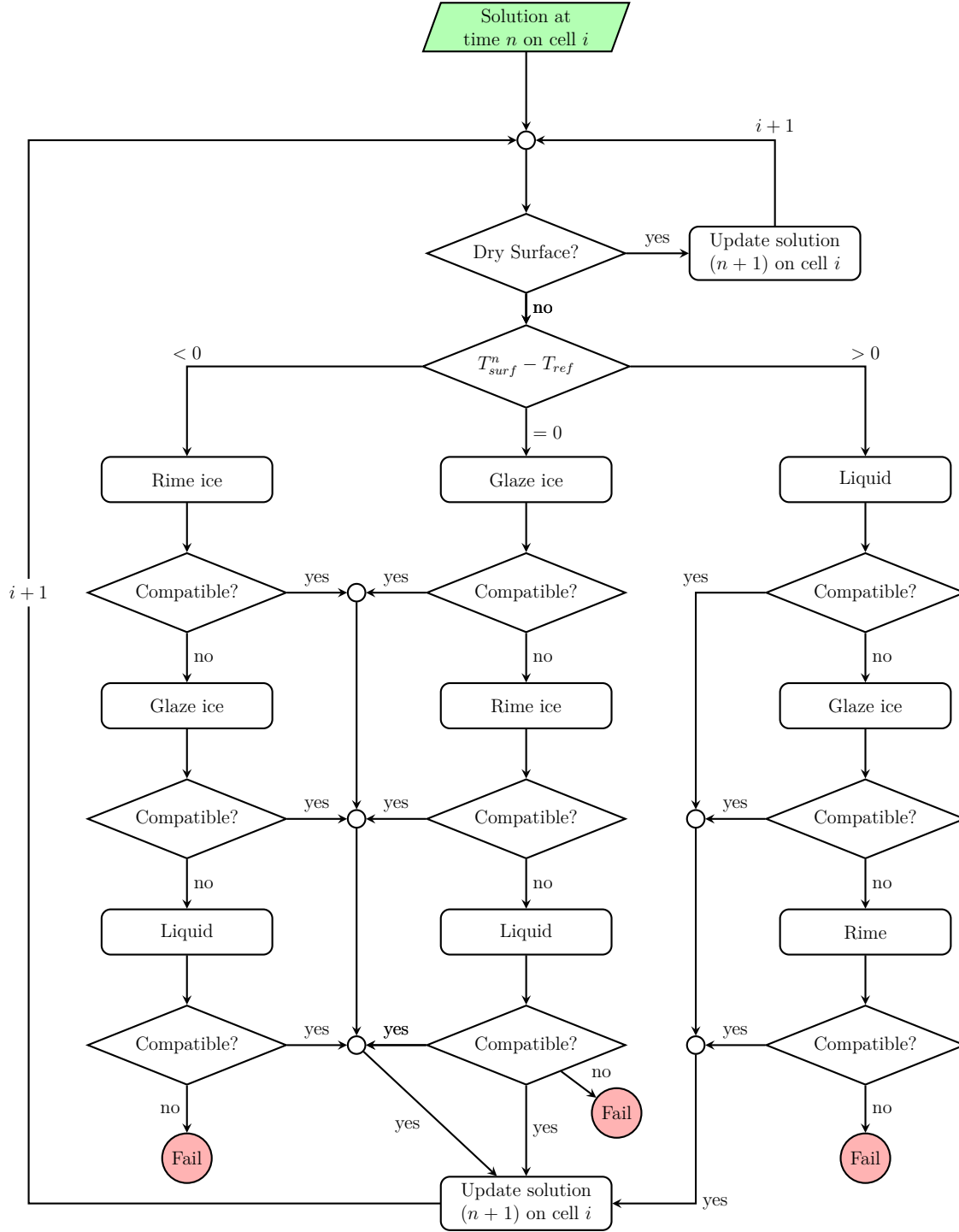
Figure 4.1 Solving process for the SWIM for a single cell i over one time step

4.1.2 Dry or Clean Surface

This case is encountered when there is no impinging water, no water flow and no initial ice nor water.

$$\dot{m}_{imp} = \dot{m}_{in} = 0 \tag{4.23}$$

$$h_{ice}^n = h_w^n = 0 \tag{4.24}$$

$$\mathbf{F}_{i-\frac{1}{2}}^n = \mathbf{F}_{i+\frac{1}{2}}^n = 0 \tag{4.25}$$

Hence,

$$\mathbf{W}^n = \mathbf{S}_{ice}^n = 0 \tag{4.26}$$

$$\dot{m}_{ev} = \dot{m}_{su} = 0 \tag{4.27}$$

$$\dot{Q}_{ev} = \dot{Q}_{su} = \dot{Q}_{drop} = 0 \tag{4.28}$$

The system simplifies to:

$$\mathbf{W}^{n+1} - \mathbf{S}_{ice}^{n+1} = \Delta t \mathbf{S}_0^{n+1} \tag{4.29}$$

For the mass balance:

$$\rho_w h_w^{n+1} + \rho_{ice} h_{ice}^{n+1} = 0 \tag{4.30}$$

Since $h_{ice} \geq 0$ and $h_w \geq 0$, the mass balance gives $h_{ice}^{n+1} = h_w^{n+1} = 0$. Then, the energy balance is:

$$(\rho_w h_w C_{p,w} \bar{T} - \rho_{ice} h_{ice}(L_{fus} - C_{p,ice}\bar{T}))^{n+1} = \frac{\Delta t}{\Delta s}(\dot{Q}_f - \dot{Q}_{rad} - \dot{Q}_{conv})^{n+1}$$

$$0 = (\dot{Q}_f - \dot{Q}_{rad} - \dot{Q}_{conv})^{n+1}$$

Rearranging the equation in the form $f(x) = 0$, the surface temperature (T_{surf}) can be solved iteratively using Newton-Raphson method (Eq. (4.31)).

$$T_{surf}^{(k+1)} = T_{surf}^{(k)} - \frac{f(T_{surf}^{(k)})}{f'(T_{surf}^{(k)})} \tag{4.31}$$

with

$$f_{dry}(T_{surf}) = \sigma_r \varepsilon(T_{surf}^4 - T_\infty^4) - HTC(T_{surf} - T_{rec}) = 0 \tag{4.32}$$

$$f'_{dry}(T_{surf}) = 4\sigma_r \varepsilon T_{surf}^3 - HTC. \tag{4.33}$$

4.1.3 Glaze Ice

In glaze ice conditions, the surface temperature is at the temperature of fusion of water $(T_{surf}^{n+1} = T_{ref}$ or $\bar{T}^{n+1} = T_{surf}^{n+1} - T_{ref} = 0)$. From the energy equation, h_{ice}^{n+1} is computed.

$$-\rho_w C_{p,w}(h_w \bar{T})^n - \rho_{ice}\left(h_{ice}^{n+1}L_{fus} - h_{ice}^n(L_{fus} - C_{p,ice}\bar{T})^n\right) = \frac{\Delta t}{\Delta s}\left(F_{i-\frac{1}{2}}^n - F_{i+\frac{1}{2}}^n + S_0^{n+1}\right)_{energy}$$

$$h_{ice}^{n+1} = \frac{\rho_w C_{p,w}(h_w \bar{T})^n - \rho_{ice}h_{ice}^n(L_{fus} - C_{p,ice}\bar{T})^n + \frac{\Delta t}{\Delta s}\left(F_{i-\frac{1}{2}}^n - F_{i+\frac{1}{2}}^n + S_0^{n+1}\right)_{energy}}{-\rho_{ice}L_{fus}} \quad (4.34)$$

Then, h_w^{n+1} is found from the mass balance.

$$\rho_w(h_w^{n+1} - h_w^n) + \rho_{ice}(h_{ice}^{n+1} - h_{ice}^n) = \frac{\Delta t}{\Delta s}\left(F_{i-\frac{1}{2}}^n - F_{i+\frac{1}{2}}^n + S_0^{n+1}\right)_{mass}$$

$$h_w^{n+1} = \frac{\rho_w h_w^n - \rho_{ice}(h_{ice}^{n+1} - h_{ice}^n) + \frac{\Delta t}{\Delta s}\left(F_{i-\frac{1}{2}}^n - F_{i+\frac{1}{2}}^n + S_0^{n+1}\right)_{mass}}{\rho_w} \quad (4.35)$$

Since the surface temperature is known the source term $\mathbf{S_0^{n+1}}$ is also known. Hence the system is directly solved by Eq. (4.34) and Eq. (4.35).

4.1.4 Rime Ice

For a rime ice case, the droplets freeze entirely upon impact with the surface. Therefore, there is no water film $(h_w^{n+1} = 0)$. First, the ice thickness h_{ice}^{n+1} is isolated from the mass balance.

$$\rho_{ice}(h_{ice}^{n+1} - h_{ice}^n) - \rho_w h_w^n = \frac{\Delta t}{\Delta s}\left(F_{i-\frac{1}{2}}^n - F_{i+\frac{1}{2}}^n + S_0^{n+1}\right)_{mass} \quad (4.36)$$

$$h_{ice}^{n+1} = \frac{\rho_w h_w^n + \rho_{ice}h_{ice}^n + \frac{\Delta t}{\Delta s}\left(F_{i-\frac{1}{2}}^n - F_{i+\frac{1}{2}}^n + S_0^{n+1}\right)_{mass}}{\rho_{ice}} \quad (4.37)$$

In order to compute h_{ice}^{n+1}, the value of T_{surf}^{n+1} is needed as it is present in the source term $S_{0,mass}^{n+1}$. The surface temperature also appears in the energy balance:

$$-\rho_w C_{p,w}(h_w \bar{T})^n - \rho_{ice}\left(h_{ice}^{n+1}(L_{fus} - C_{p,ice}\bar{T})^{n+1} - h_{ice}^n(L_{fus} - C_{p,ice}\bar{T})^n\right) =$$
$$\frac{\Delta t}{\Delta s}\left(F_{i-\frac{1}{2}}^n - F_{i+\frac{1}{2}}^n + S_0^{n+1}\right)_{energy}. \quad (4.38)$$

Note the source terms $S^{n+1}_{0,mass}$ and $S^{n+1}_{0,energy}$ are non-linear and function of the surface temperature (the evaporation, sublimation and radiation terms are non-linear). Hence, the system is solved using an iterative method. Eq. (4.37) is replaced in the energy balance Eq. (4.38), then the equation is written in the form $f(T_{surf}) = 0$ and the system is solved using an iterative method.

$$f_{rime}(T^{n+1}_{surf}) = \rho_w C_{p,w}(h_w \bar{T})^n + \rho_{ice}\left(h^{n+1}_{ice}(L_{fus} - C_{p,ice}\bar{T})^{n+1} - h^n_{ice}(L_{fus} - C_{p,ice}\bar{T})^n\right) + $$
$$\frac{\Delta t}{\Delta s}\left(F^n_{i-\frac{1}{2}} - F^n_{i+\frac{1}{2}} + S^{n+1}_0\right)_{energy} = 0$$

(4.39)

Equation (4.39) could be solved using the Newton-Raphson method. However, when an expression cannot easily be derived for f' (Eq. (4.31)), it is preferable to use Brent method (Press et al., 1992) as it is more computationally efficient. Also, it makes for a more general implementation, since there is no need to re-derive an expression for f' if the terms are changed in the mass and energy balances.

A limiter for the sublimation

The solution changes abruptly at the glaze/rime interface and it sometimes induces difficulties in solving the surface temperature. For instance, one may observe a large amount of sublimation that leads to a negative ice accretion rate. In reality, the sublimation process stops when no ice is left. To avoid this issue and increase robustness, a limiter is used on the mass of sublimation. The worst case scenario occurs when there is no ice accretion ($\dot{m}_{ice} = 0$ or $h^{n+1}_{ice} = h^n_{ice}$). Hence, the maximum amount of mass that can sublimate is found from the mass balance (Eq. (4.36)), which gives:

$$\rho_{ice}h^{n+1}_{ice} = \rho_w h^n_w + \rho_{ice}h^n_{ice} + \frac{\Delta t}{\Delta s}\left(F^n_{i-\frac{1}{2}} - F^n_{i+\frac{1}{2}} + \dot{m}^{n+1}_{imp} - \dot{m}^{n+1}_{su}\right)$$
$$\dot{m}^{max}_{su} = \frac{\Delta s}{\Delta t}\rho_w h^n_w + F^n_{i-\frac{1}{2}} - F^n_{i+\frac{1}{2}} + \dot{m}^{n+1}_{imp}$$

(4.40)

Then, one must simply ensure that $0 \leq \dot{m}^{n+1}_{su} \leq \dot{m}^{max}_{su}$. One method is to compute $\dot{m}^{n+1}_{su}$ from the usual relation and $\dot{m}^{max}_{su}$ from Eq. (4.40). Then, apply the following constraints to the mass balance:

$$h^{n+1}_{ice} = \begin{cases} Eq.\ (4.37) & if \quad \dot{m}^{n+1}_{su} \leq \dot{m}^{max}_{su} \\ h^n_{ice} & otherwise \end{cases}$$

(4.41)

$$\dot{m}^{n+1*}_{su} = min(\dot{m}^{n+1}_{su}, \dot{m}^{max}_{su})$$

(4.42)

where $\dot{m}_{su}^{n+1*}$ denotes the corrected mass rate of sublimation that can be used in the mass and energy balances.

4.1.5 Wet Surface

In wet regime the surface is covered with a water film, but there is no ice ($h_{ice}^{n+1} = 0$). In such a situation, the water film thickness h_w^{n+1} is first computed from the mass balance.

$$\rho_w(h_w^{n+1} - h_w^n) - \rho_{ice}h_{ice}^n = \frac{\Delta t}{\Delta s}\left(F_{i-\frac{1}{2}}^n - F_{i+\frac{1}{2}}^n + S_0^{n+1}\right)_{mass} \tag{4.43}$$

$$h_w^{n+1} = \frac{\rho_w h_w^n + \rho_{ice}h_{ice}^n + \frac{\Delta t}{\Delta s}\left(F_{i-\frac{1}{2}}^n - F_{i+\frac{1}{2}}^n + S_0^{n+1}\right)_{mass}}{\rho_w} \tag{4.44}$$

Second, the surface temperature is computed from the energy balance (Eq. (4.45)) using h_w^{n+1} from Eq. (4.44). Again the source term is non-linear due to the presence of T_{surf} in evaporation, sublimation and radiation related terms. Following the same process as for rime ice condition, the equation is written in the form $f(x) = 0$ so the temperature can be solved iteratively using Brent method.

$$\begin{aligned} f(T_{surf}^{n+1}) = \rho_w C_{p,w}\left((h_w\bar{T})^{n+1} - (h_w\bar{T})^n\right) + \rho_{ice}h_{ice}^n(L_{fus} - C_{p,ice}\bar{T})^n \\ + \frac{\Delta t}{\Delta s}\left(F_{i-\frac{1}{2}}^n - F_{i+\frac{1}{2}}^n + S_0^{n+1}\right)_{energy} = 0 \end{aligned} \tag{4.45}$$

A limiter for the evaporation

In some cases, the evaluation of the surface temperature may lead to an evaporation mass larger than the actual water mass available. A negative water film thickness is then obtained. To avoid this situation, a limiter is used on the mass of evaporation. The worst case scenario occurs when all the water evaporates hence $h_w^{n+1} = 0$. From this condition, the maximum mass of evaporation is computed from the mass balance.

$$\rho_w h_w^{n+1} = \rho_w h_w^n + \rho_{ice}h_{ice}^n + \frac{\Delta t}{\Delta s}\left(F_{i-\frac{1}{2}}^n - F_{i+\frac{1}{2}}^n + \dot{m}_{imp}^{n+1} - \dot{m}_{ev}^{n+1}\right) \tag{4.46}$$

$$\dot{m}_{ev}^{max} = \frac{\Delta s}{\Delta t}\left(\rho_w h_w^n + \rho_{ice}h_{ice}^n\right) + F_{i-\frac{1}{2}}^n - F_{i+\frac{1}{2}}^n + \dot{m}_{imp}^{n+1} \tag{4.47}$$

Again, one must simply ensure that $0 \leq \dot{m}_{ev}^{n+1} \leq \dot{m}_{ev}^{max}$. For instance, by applying the following procedure.

$$h_w^{n+1} = \begin{cases} Eq. \ (4.35) & if \quad \dot{m}_{ev}^{n+1} \leq \dot{m}_{ev}^{max} \\ h_w^n & otherwise \end{cases} \tag{4.48}$$

$$\dot{m}_{ev}^{n+1*} = min(\dot{m}_{ev}^{n+1}, \dot{m}_{ev}^{max}) \tag{4.49}$$

4.1.6 First-Order Roe Scheme for the Convective Fluxes

The water film flowing over the airfoil surface can be seen as an advancing front with a shock at the location of the wet/dry interface. The numerical scheme of Roe is known for its crisp representation of shocks which make it suitable for the SWIM. A Roe scheme was also used by Beaugendre (2003) and Myers et al. (2002) for similar applications. The implementation of the numerical scheme is presented below.

Taking the definition from Blazek (2005), Chapter 4, the first-order Roe scheme is developed for the fluxes $(\mathbf{F}_{i+\frac{1}{2}})$ of the SWIM:

$$\mathbf{F}_{i+\frac{1}{2}} = \frac{1}{2}(\mathbf{F}_R + \mathbf{F}_L) - \frac{1}{2}|\mathbf{A}(\mathbf{W})|_{i+\frac{1}{2}}(\mathbf{W}_R - \mathbf{W}_L) \tag{4.50}$$

where the Jacobian matrix $(\mathbf{A}(\mathbf{W}))$ is evaluated at the Roe average, taken as the average of the left and right states:

$$\tilde{(\cdot)} = \frac{(\cdot)_R + (\cdot)_L}{2} \tag{4.51}$$

First, Eq. (4.8) and Eq. (4.9) are rearranged and $\bar{u}$ is expended:

$$\mathbf{W} = \begin{pmatrix} h_w \\ h_w C_{p,w} \bar{T} \end{pmatrix}, \quad \mathbf{F} = \begin{pmatrix} \frac{h_w^2}{2\mu_w}\tau_{wall} \\ \frac{h_w^2}{2\mu_w}\tau_{wall} C_{p,w} \bar{T} \end{pmatrix} \tag{4.52}$$

$$\mathbf{S} = \frac{1}{\rho_w} \begin{pmatrix} \dot{m}_{imp} - \dot{m}_{ice} - \dot{m}_{es} \\ \dot{Q}_{drop} + \dot{Q}_{ice} - \dot{Q}_{ev} + \dot{Q}_{rad} + \dot{Q}_{conv} \end{pmatrix} = \begin{pmatrix} S_1 \\ S_2 \end{pmatrix} \tag{4.53}$$

The system can be written as (in 1D curvilinear coordinates):

$$\frac{\partial \mathbf{W}}{\partial t} + \mathbf{A}(\mathbf{W})\frac{\partial \mathbf{W}}{\partial s} = \mathbf{S} \tag{4.54}$$

where $\mathbf{A}(\mathbf{W})$ is the Jacobian matrix of the system and, for a 1D case, it is equal to:

$$\frac{\partial \mathbf{F}}{\partial \mathbf{W}} = \mathbf{A}(\mathbf{W}) = \frac{1}{2\mu_w} \begin{bmatrix} 2h_w\tau_{wall} & 0 \\ h_wC_{p,w}\bar{T}\tau_{wall} & h_w\tau_{wall} \end{bmatrix} \tag{4.55}$$

Hence, the eigenvalues of $\mathbf{A}$ are:

$$\lambda_1 = \frac{h_w\tau_{wall}}{\mu_w} = 2\bar{u} \quad and \quad \lambda_2 = \frac{h_w\tau_{wall}}{2\mu_w} = \bar{u} \tag{4.56}$$

4.1.7 Time-stepping

The eigenvalues (Eq. (4.56)) are used to compute the maximum allowable time-step for the simulation to be stable via the Courant-Friedrichs-Lewy (CFL) condition. The local time-step for a cell j is computed from:

$$\Delta t_j = \left(CFL \frac{\Delta s}{max(\lambda_1, \lambda_2)} \right)_j \tag{4.57}$$

Since a global time-stepping method is used, the overall time-step (Δt) is taken as the minimum of all the Δt_j. The CFL is typically set to 0.9.

$$\Delta t = min(\Delta t_j) \tag{4.58}$$

Note that the eigenvalues are both zeros when there is no water ($h_w = 0$), leading to an undefined time-step size. This situation is encountered when computing the initial time-step and, when the surface is either in rime ice or in dry condition. To solve this issue, a thin water film height is set to evaluate the required parameters, referred to as the precursor film (h_p). A priori, the precursor film thickness is unknown. Following the observation of many simulations, the water film thickness tends to be of the order $10^{-6}\,m$ and the same order of magnitude is also used by Myers et al. (2002) for the precursor film thickness. Thus, the eigenvalues are evaluated with h_p to provide the time-step size following Eq. (4.57). The precursor film is used only if the surface is completely dry. If a water film is present anywhere on the surface, the time-step is computed the usual way, using h_w^n.

4.1.8 Convergence

The SWIM is implemented in an unsteady manner using a first-order forward Euler temporal discretization and a first-order spatial discretization. The solution evolves in time where all the parameters are evaluated accordingly, but without updating the airflow and droplets

solution. The time-step size is determined by the eigenvalues of the system via the CFL conditions §4.1.7. The solution is integrated in time until the total ice accretion time is achieved. For instance, the case 31 represent a $480s$ ice accretion process and the time-step size is of the order of $1 \times 10^{-3}s$. This gives at best $480\,000$ iterations to solve the unsteady problem since the time-step size as a tendency to reduce as the water height increases. It is important to note that for some simulation the time-step size can be significantly lower (e.g. $1 \times 10^{-6}s$), hence leading to large simulation times.

To avoid this issue, it is interesting to notice that the simulation can behave in three different ways. First, the ice accretion process could stabilize to a state where the ice thickness, water film thickness and surface temperature are constant. This situation is unlikely to occur for in-flight icing unless an anti-icing system is preventing any ice to accumulate. Second, the ice accretion could reach a steady growth rate where the ice and water thicknesses are not constant but accumulating at a steady rate. Third, the simulation is unsteady and the parameters change over time for the entire simulation time. The current implementation can simulate all three scenarios.

The second option, when a steady accumulation rate is reached is often observed during numerical icing simulation with the SWIM. This is mainly due to the quasi-steady method employed in the icing software where the airflow and droplets fields are at steady states. Therefore the parameters such as the water impingement rate ($\dot{m}_{imp}$), the skin friction, the HTC, etc. are constant over the simulation time as seen by the SWIM. There is a short transient process over which the water film thickness pass from null to a fairly constant value as shown on Figure 4.2. This is the time required for the runback water to stabilize, then the water accumulation and ice accretion rates are very close to a steady state.
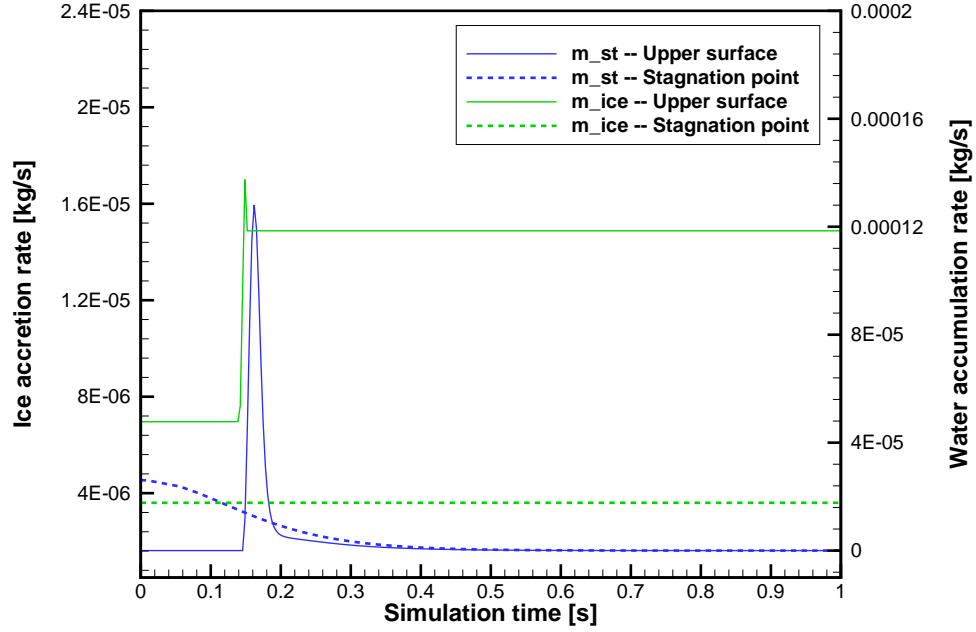
Figure 4.2 Time evolution of the SWIM for the glaze ice case 31 – water accumulation and ice accretion rates

Following this observation, a stopping criterion is added to the SWIM. When the mass and temperature residuals reach 1×10^{-12} the simulation is deemed to be in a steady accretion/accumulation rate. Hence, the solution is integrated in time until $\log_{10}(err) \leq -12$, if it is ever the case. Then, the simulation is stopped and the parameters (h_w, h_{ice}, T_{surf}) are extrapolated to the total icing time. For h_{ice} on a control volume j, it gives:

$$h_{ice,j} = h_{ice,j}^{n+1} + \dot{m}_{ice,j}^{n+1}(t_{ice} - t_{stop}) \tag{4.59}$$

where t_{ice} and t_{stop} denote respectively the total ice accretion time and the simulation time when the steady state was reached. If the steady rate state is not achieved, the simulation continues until the total ice accretion time or the user defined number of iteration is achieved.

The mass and temperature residuals are defined respectively as:

$$RMS_{mass} = \sqrt{\frac{1}{N_{cell}} \sum_{j}^{N_{cell}} (\dot{m}_{ice,j}^{n+1} - \dot{m}_{ice,j}^{n})^2 ds_j^2} \tag{4.60}$$

$$RMS_{Temp} = \sqrt{\frac{1}{N_{cell}} \sum_{j}^{N_{cell}} (T_{surf,j}^{n+1} - T_{surf,j}^{n})^2} \tag{4.61}$$

where

$$\dot{m}_{ice}^{n+1}ds = \frac{\rho_{ice}ds(h_{ice}^{n+1} - h_{ice}^n)}{\Delta t} \tag{4.62}$$

The residuals are then scaled against the initial value evaluated at the first iteration (RMS_0) to evaluate $\log_{10}(err)$ with Eq. (4.65).

$$\log_{10}(err)_{mass} = \log_{10}(RMS_{mass}) - \log_{10}(RMS_{mass,0}) \tag{4.63}$$

$$\log_{10}(err)_{energy} = \log_{10}(RMS_{energy}) - \log_{10}(RMS_{energy,0}) \tag{4.64}$$

$$\log_{10}(err) = \max(\log_{10}(err)_{mass}, \log_{10}(err)_{energy}) \tag{4.65}$$
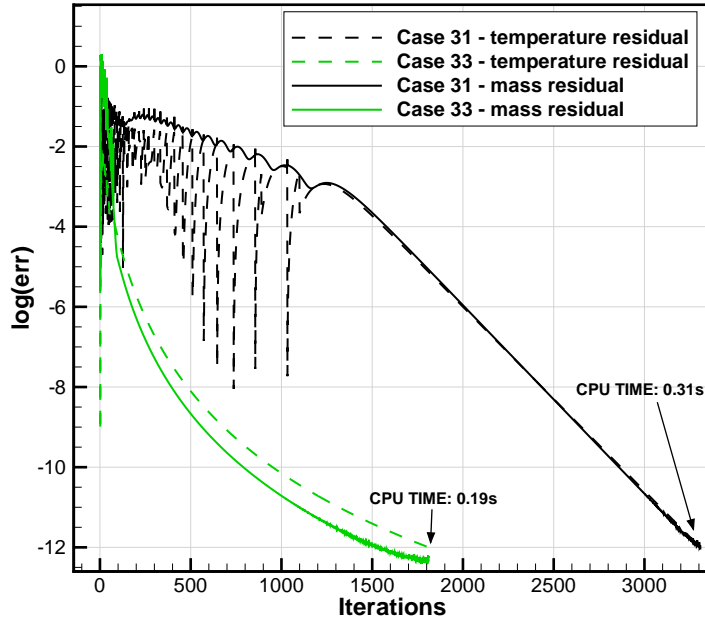
Figure 4.3 Convergence for the glaze ice case 31 and the rime ice case 33

Figure 4.3 illustrates the convergence for the case 31 and 33. Both test cases reached the steady state, leading to a significantly faster simulation time. For case 31 the CPU time with the extrapolation is $0.31s$ compared to $10.47s$ without. As for the case 33, the CPU time is $0.19s$ with the extrapolation while it is $0.81s$ for the full simulation.

4.2 Verification of the Thermodynamic Model

A verification of the swim is required to make sure it is implemented properly. This section first presents a grid convergence study in order to assess the accuracy of the discretization.

Second, the behavior of the model is verified over an airfoil in liquid conditions. Third, it is verified that the model compares well with the Iterative Messinger model previously implemented in NSCODE-ICE as they model similar physics. The results are also compared to other icing softwares. Finally, a manufactured test case is presented to highlight issues with the current implementation.

All the test cases are run with the HTC model described in §3.1. For this chapter, a mono-dispersed droplets distribution is used except for the results of cases 27 and 31 which are run with the Langmuir D distribution (§3.3.1). A summary of the test parameters for each run is given in Table A.1.

4.2.1 Grid Convergence

To verify the accuracy of the discretization, a set of five structured grids is used. The finest grid is composed of 1024 cells in the tangential (i) and normal (j) directions. This mesh is then coarsened to obtain grids with respectively 512, 256, 128 and 64 cells in both directions. The Root Mean Square (RMS) of the distance between the current ice shape compared to the finest one is evaluated. Since the number of cells is not the same for each grid, the ice shapes are linearly interpolated to obtain a distribution of 1024 cells. Furthermore, as the clean geometry will also affect the result, only the iced surface of the airfoil is considered for the evaluation of the RMS.

Figure 4.4a illustrates the ice shape for the different grids used. The ice thickness is fairly constant from the grid composed of 257x257 nodes to the 1025x1025 grid. Also, as the grid is refined a sharper representation of the ice limits is achieved, inducing only a small change of the overall iced geometry. Figure 4.4b shows the error ($\log(RMS)$) against $\log(1/N)$ where N represent the number of cells. The order of accuracy is given by the slope and is somewhere between 1 and 2. Since the result depend on the entire icing software, it is concluded that the SWIM is at least 1st order accurate which verifies the consistency of the model.
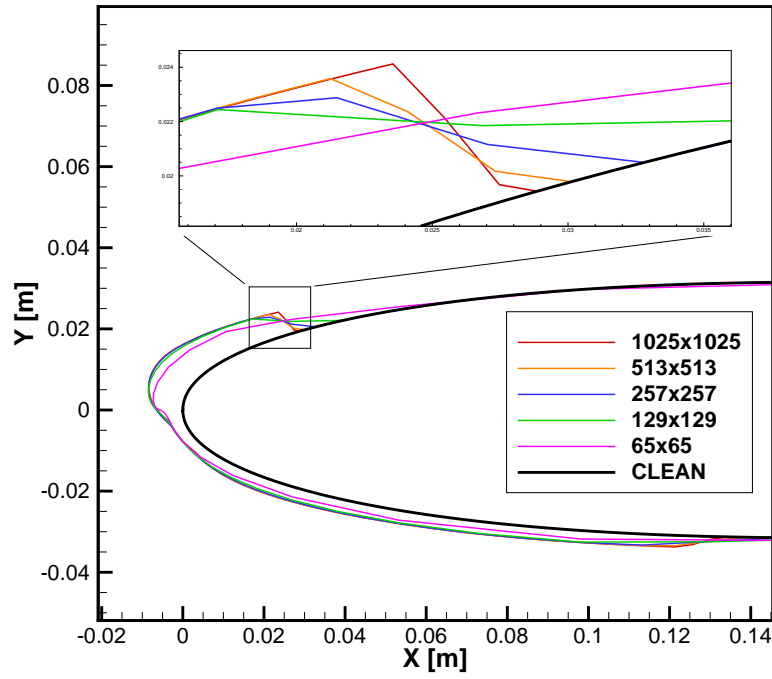
(a) Ice shape
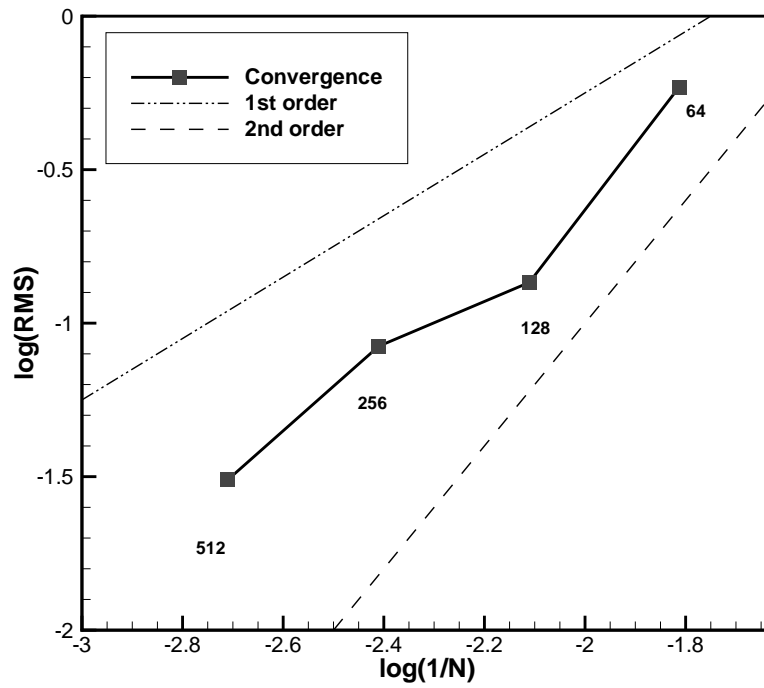
(b) Order of convergence

Figure 4.4 Grid convergence for NSCODE-ICE using the SWIM

4.2.2 Verification of the Water Film (Case W)

To verify that the model behaves correctly, a simulation is performed on a NACA0012 airfoil at 0 degrees of angle of attack in liquid condition using a temperature of $15°C$. The test parameters are presented in Table A.1 as cases W.

On Figure 4.5, the water film thickness, water film velocity, surface temperature and ice thickness are observed at ice accretion times: $0.5s$, $1.0s$, $1.5s$ and $2.0s$. As expected since the ambient temperature is above the freezing temperature, no ice is generated for the simulation time presented here. Moreover, note from Figure 4.5a that the collection efficiency is concentrated within the first 5% each side of the stagnation point, hence any water outside of this area is runback water.

Figure 4.5a illustrates that the water film flows away from the stagnation point as the simulation time increases and would eventually reach the trailing edge. This is expected since the only mechanism available to remove water from the surface is evaporation, which is small in comparison to the water impingement rate. Hence the water accumulates and when the film reaches a specific height it starts to flow following the direction of the skin friction. The film velocity (Figure 4.5c) also behaves as expected, since it follows the direction of the local streamlines. The water film must flow in opposite directions at the stagnation point, which is represented with a negative film velocity on the lower surface ($s/c < 1$) and a positive velocity on the upper surface ($s/c > 1$).

The surface temperature is shown on Figure 4.5d, where it is colder when there is water on the airfoil. This is again a normal behavior since energy is lost by evaporation where there is water, reducing the surface temperature. On a dry surface, only the radiation and convection are affecting the temperature of the surface, leading to a warmer surface.

Hence, it is concluded that the water film behaves properly in a fully liquid state. There is no negative water height, the film velocity follows the skin friction direction and the water film thickness reaches a steady state before starting to flow away from the stagnation point.

(a) Water height

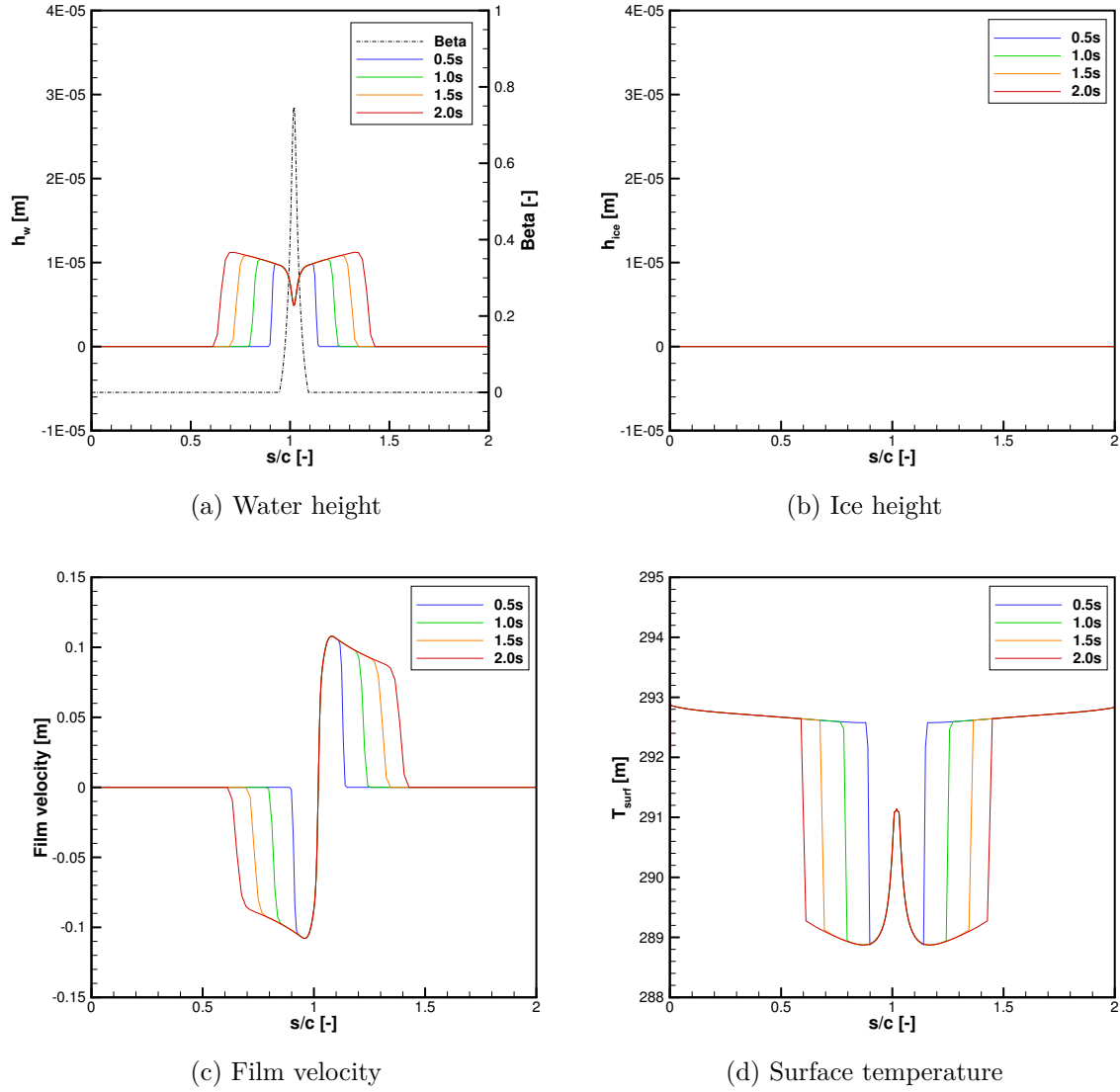(b) Ice height

(c) Film velocity

(d) Surface temperature

Figure 4.5 SWIM in liquid condition

4.2.3 Verification against NSCODE-ICE, LEWICE and ONERA

The Iterative Messinger model as implemented in NSCODE-ICE models the same physics as the SWIM. The main difference being that the former is an algebraic model and the latter

a PDE-based model. For the SWIM, the mass and energy balance are:

$$\rho_w \left[\frac{\partial h_w}{\partial t} + \text{div}(\bar{u} h_w) \right] = \dot{m}_{imp} - \dot{m}_{ice} - \dot{m}_{es} \qquad \text{(4.2 revisited)}$$

$$\rho_w \left[\frac{\partial h_w C_{p,w} \bar{T}}{\partial t} + \text{div}(\bar{u} h_w C_{p,w} \bar{T}) \right] = \dot{Q}_{kin} + \dot{Q}_{ice} - \dot{Q}_{imp} - \dot{Q}_{es} - \dot{Q}_{rad} - \dot{Q}_{conv}$$

$$\text{(4.3 revisited)}$$

and for the Iterative Messinger model, they are:

$$\dot{m}_{st} + \dot{m}_{out} - \sum \dot{m}_{in} = \dot{m}_{imp} - \dot{m}_{ice} - \dot{m}_{es} \qquad (4.66)$$

$$\dot{Q}_{st} - \sum \dot{Q}_{in} = \dot{Q}_{kin} + \dot{Q}_{ice} - \dot{Q}_{imp} - \dot{Q}_{es} - \dot{Q}_{rad} - \dot{Q}_{conv} \qquad (4.67)$$

where $\sum \dot{m}_{in}$ and $\sum \dot{Q}_{in}$ represent the summation of the water inflows in the control volume in terms of mass and energy, allowing inflows from more than one direction. $\dot{m}_{st}$ and $\dot{Q}_{st}$ denote a water accumulation rate (stagnation water) into the cell in terms of mass and energy.

It is noticed that the right hand sides of Eq. (4.2) and Eq. (4.66) are identical. The same pattern is observed for Eq. (4.3) and Eq. (4.67). The term $\rho_w \text{div}(\bar{u} h_w)$ represents the fluxes at the faces of the control volume and is then directly related to $\dot{m}_{out} - \sum \dot{m}_{in}$. Furthermore, $\rho_w \frac{\partial h_w}{\partial t}$ is related to the rate of change of water mass which correspond to $\dot{m}_{st}$. The same observations are made for the energy terms.

Moreover, remember that the Iterative Messinger model is solved for a steady state and the SWIM is solved in an unsteady manner. Besides, the SWIM generally converges to a steady state in a very short time as evidenced by Figure 4.2 and Figure 4.3. Therefore, it is concluded that both model should generate very similar results.

Figure 4.6 illustrates the ice shape prediction for both thermodynamic models on a glaze ice case and a rime ice case. As expected, the ice shapes are similar for the SWIM and the Iterative Messinger model. It confirms the previous discussion and the correctness of the implementation for the SWIM. Moreover, the results compares well to the other icing softwares (Figure 4.7), suggesting that both models are well implemented.
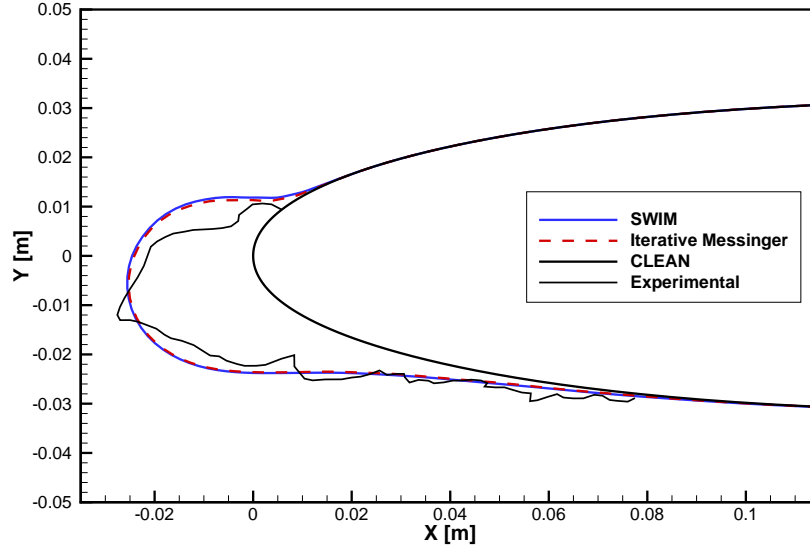
(a) Rime ice case 27
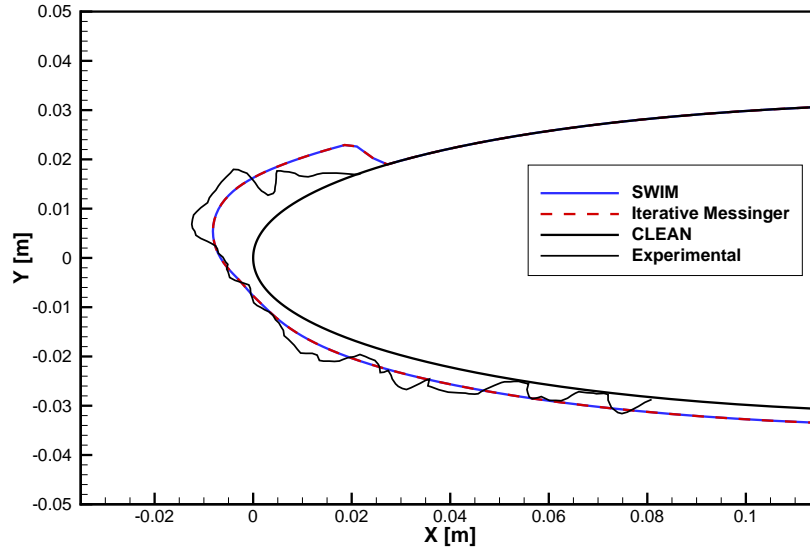
(b) Glaze ice case 31

Figure 4.6 Comparison of the Iterative Messinger model and the SWIM for rime and glaze ice – Single layer ice accretion
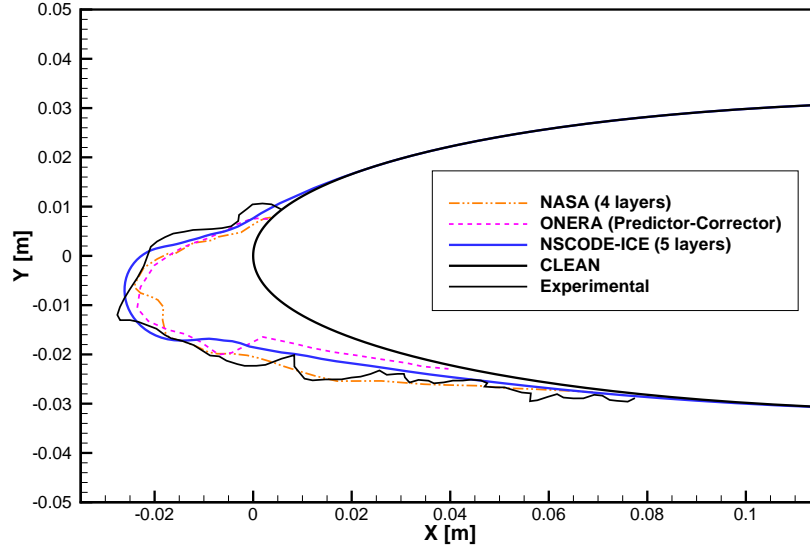
(a) Rime ice case 27
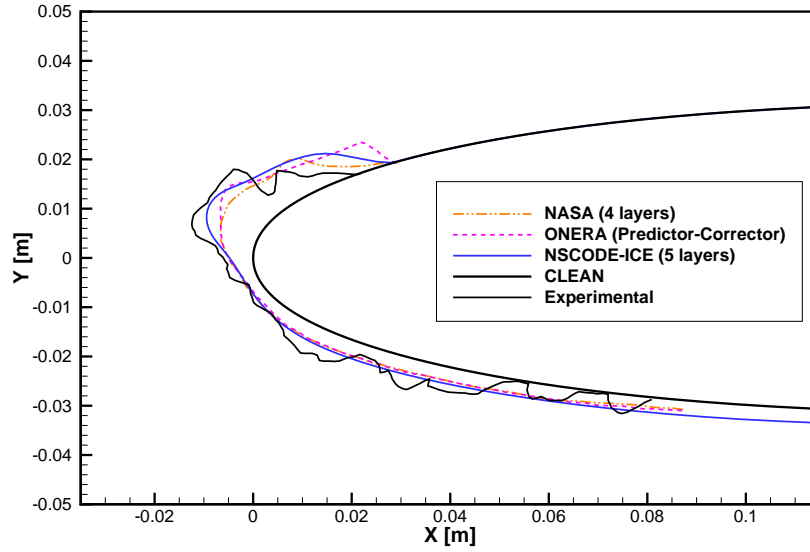
(b) Glaze ice case 31

Figure 4.7 Comparison of the SWIM against NASA and ONERA numerical results (Wright et al., 1997)

4.2.4   Manufactured Ice Shape (Case M)

To this point, the Iterate Messinger model and the SWIM predicts very similar ice shape. It is assumed to be true for regular geometries, however it might be different for more complex cases. A manufactured ice shape is then created to highlight the weaknesses of the thermodynamic models, especially in terms of runback water behavior. The geometry has three ice horns allowing four recirculation zones to form (Figure 4.8a). Also Figure 4.8b

shows that there is no droplet impacting the surface past the upper and lower horns. Any ice accretion past these areas must be due to runback water.
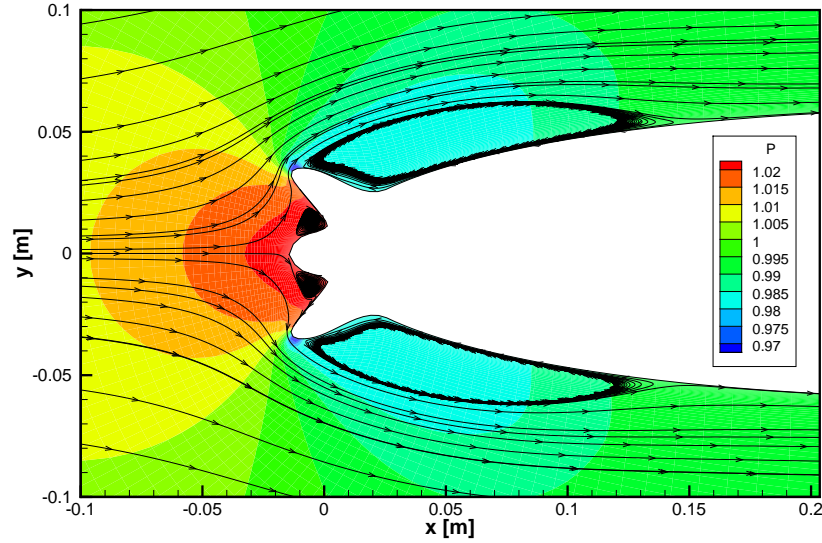
(a) Pressure contours and streamlines
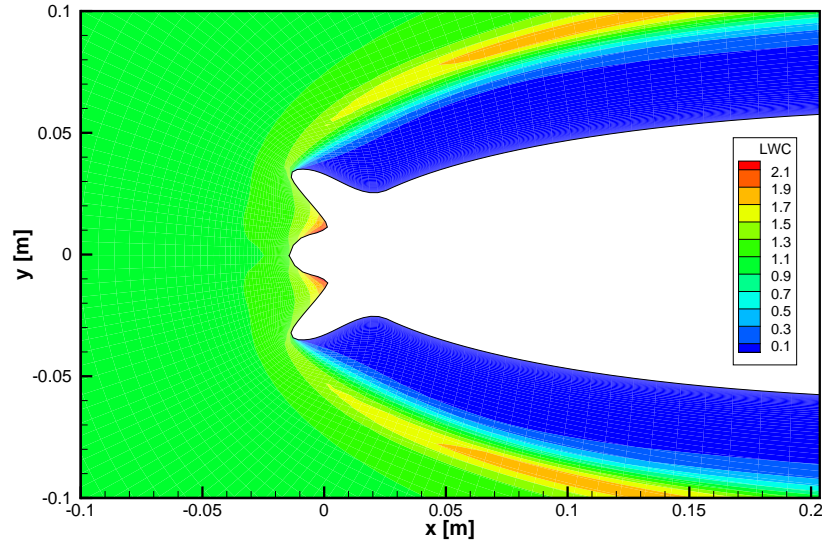
(b) Liquid water content contours

Figure 4.8 Airflow and droplets field on the manufactured geometry

Three thermodynamic models are presented on the manufactured geometry: the Messinger model, the Iterative Messinger model and the SWIM. The Messinger model is available in NSCODE-ICE since it is only a matter of extracting the heat and mass balances from the iterative loop of the Iterative Messinger model. It is added to the comparison to illustrate the difference in runback water modeling when using a stagnation point based model. Figure

4.9 exhibits the ice shape for the three thermodynamic models.

First, by analyzing Figure 4.9, the Messinger models shows ice limits reaching farther towards the trailing edge. For this models the runback water flows towards the trailing edge regardless of the ice horns. However, the SWIM and the Iterative Messinger model capture the effect of the recirculation areas by showing less runback water (reversed shear stress). Taking the upper ice horn as an example, the wall shear stress in this area points towards the tip of the horn, driving the water film in this direction at the same time.

Second, there seems to be a discrepancy with the mass of ice (Figure 4.9) since the Messinger model shows a larger mass of ice. Close the the manufactured horns, the ice thickness is very similar for the three models. However, past the upper and lower horns, the SWIM and the Iterative Messinger model present no ice while the Messinger model exhibits a thin ice layer extending on a long part of the airfoil. The total mass of ice is then clearly and significantly different.
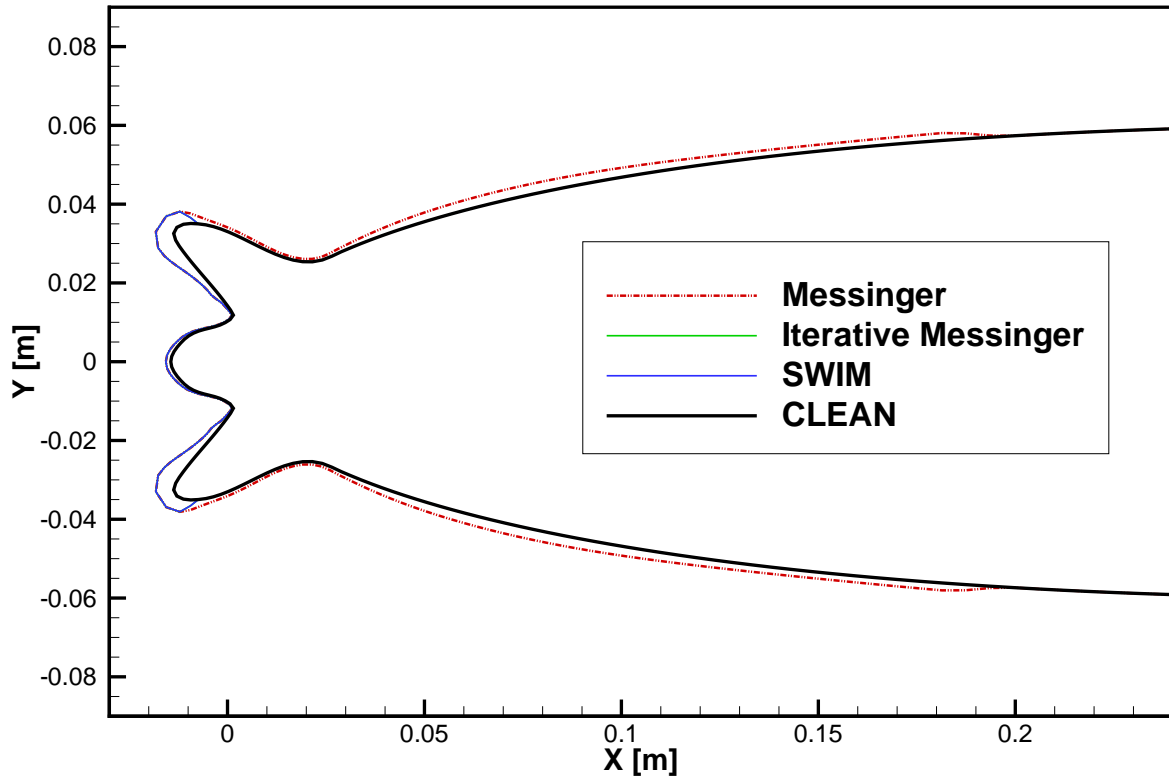
Figure 4.9 Comparison of the ice shapes for the Iterative Messinger model and the SWIM on the manufactured geometry

Figure 4.10 illustrates that the missing ice mass (Iterative Messinger and SWIM) is water accumulated on the surface but not shown on typical icing simulation results. The Messinger model does not allow water accumulation into a cell. Hence for this model, water flows towards the trailing edge until everything is frozen, or until the water reach the trailing edge itself. For the SWIM and the Iterative Messinger model, water accumulation is possible and occurring in 4 zones: on both side of the middle horn, on the lower side of the lower horn and on the upper side of the upper horn. A simple look at Figure 4.10 highlights an issue. The water accumulated is too high comparing to how it should normally behave. A water column like shown cannot build up on an airfoil surface with the current wind velocity, it would simply collapse and spread or shed from the surface. The water runback here is driven by the air shear stress only. The results suggests that more physics might be needed to correctly model the motion for the water film in such a situation.
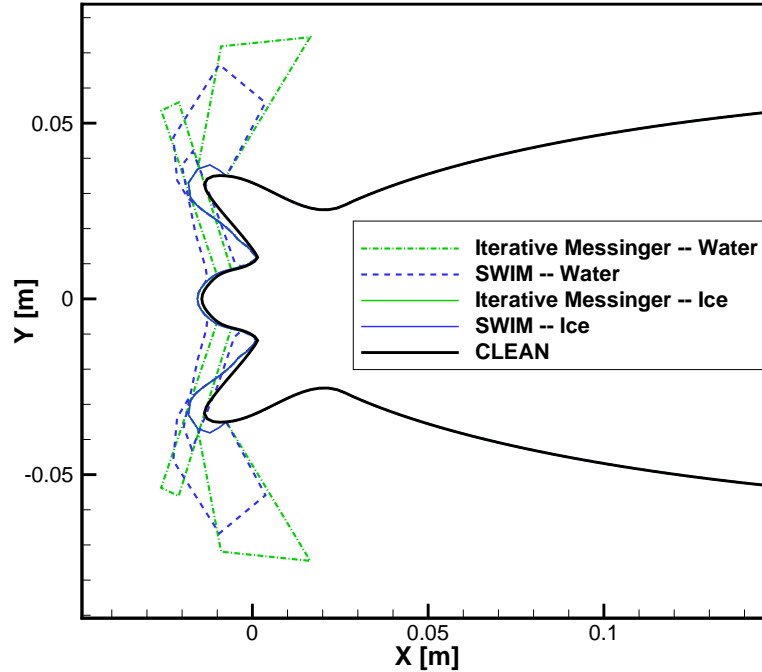
Figure 4.10 Comparison of the water film for the Iterative Messinger model and the SWIM on the manufactured geometry

4.2.5 Pressure Gradients, Gravity and Surface Tension

Further developments are needed to solve the water accumulation issues observed with the Iterative Messinger model and the SWIM (Figure 4.10). A water shedding term could be considered (Wright et al. (2015)), however more fundamental physics is lacking in the current

implementation of the SWIM. Myers et al. (2002) have also developed a thermodynamic model similar to the SWIM but this time considering the effects of pressure, surface tension and gravity for the water film motion. It also models the temperature gradients through the ice and water layer, which require solving the thermodynamic model in an unsteady manner.

The Eq. (4.22) is used to solve the SWIM:

$$\mathbf{W}_i^{n+1} - \mathbf{S}_{ice,i}^{n+1} = \mathbf{W}_i^n - \mathbf{S}_{ice,i}^n + \Delta t \frac{\mathbf{F}_{i-\frac{1}{2}}^n - \mathbf{F}_{i+\frac{1}{2}}^n}{\Delta s_i} + \Delta t \mathbf{S}_{0,i}^{n+1} \qquad (4.22 \text{ revisited})$$

When considering the pressure gradients and the force of gravity for the water film motion, the effect is only present in the film velocity ($\bar{u}$) which in turn affects the flux term ($\mathbf{F}$). According to Myers et al. (2002), the new definition in curvilinear coordinates is:

$$\mathbf{F} = \rho_w \begin{pmatrix} -\frac{h_w^3}{3\mu_w}\left(\frac{\partial P}{\partial s} + g_t\right) + \frac{h_w^2}{2\mu_w}\tau_{wall} \\ \left(-\frac{h_w^3}{3\mu_w}\left(\frac{\partial P}{\partial s} + g_t\right) + \frac{h_w^2}{2\mu_w}\tau_{wall}\right)C_{p,w}\bar{T} \end{pmatrix} = \rho_w \begin{pmatrix} \bar{u}h_w \\ \bar{u}h_w C_{p,w}\bar{T} \end{pmatrix} \qquad (4.68)$$

with the velocity now defined as:

$$\bar{u} = -\frac{h_w^2}{3\mu_w}\left(\frac{\partial P}{\partial s} + g_t\right) + \frac{h_w}{2\mu_w}\tau_{wall} \qquad (4.69)$$

Notice that by setting, $\frac{\partial P}{\partial s}$ and g_t to zero, the original SWIM film velocity is retrieved (Eq. (4.1)). The pressure term ($\frac{\partial P}{\partial s}$) represents the pressure variation within the water film. Accounting for the surface tension, the pressure term is expended to give:

$$\bar{u} = \frac{h_w^2}{3\mu_w}\left(\sigma_w \frac{\partial^3 h_w}{\partial s^3} + g_n \frac{\partial h_w}{\partial s} - g_t\right) + \frac{h_w}{2\mu_w}\tau_{wall} \qquad (4.70)$$

where σ_w is the surface tension. g_t and g_n are respectively the tangential and normal component of the gravitational acceleration.

The new water film velocity (Eq. (4.70)) increases with h_w, $\frac{\partial h_w}{\partial s}$ and $\frac{\partial^3 h_w}{\partial s^3}$ meaning that it could prevent the water accumulation observed for the manufactured geometry (Figure 4.10). This is an interesting solution that should be investigated on the manufactured ice shape.

CHAPTER 5   ICING RESULTS

This chapter assess the capacity of NSCODE-ICE to correctly model the ice accretion on airfoils and infinite swept-wings using the 2.5D approach. First a description of the multi-layer process as used in NSCODE-ICE is presented. Then 2D ice accretion simulations are performed using the multi-layer approach, followed by a discussion. The last section covers ice accretion on swept wings. The SWIM is used for all the icing simulations presented in this chapter.

5.1   Multi-Layer Icing in NSCODE-ICE

The standard method to perform multi-layer icing simulation when using a Messinger-like model is to reset the solution at the next layer (e.g. no water, no ice, surface temperature is reset). However, completely resetting the solution is not valid for the SWIM and the iterative Messinger model.

To begin with, the SWIM models the runback water according to the shear stress direction and the water flow depends on the water thickness on the surface. If the water thickness is set to zero for the next layer, first some mass is lost and second the water film velocity will initially be zero. A better solution in this case is to keep track of the water thickness from one layer to the next. The simulation would then start with the water thickness of the previous layer.

Then, the Iterative Messinger model uses the shear stress to determine the motion of the water film. In some situations, the water can accumulate and remain on the surface. Hence the water film thickness should not be reset for the next ice layer to avoid water mass loss.

NSCODE-ICE has been modified to track the surface temperature, the water thickness and the overall ice thickness during the multi-layer process. This slightly changes the structure of the multi-layer icing simulation as illustrated in Figure 5.1. The icing simulation for the first layer is performed normally (see §2.1.1). Then, following the generation of the new iced geometry, the tracked properties are saved for all the control volumes defining the wall. They are saved in a table against their curvilinear location along the wall. Then the new mesh is created. This process moves the nodes on the wall, hence the saved properties are interpolated over the new nodes distribution via a cubic spline interpolation. The next layer can then be solved with the tracked properties as the initial values.

```
Mesh Generation        Initial parameters
  (NSGRID2D)            and geometry

Interpolation on
the new geometry

Airflow Solver
   (RANS)

Droplets Solver      Heat transfer
  (Eulerian)        and shear stress

Ice Accretion
(Thermodynamics)

  Geometry
  Evolution

 Save data from
 current layer
```
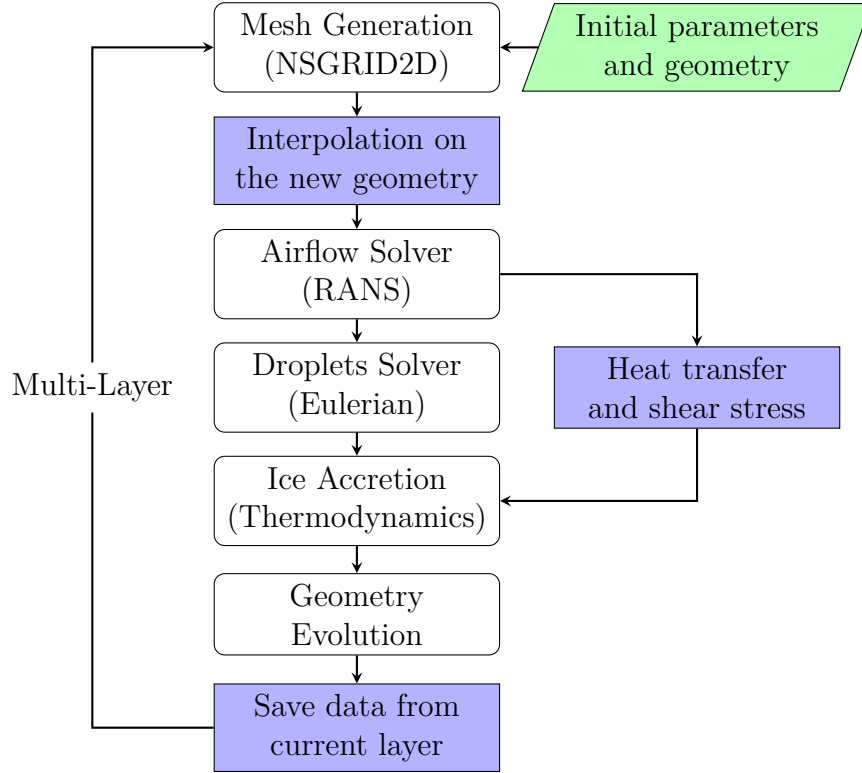
Multi-Layer

Figure 5.1 Multi-layer icing simulation in NSCODE-ICE

5.2 Assessment of the Ice Accretion Results

No official metric is available to determine the error of the ice accretion prediction in comparison to experimental data. The ice shape is typically assessed qualitatively by examining key features:

- the location of the ice limits;
- the location and orientation of ice horns, if any;
- the maximum ice thickness and its location;
- the overall ice shape compared to the experiment.

Furthermore, the experimental error on the tracing of the ice shape and the repeatability of the experiments can be quite large ($\pm 20\%$). For instance Figures 5.10a, 5.10b, 5.11b illustrate the variability of the experimental data over multiple runs at the same icing conditions (labeled Experimental 1, 2 and 3 on the figures). In particular, Figure 5.10b exhibits a large change in ice thickness in the upper ice limits area for the experimental data. Thus, when comparing the numerical results to the experimental ice shape, the variability of the results

have to be kept in mind. In the following sections, a qualitative comparison is performed by examining the ice features listed above.

5.3 2D Icing

A rime ice case and a glaze ice case are selected to demonstrate the multi-layer results of NSCODE-ICE. The simulation parameters are shown in Table A.1 and are taken from Wright et al. (1997). A O-grid with 257 nodes on the wall (i) and 129 nodes in the direction normal to the wall (j) is used. The SA turbulence model is selected with Boeing roughness extension. The convective heat transfer model of §3.1 and the Langmuir D droplet distribution are applied to all the following ice accretion simulations. Unless otherwise specified, the equivalent sand grain roughness of the surface is evaluated with the empirical model of §3.2.

5.3.1 Rime Ice – Case 27

The test case 27 is in full rime ice condition with a low temperature and a relatively low airspeed, thus very little or no runback water is expected for this type of simulation. This is confirmed by observing Figure 5.2 where the limits for collection efficiency (β) match the ice limits. Also, the water film thickness is of the order of 1e-7 in the stagnation point region and 0 everywhere else. The ice shape (Figure 5.3) exhibits no ice horn and the typical bubble-like ice shape is observed for the single layer simulation. The upper and lower ice limits match the experimental results and the maximum ice thickness in the x direction is similar to the experiment. However the ice is too thick when following the y direction. This is typical of single layer rime ice simulation.

For the 5 layers simulations, the ice limits and the maximum ice thickness in x are respected. Moreover, the ice thickness in y is in much better agreement with the experimental data. By increasing the number of layers, the ice shape is similar to the previous results but with further reduction in the ice thickness following the y direction.

In theory, the more icing layers are added, the closer to the reality the result should be. Hasanzadeh et al. (2013) showed that 40 to 60 layers are required to reach a state where the change in ice shape is not significant. In practice (e.g. Wright et al. (1997)), a lower number of layers (e.g. 4-5 layers) is used and fair results are obtained since the surface roughness is tuned accordingly. Considering the results of NSCODE-ICE for case 27, best results are achieved using the 5 layers simulation, not 20 layers. It suggests that the current model does not correctly represent the real physics of the problem. The roughness model is a probable cause since it was calibrated for 1st generation icing softwares.
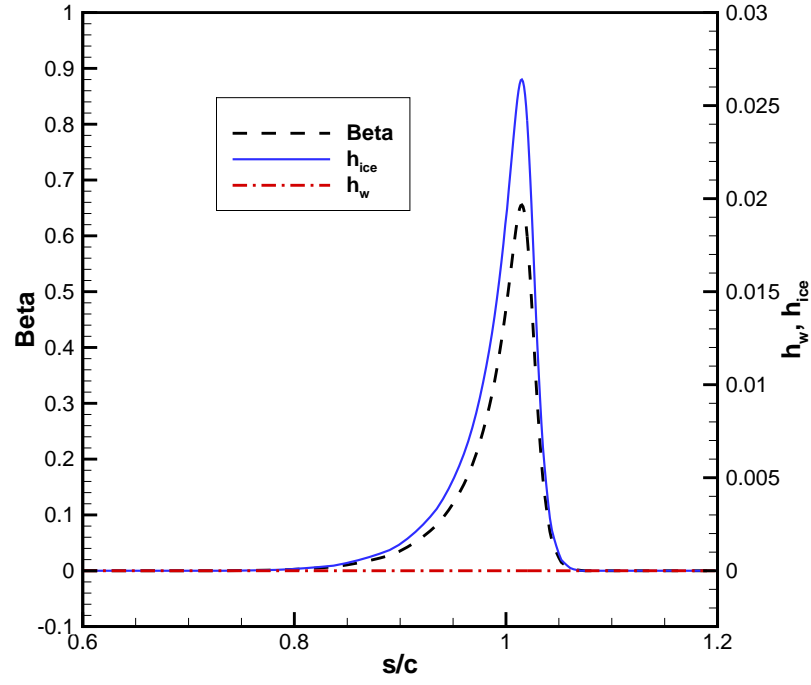
Figure 5.2 Collection efficiency (β) for the rime ice case 27 – 1st layer
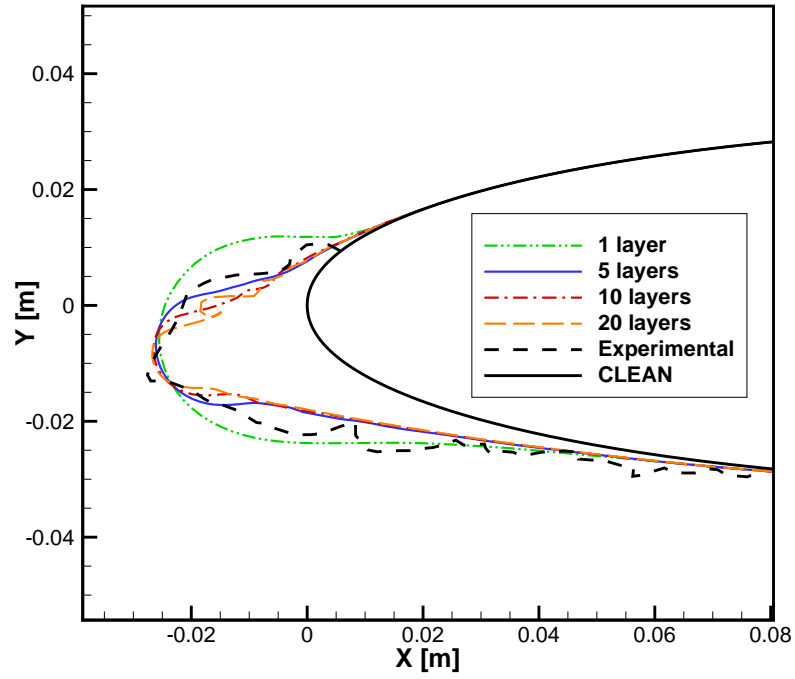
Figure 5.3 Multi-layer results for the rime ice case 27

5.3.2 Glaze Ice – Case 31

This test case is at warm temperature $(269.1K)$ and at relatively low velocity, leading to glaze ice conditions. A moderate ice horn is observed on the upper surface for the experimental ice shape (Figure 5.4).

Considering the single layer simulation, the icing limits on both the upper and lower are close the the experimental but the result is not as good as for the rime ice case (Figure 5.3). Besides, the ice is too thin in the horn area. The icing limits for a glaze ice case are mostly determined by the behavior of the runback water. The convective heat transfer and the evaporation greatly influence the amount of water that flows and the location where it freezes. These terms are modified by the airflow update in the multi-layer process.

By performing a 5 layers simulation, there is an improvement near the upper ice limit as the ice goes thinner. Moreover, the ice is thicker in the horn area leading to a better match with the experimental results. By increasing the number of layers to 10 and then 20, the ice shape improves further as the ice thickness is reduced in the upper ice limit area. Also, the maximum ice thickness near the horn is in good agreement with the experiment. Finally, the ice limits are improved on the lower surface as well.

Figure 5.4 Multi-layer results for the glaze ice case 31

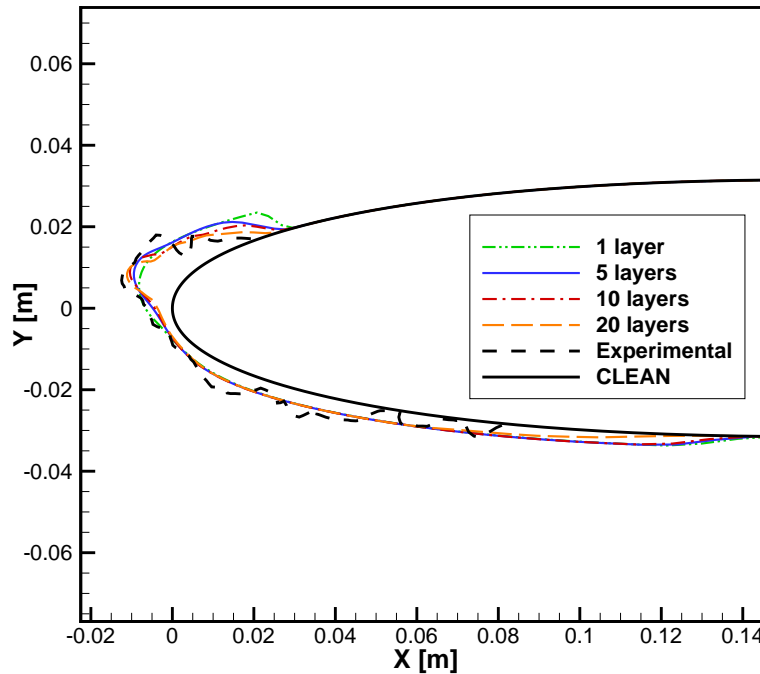In conclusion, the addition of ice layers improves the ice shape prediction significantly for both test cases. For the rime ice case, an optimal number of layers is reached, past which the addition of layers worsen the result. However, this is not true for the glaze ice case, where increasing the number of layers improves the results until the maximum number of layer tested.

5.3.3 Additional 2D Results

Following the observations of the previous section, five layers are used with the multi-layer icing simulation. This allows a fair estimation of the ice shape for both rime and glaze situations while reducing the computation time compared to a 20 or a 40 layers simulation. The test case parameters are again listed in Table A.1.

Figure 5.5 to 5.7 illustrate the ice shapes for cases 27 to 32 taken from Wright et al. (1997). These cases are at the same icing conditions except a change in static temperature ranging from $245.2K$ (rime ice) to $270.2K$ (glaze ice). They are presented in order for increasing temperature. A quick look reveals a good agreement of the overall ice shape against the experimental data for all cases, with better results being achieved with the 5 layers simulation compared to the single layer ice shape. The ice limits are well detected for all cases except for the warmer case (32), where the upper surface shows too much runback water. The same behavior was observed by Wright et al. (1997) when comparing the numerical results of the NASA and ONERA with the experimental shape. Also, cases 28 and 29 exhibits ice horns when there should be none. However the orientation of the horns is close to the orientation of the experimental ice shape.

Again from Wright et al. (1997), Figure 5.8 to 5.9 present ice accretion results for cases 33 through 36, showed in order of increasing temperature (from $242.5K$ to $266.4K$). For these cases the freestream velocity is higher than the previous cases (27 to 32). The ice shapes are again in good agreement compared to the experimental data. The ice horns are following the good orientation and are in the correct location although their height is slightly overestimated. The ice limits are well represented except for case 36 for which the lower surface shows extra runback water. Also, for cases 35 and 36, the ice is too thin on the lower surface where a small ice horn was expected.

Figure 5.10 to 5.12 show the numerical results with the SWIM for cases 401, 403, 405, 421 and 425 which are taken from Wright and Rutkowski (1999). The results are still in good agreement with the experimental data, especially for cases 405, 421 and 425. For case 401, the ice horn follows the correct direction but is too high compared to the experimental ice shape. Considering case 403, ice horns are formed while they should not. However, the

overall ice shape is still in fair agreement with the experiment data.

The results confirm the validity of NSCODE-ICE for a wider range of parameters as the ice shapes are in good agreement for all the test cases. The results could be improved by the use of a surface roughness which is location dependent, as observed on cylinders by Hansman (1989). Furthermore, a constant ice density is used ($\rho_{ice} = 917 \ kg/m^3$) while variable density models are available and more realistic. The ice is usually more compact for glaze ice and this could reduce the maximum height of the ice horns, which were slightly overestimated.
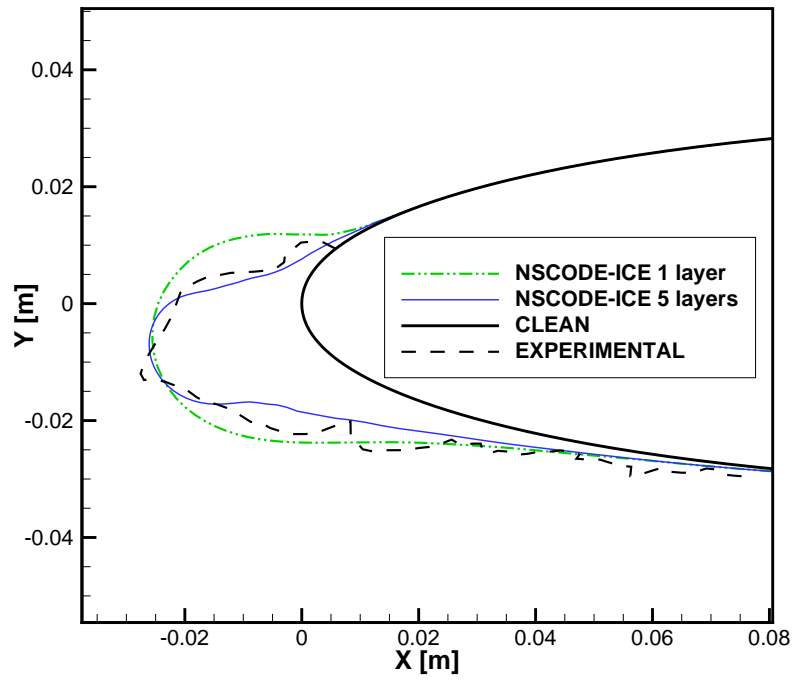
(a) Case 27
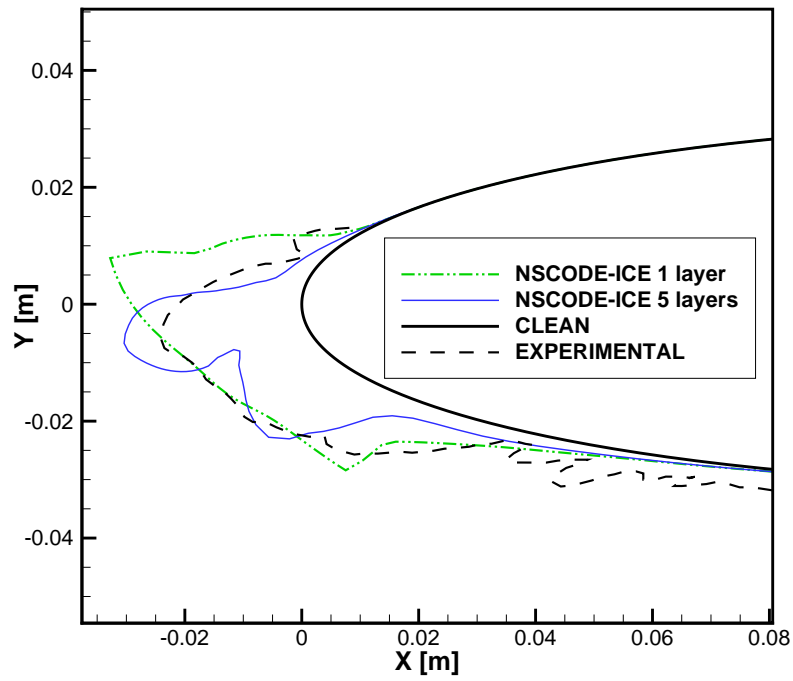
(b) Case 28

Figure 5.5 Ice shape validation with the SWIM – 1 and 5 layers (58 m/s)

(a) Case 29

(b) Case 30

Figure 5.6 Ice shape validation with the SWIM – 1 and 5 layers (58 m/s) (Cont'd)
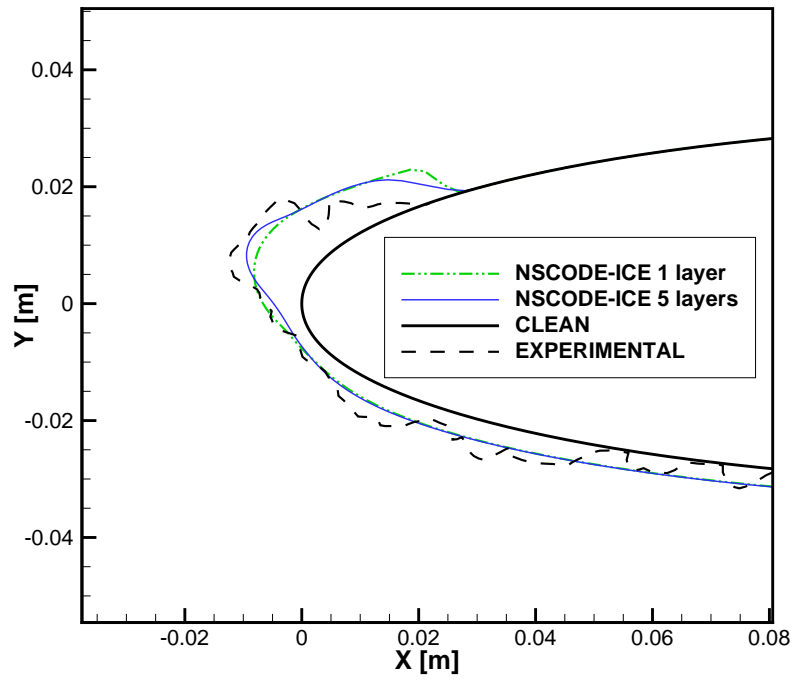
(a) Case 31
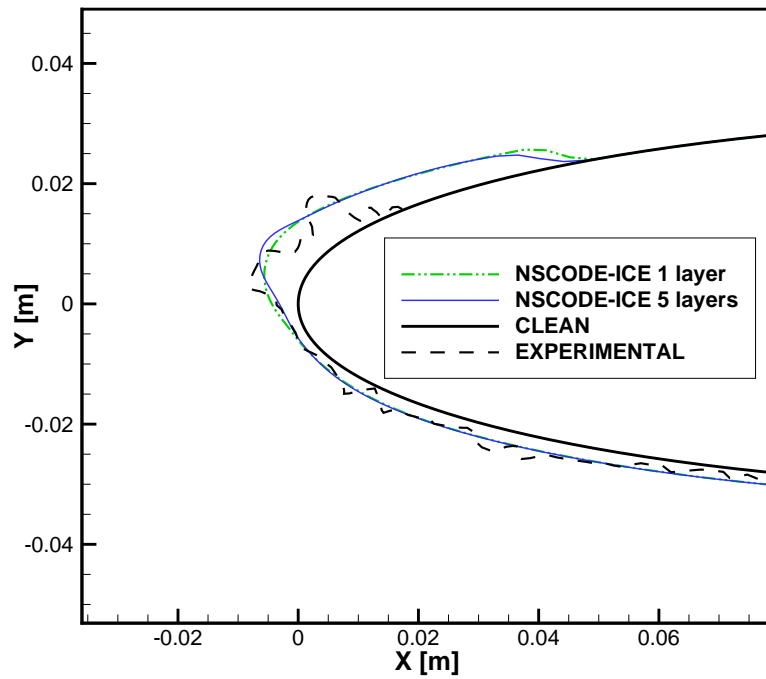
(b) Case 32

Figure 5.7 Ice shape validation with the SWIM – 1 and 5 layers (58 m/s) (Cont'd)
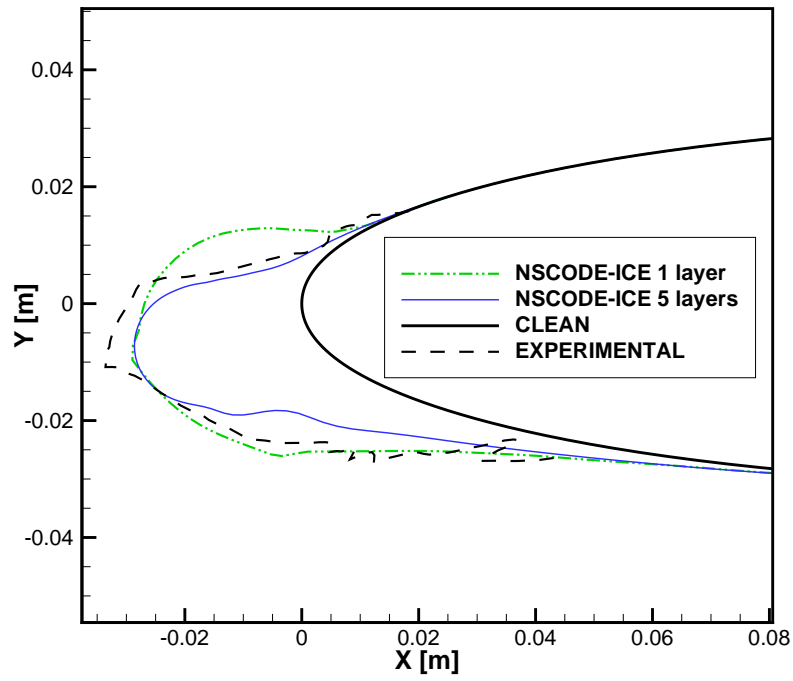
(a) Case 33
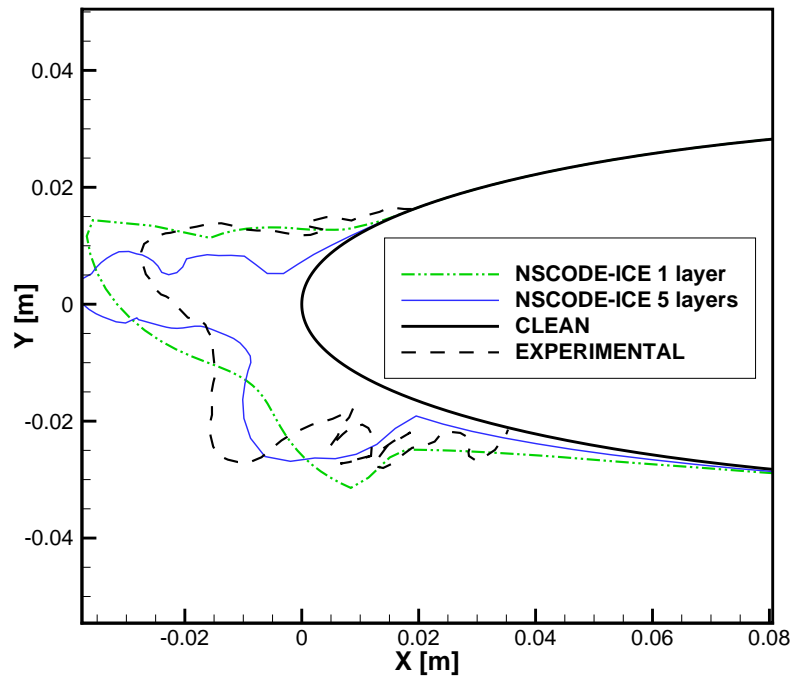
(b) Case 34

Figure 5.8 Ice shape validation with the SWIM – 1 and 5 layers (93.89 m/s)
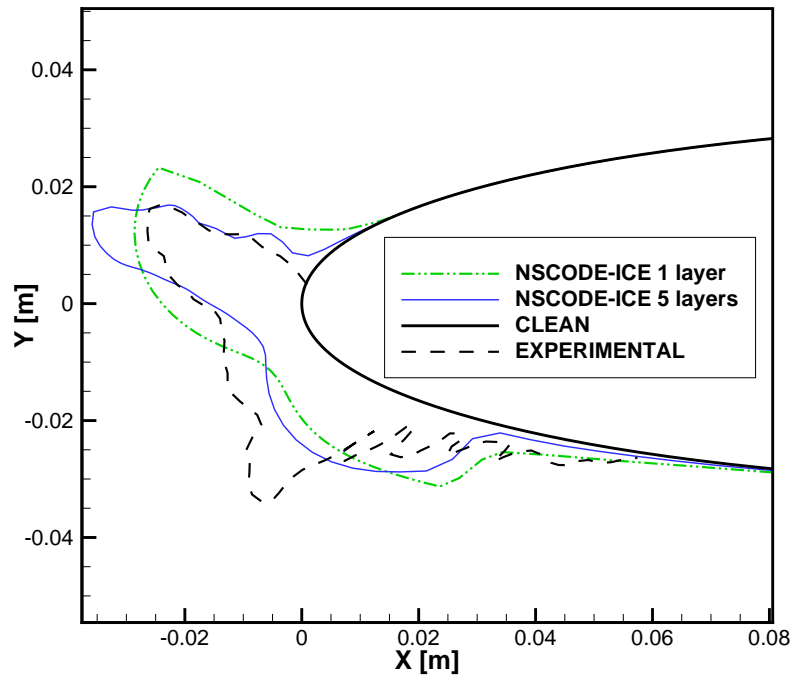
(a) Case 35
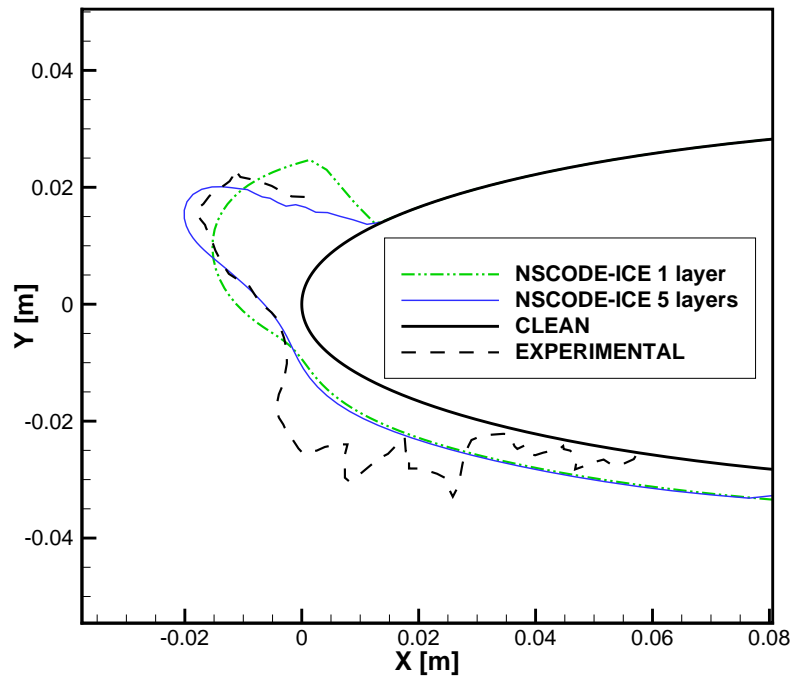
(b) Case 36

Figure 5.9 Ice shape validation with the SWIM – 1 and 5 layers (93.89 m/s) (Cont'd)
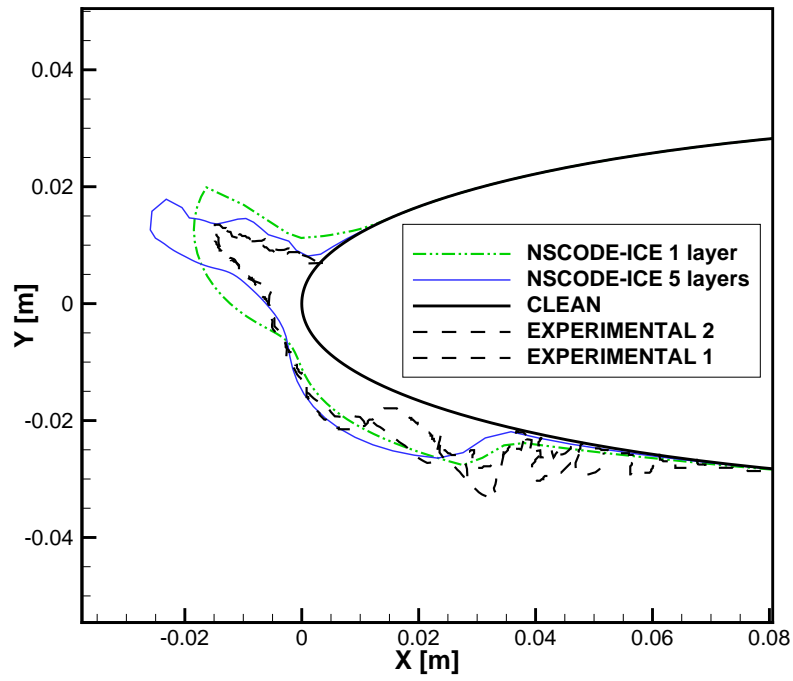
(a) Case 401

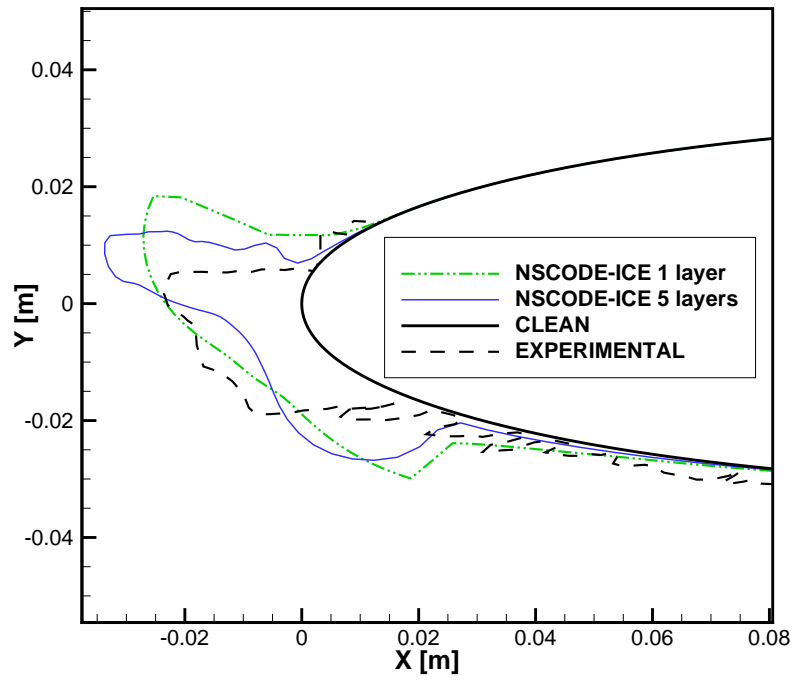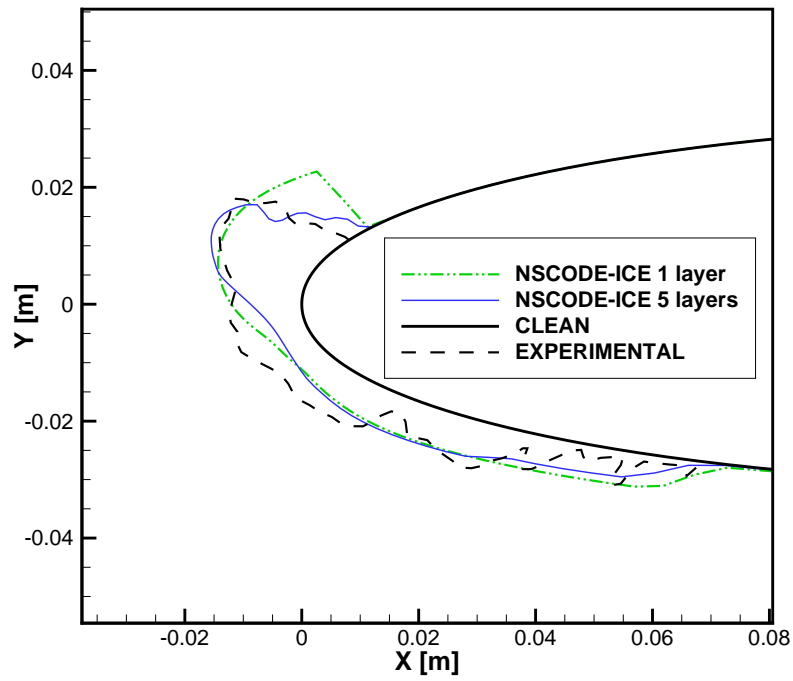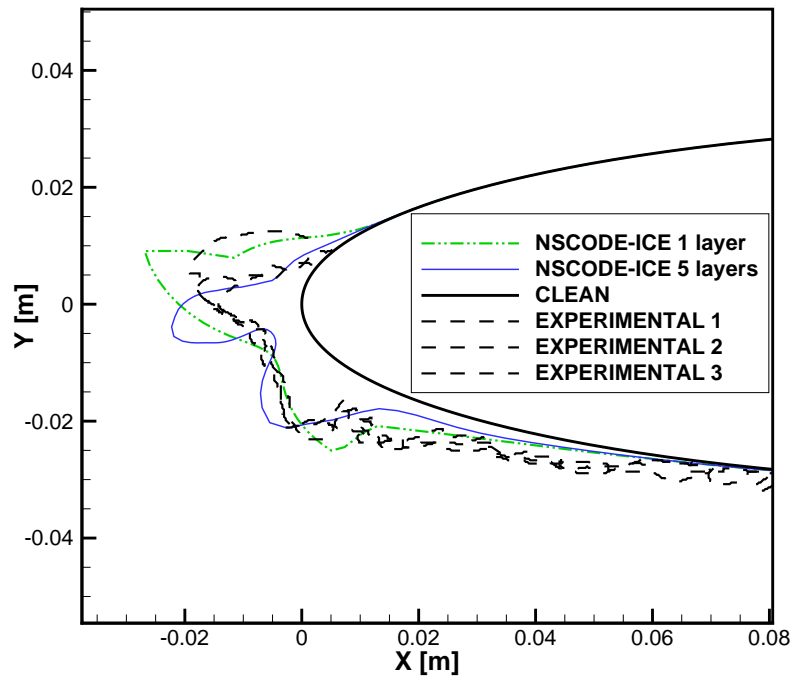(b) Case 403

Figure 5.10 Ice shape validation with the SWIM – 1 and 5 layers (CASE 4XX)
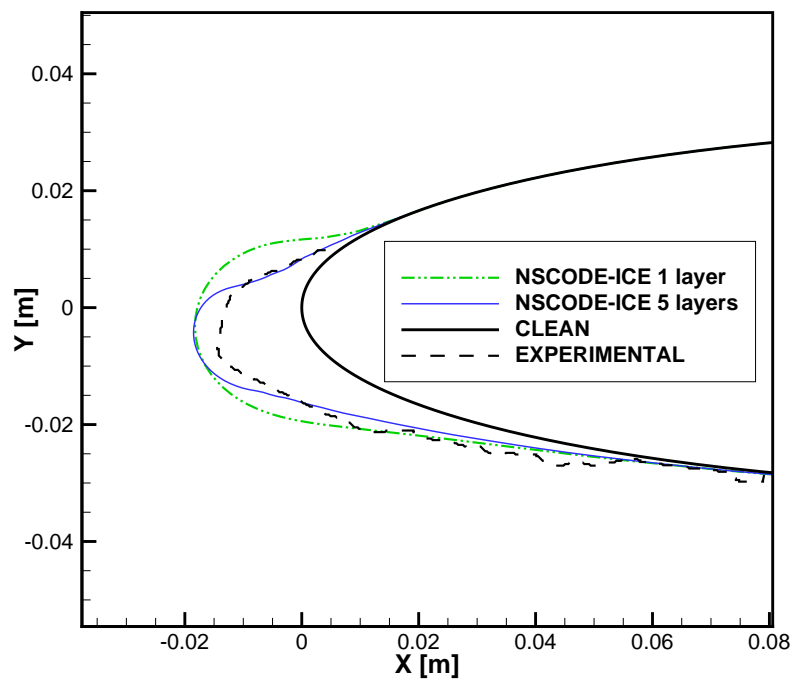
(a) Case 405
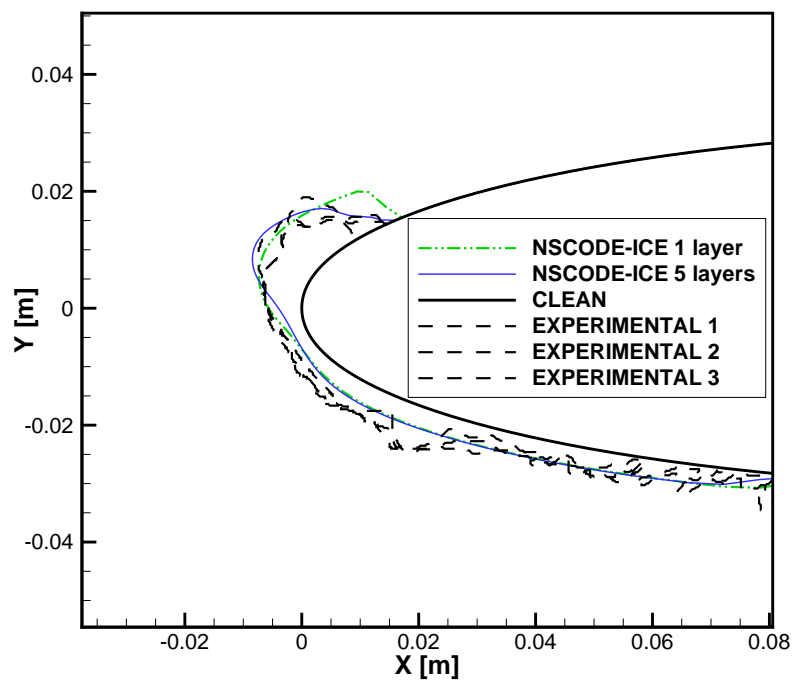
(b) Case 421

Figure 5.11 Ice shape validation with the SWIM – 1 and 5 layers (CASE 4XX) (Cont'd)
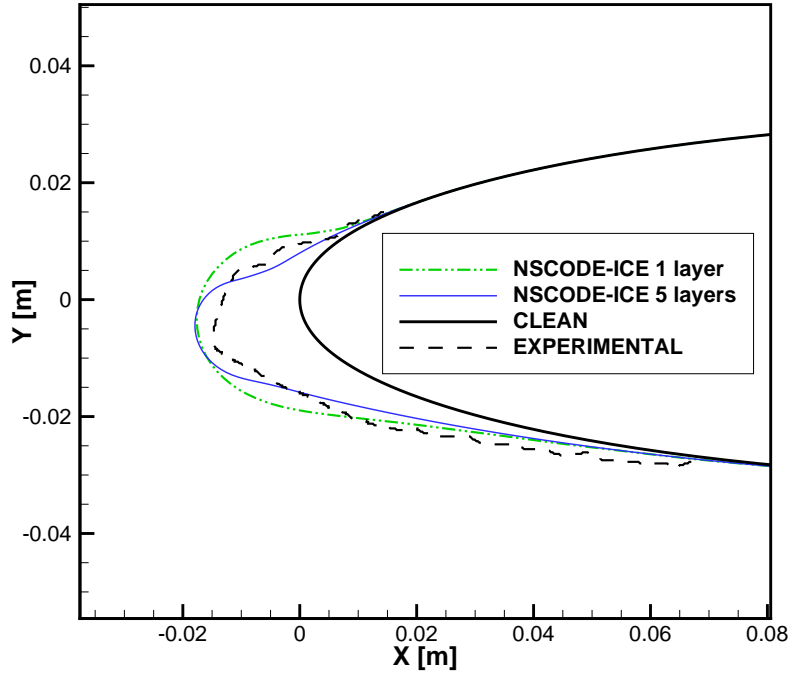
(a) Case 425

Figure 5.12 Ice shape validation with the SWIM – 1 and 5 layers (CASE 4XX) (Cont'd)

5.4 Infinite Swept Wing Icing (2.5D)

This section presents numerical ice shape predictions against experimental results on an infinite MS(1)-317 swept wing with a sweep angle of 30 degrees. The experimental test procedure is outlined by Bidwell (1991), the icing parameters and numerical results from LEWICE are provided by Potapczuk and Bidwell (1991). The geometry is chosen with a sharp trailing edge from Papadakis et al. (2007). The original airfoil points distribution induces oscillation in the Cp curves and therefore in the HTC and predicted ice shape. A smoothed version of the airfoil is used instead. Non-Uniform Rational B-Spline (NURBS) were used to ensure a smooth curvature, leading to smooth ice shapes.

The test case parameters are given in Table A.1. Note that the equivalent sand grain roughness (k_s) is directly provided by Bidwell (1991) and is used for the following simulations. The empirical roughness model of §3.2 was tried only to give a poor estimation of the ice shapes compared to the experimental. Namely, the amount of runback water was too large and the icing limits, too wide. It suggests that the empirical roughness model is not calibrated for swept-wing simulations.

Figure 5.13 illustrates the ice prediction from NSCODE-ICE using both the 2.5D method and the correction of Dorsch and Brun (1953) as reviewed in §2.5. The test case 3 represents a glaze ice situation (warm temperature) with moderate ice accretion concentrated on the leading edge (Figure 5.13a). For both the 2.5D and Dorsch correction methods the ice limits are very similar. However, the limits extend farther then the experiment. Also, for Dorsch method, there is a small concavity close to the stagnation line area which is not present for the 2.5D approach. This is in-line with the behavior described at §3.1.4, where it is mentioned that correction methods based on purely 2D flow solution fail to account for the crossflow in the spanwise direction. Effectively, the HTC is underestimated since the stagnation line is taken as a stagnation point. Although the upper ice limit is not so close from the experiment, the 2.5D method gives a better estimation of the ice shape. It avoids the concave region in the stagnation area by correctly modeling the stagnation line.

Colder conditions are now considered with the test case 7 illustrated in Figure 5.13b. Again, the ice limits are practically identical for the 2.5D and Dorsch methods. Moreover, they match well the experimental results. The maximum ice thickness in the x direction corresponds to the experiment for the 2.5D method, while for Dorsch's approach a concave area is again present in the stagnation area. The overall ice shape is in very good agreement with the experimental data when using the 2.5D approach, since the stagnation line is modeled properly.
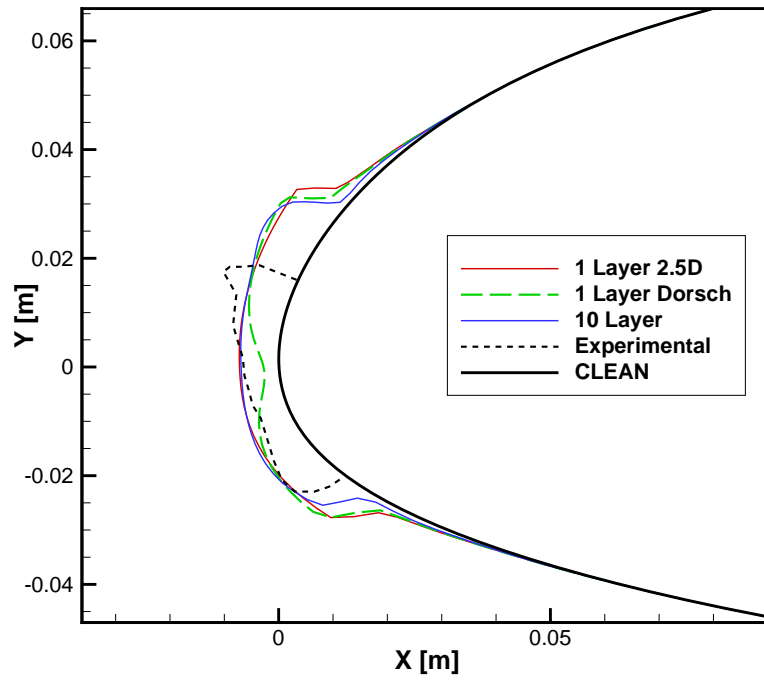
(a) Case 3
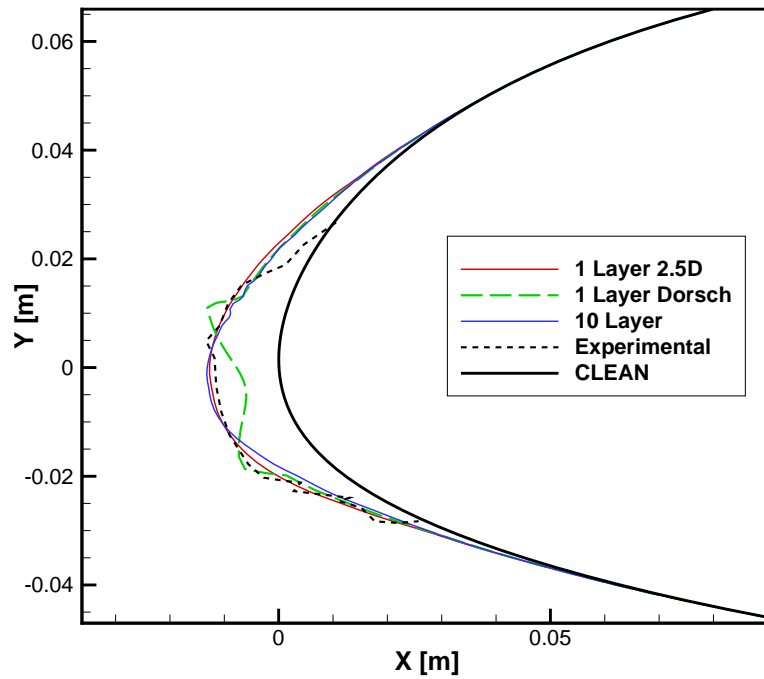
(b) Case 7

Figure 5.13 Ice accretion validation for the MS-317 infinite swept wing

CHAPTER 6   CONCLUSION

The current research project focuses on the development of a thermodynamic model for the evaluation of thin water films on airfoils and on the problem formulation for infinite swept wings. As of 2015, NSCODE-ICE was composed of five modules: a mesh generator (NS-GRID2D), a RANS solver for the airflow (NSCODE), an Eulerian droplets density and velocity field solver, an algebraic thermodynamic solver and a geometry evolution solver. While the mesh generator, flow solver and droplets solver are following the state-of-the art in the field of ice accretion simulations, some improvements were required for the thermodynamic and geometry evolution modules.

6.1   Advancement of Knowledge

In order to correctly model the water film behavior, it is first required to predict the correct ice type for a given set of ambient conditions. For instance, it is not desirable to obtain a typical glaze ice shape (with runback water) in full rime ice condition. The previous version of NSCODE-ICE was having some difficulty to predict the correct ice shape. Hence, modifications are made to solve this issue: an improved evaluation of the convective heat transfer coefficient, the addition of a droplet size distribution to better represent the droplets cloud and an automatic surface roughness modeling. Then the water film behavior was tackled by the implementation of the SWIM. All the modifications are made keeping in mind the methods are to be extended to infinite swept wings computation.

6.1.1   Convective Heat Transfer

The evaluation of the Convective Heat Transfer Coefficient (HTC) was originally done in the thermodynamic module using an Integral Boundary Layer (IBL) method to evaluate the skin friction coefficient. It was modified to take the skin friction coefficient from the RANS solver assuming a fully turbulent flow. This method has been found to underestimate the HTC in the stagnation point area and to overestimate it on the upper surface of the airfoil (for a positive angle of attack).

The method recommended in this thesis is to evaluate the HTC directly from the wall temperature gradient provided by the RANS airflow solver, as proposed by Beaugendre (2003). This method requires a fixed wall temperature boundary condition which was not available. Hence the new boundary condition was implemented, along with a new fixed heat flux boundary

condition. The detail of this work is presented in Appendix B.

Once the boundary condition was implemented, the wall heat flux was extracted from the solution to give the HTC. Since the solution of the HTC depends on the specified wall heat flux, a study has been conducted as to select the right wall temperature for a given case. It has been concluded that the wall temperature (T_{wall}) should be close to T_{rec} while not being too close from it as to avoid oscillations in the solution. It was suggested to use $T_{wall} = 1.05 T_{\infty}$ for the cases presented in this thesis.

The skin friction was verified against empirical relations on rough flat plate. Then, the convective heat transfer was validated on a rough flat plate, and verified on a NACA0012 airfoil. The results agree well with experiments and empirical relations and the stagnation point area is automatically handled with this method. This is a large improvement from the previous implementation, with and even larger benefit if implemented in a 3D code.

Infinite Swept Wing

The prediction of the ice accretion on swept wings is often performed by the use of 2D solvers corrected for the sweep via empirical methods (e.g. (Dorsch and Brun, 1953)). These approaches lack accuracy close to the stagnation area as they model a stagnation point instead of a stagnation line. Proper prediction of the ice accretion on swept wings requires the simulation of the crossflow component of the airflow. The 2.5D approach (Bourgault-Côté et al., 2017) combined with the newly implemented RANS-based HTC evaluation model, accounts for the stagnation line. Therefore, it provides a more representative ice shape in the stagnation region compared to classical methods.

6.1.2   Droplets Modeling

The previous version of NSCODE-ICE was using an Eulerian method to solve the droplet density and velocity field. The solver was designed for a single droplet size, taking the MVD as the running condition. To better represent the reality of a supercooled droplet cloud, a droplet size distribution is implemented. This also allow a better representation of SLD for which the use of a droplet size distribution is required. In line with the modeling of SLD, a new droplet drag model was implemented to account for the deformation of the droplets (from spherical to ellipsoid). These modifications makes for a more general implementation of the droplet field solver and can be seen as a first step towards proper SLD modeling. The reader is referred to Wright (2006), Honsek et al. (2008), Iuliano et al. (2011), Trontin and Villedieu (2016) for more information about SLD and splashing models.

6.1.3 PDE-based Thermodynamic Model

The previous thermodynamic model available in NSCODE-ICE was a basic implementation of the algebraic model of Zhu et al. (2012), referred to as the Iterative Messinger model. This model is a significant improvement over the classical Messinger model since it is no longer stagnation point dependent. However, this model was not capable of representing the water accumulation into a cell, an issue that was fixed. Then, a PDE-based model was implemented as an attempt to model more physics, the SWIM of Bourgault et al. (2000). It is shown that both the SWIM and Iterative Messinger model are giving almost identical results for the cases tested in this thesis. However, since the SWIM is time-dependent and PDE-based, more physics could be modeled including transient phenomena.

6.2 Limits and Constraints

While many improvements are brought to NSCODE-ICE, the new features present some limitations. First, the new method to evaluate the HTC is sensitive to the quality of the grid, the choice of turbulence model and the roughness boundary condition employed. The developments, verification and validation were made for the SA one-equation turbulence model with Boeing's extension for the roughness modeling. These choices might not always be the most appropriate depending on the application. Also, the wall temperature to impose at the wall is not known a priori for this method. A rule of thumb is suggested ($T_{wall} = 1.05T_\infty$) but the best value may vary for different simulation parameters.

Moreover, the roughness greatly influences the value of the HTC. The empirical model currently implemented provide a fair estimate of the equivalent sand grain roughness for the 2D cases presented in this thesis. However, for 2.5D simulations the relation does not seem to be valid since it leads to ice shapes with extended icing limits compared to the experimental data. A higher roughness was used as suggested in the original paper. A model correlating the sweep angle to the equivalent sand grain roughness could be required. Simulations should be performed on a wider range of test cases to verify this hypothesis. Furthermore, the roughness should vary with the location along the surface, a behavior not represented with the current model.

The SWIM was implemented to obtain a general model where more physics could be added. As presently implemented, the SWIM models the same physics as the Iterative Messinger model, with the latter being faster and more robust. Additionally, the SWIM can be quite slow when the convergence criterion is not reached, e.g. when the entire icing time has to be integrated without extrapolating the solution. Furthermore, the SWIM is currently first

order accurate in time and space, which offers poor accuracy for long simulation times. Thus, the implementation of the Iterative Messinger model is recommended, unless transient terms or additional physics is added to the SWIM.

6.3 Recommendations

As the limitations of the current icing software have been discussed in the previous section, solutions are suggested and potential research topics are discussed to improve NSCODE-ICE.

6.3.1 Variable Surface Roughness

The surface roughness model could be improved by the use of a variable surface roughness, which would be more realistic. One approach is to use the bead height to compute the surface roughness. The resulting roughness follow a physical criterion instead of being curve fitted to experimental results. This type of method is used in LEWICE 1.0 (Wright et al., 1997) and was also presented by Fortin et al. (2006), Croce et al. (2010).

6.3.2 Variable Ice Density

In NSCODE-ICE, the ice density is constant over the airfoil surface. However, in reality, the ice density varies and tends to be greater for glaze ice than for rime ice. The use of a variable ice density along the airfoil surface might have a positive effect on the predicted ice shape and should be investigated.

Some icing softwares already incorporate this feature. For instance, Özgen and Canibek (2009) set a different value for rime and glaze ice as shown in Table 6.1.

Table 6.1 Glaze and rime ice densities as defined by Özgen and Canibek (2009)

Ice Type	Criterion	Density
Glaze	$T_{surf} >= T_{ref}$	$917 \ kg/m^3$
Rime	$T_{surf} < T_{ref}$	$880 \ kg/m^3$

Furthermore, FENSAP-ICE (Beaugendre, 2003) uses the Makkonen formula and Macklin R_M parameter to evaluate the ice density. This method provides a variable ice density (in kg/m^3) as a function of the mean droplet radius (r_d in μm), the normal droplet velocity ($u_{d,n}$) and the wall temperature in Celsius (Jones, 1990), (Beaugendre, 2003).

$$R_M = \frac{-r_d u_{d.n}}{\overline{T}}$$

(6.1)

$$\rho_{ice} = \begin{cases} 378 + 425log_{10}(R_M) - 82.3(log_{10}(R_M))^2 & 0.2 < R_M < 170 \\ 917 & otherwise \end{cases} \quad (6.2)$$

Makkonen correlation was calibrated for ice accretion on cylinders and wires. Since in-flight icing is typically simulated at higher velocities, one can argue on the validity of the correlation. Nonetheless, it could provide a good starting point for further investigations.

6.3.3 Droplets Solver and SLD

The droplets size distribution and the droplets deformation are accounted for in the current implementation. However, the splashing phenomenon as well as the droplets breakup and their re-injection have been neglected. These issue should be considered in more details as they have a clear influence over the solution for SLD (Hospers, 2013). Also, with the current implementation, there is no difference between a droplet impacting a dry surface or a droplet impacting a water film. It would be interesting to couple the droplets solver with the thermodynamic solver to include this effect.

6.3.4 Thermodynamic Model

Water accumulation was observed on a manufactured ice shape comprising three ice horns. The water thickness reached a high value which is not representative of the reality. It is suggested to implement an improved thermodynamic model inspired of the work of Myers et al. (2002). The model is more general and could solve the water accumulation issue, since it accounts for the pressure gradients, gravity, surface tension in the water film. It also models the conduction through the ice and water layers. It is therefore recommended to investigate the effect of these new terms in the heat and mass balance for the SWIM.

The SWIM is implemented in an unsteady manner which can lead to a large number of iterations if a long physical icing time is to be simulated. Thus a high order temporal discretization scheme should be considered as to reduce the error on the final solution.

6.3.5 Geometry Evolution

A node displacement method is used for the evolution of the iced geometry in NSCODE-ICE. Since the thermodynamic balances are evaluated along the curvilinear distance, the computed ice thickness does not account for curved bodies. It means that for a standard node displacement method, the ice thickness is overestimated on convex surface and underestimated in concave areas. With this approach, it is also difficult to deal with the geometry clashes (overlapping of the geometry).

It is recommended to implement a new geometry evolution solver that would be mass conservative, deal with geometry clashing automatically and keep the geometry smooth (required for multi-layer icing). The Level-Set method (Rauschenberger et al., 2013), (Pena et al., 2016b) is an interesting candidate. It is a front tracking method which could be used to generate the new ice geometry. Its main advantage compared to a more classical approach is its capacity to handle the overlapping of the geometry automatically (e.g. concave geometry with a high ice accretion rate).

It has been observed that the iced geometry can become rough (oscillating surface) after a few layer of the multi-layer icing process. An auxiliary tool should be created to allow a smoothing of the geometry while keeping the important features of the ice. A mass conservative smoothing would be appropriate. As a starting point, one could consider curvature smoothing via NURBS.

6.3.6 Convective Heat Transfer Coefficient

The evaluation of the convective heat transfer coefficient should be validated on curved bodies such as cylinders and airfoils. NSCODE-ICE was only validated on flat plates and verified on airfoils against LEWICE. Since the HTC is a crucial parameter in the heat and mass balances for ice accretion, it should undergo a thorough validation.

The Prandtl number in NSCODE-ICE is a constant and this model might be improved by the use of different methods like the ones summarized by Yoder (2016). This might affect the behavior of the HTC and should be investigated.

The Spalart-Allmaras turbulence model with Boeing's extension is used for all the results presented in this paper. Although this model is widely used for aircraft application it has not been proven that it is the best turbulence model for icing simulations. For instance two-equations turbulence models like the Menter's $k - \omega\, SST$ (Menter, 1994) should be investigated. Furthermore, the SA model is a fully turbulent model. The use of a model allowing the detection of the laminar-turbulent transition would produce higher quality results in some cases. Hence, different turbulence models should be investigated, especially in terms of heat transfer.

REFERENCES

C. N. Aliaga, M. S. Aubé, G. S. Baruzzi, and W. G. Habashi, "Fensap-ice-unsteady: Unified in-flight icing simulation methodology for aircraft, rotorcraft, and jet engines", *Journal of Aircraft*, vol. 48, no. 1, pp. 119–126, Jan. 2011. DOI: `10.2514/1.C000327`

J. D. Anderson, *Fundamentals of Aerodynamics*, 5th ed. McGraw-Hill, New York, 2011.

B. Aupoix and P. Spalart, "Extensions of the spalart–allmaras turbulence model to account for wall roughness", *International Journal of Heat and Fluid Flow*, vol. 24, no. 4, pp. 454 – 462, 2003, selected Papers from the Fifth International Conference on Engineering Turbulence Modelling and Measurements. DOI: `10.1016/S0142-727X(03)00043-2`

BEA, "On the accident on 1st june 2009 to the Airbus A330-203 flight AF 447 Rio de Janeiro - Paris", Bureau d'Enquêtes et d'Analyses pour la sécurité de l'aviation civile, Aircraft Accident Report f-cp090601, 2012. Retrieved from URL: `https://www.bea.aero/docspa/2009/f-cp090601.en/pdf/f-cp090601.en.pdf`

H. Beaugendre, "A PDE-based 3D approach to in-flight ice accretion", PhD thesis, McGill University, June 2003. Retrieved from URL: `http://digitool.library.mcgill.ca/webclient/StreamGate?folder_id=0&dvs=1486315257461~532`

C. S. Bidwell, "Icing characteristics of a natural-laminar flow, a medium-speed, and a swept, medium speed airfoil", NASA TM–103693, Tech. rep., 1991, also AIAA Paper 91-0447. DOI: `10.2514/6.1991-447`

J. Blazek, *Computational fluid dynamics: Principles and applications*, 2nd ed. Elsevier, 2005.

Y. Bourgault, H. Beaugendre, and W. G. Habashi, "Development of a shallow-water icing model in FENSAP-ICE", *Journal of Aircraft*, vol. 37, no. 4, pp. 640–646, July-August 2000. DOI: `10.2514/2.2646`

Y. Bourgault, W. G. Habashi, J. Dompierre, and G. S. Baruzzi, "A finite element method study of eulerian droplets impingement models", *International Journal for Numerical Methods in Fluids*, vol. 29, no. 4, pp. 429–449, 1999. DOI: `10.1002/(SICI)1097-0363(19990228)29:4<429::AID-FLD795>3.0.CO;2-F`

S. Bourgault-Côté, "Simulation du givrage sur ailes en flèche par méthodes RANS/eulérienne quasi stationnaires", Master thesis, École Polytechnique de Montréal, 2015. Retrieved from URL: `http://publications.polymtl.ca/1710/`

S. Bourgault-Côté, S. Ghasemi, A. Mosahebi, and E. Laurendeau, "Extension of a two-dimensional navier-stokes solver for infinite swept flow", *AIAA Journal*, vol. 55, no. 2, pp. 662–667, Jan. 2017. DOI: `10.2514/1.J055139`

M. T. Brahimi, P. Tran, and I. Paraschivoiu, "Numerical simulation and thermodynamic analysis of ice accretion on aircraft wings", Ecole Polytechnique de Montreal, Tech. rep., May 1994, final Report C.D.T. Project C159.

Y. Cao and S. Hou, "Extension to the myers model for calculation pf three-dimensional glaze icing", *Journal of Aircraft*, vol. 53, no. 1, pp. 106–116, 2016. DOI: `10.2514/1.C033212`

Y. Cao and J. Huang, "New method for direct numerical simulation of three-dimensional ice accretion", *Journal of Aircraft*, vol. 52, no. 2, pp. 650–659, 2015. DOI: `10.2514/1.C032824`

T. Cebeci and J. Cousteix, *Interactive Boundary-Layer Theory.* Berlin, Heidelberg: Springer Berlin Heidelberg, 2005, ch. 9, pp. 307–343. DOI: `10.1007/3-540-27624-6_9`

T. Cebeci, J. P. Shao, F. Kafyeke, and E. Laurendeau, *Computational Fluid Dynamics for Engineers*, 1st ed. Springer-Verlag Berlin Heidelberg, 2005. DOI: `10.1007/3-540-27717-X`

R. Chauvin, "Un modèle unifié pour les phénomènes de givrage en aéronautique et les systèmes de protection thermiques", PhD thesis, Université de Toulouse, ISAE, 2015. Retrieved from URL: `https://hal.archives-ouvertes.fr/tel-01297308`

R. Clift, J. Grace, and M. Weber, *Bubbles, Drops, and Particles.* Academic Press, New York, 1978.

G. Croce, E. D. Candido, W. G. Habashi, J. Munzar, M. S. Aubé, G. S. Baruzzi, and C. N. Aliaga, "Fensap-ice: Analytical model for spatial and temporal evolution of in-flight icing roughness", *Journal of Aircraft*, vol. 47, no. 4, pp. 1283–1289, Jul.. 2010. DOI: `10.2514/1.47143`

R. G. Dorsch and R. J. Brun, "A method for determining cloud-droplet impingement on swept wings", NACA TN 2931, Tech. rep., Apr.. 1953. Retrieved from URL: `https://ntrs.nasa.gov/search.jsp?R=19810068687`

FAA, *Airworthiness Standards: Transport Category Airplanes*, Federal Aviation Administration Std. Part 25, Appendix C, 2016. Retrieved from URL: `https://www.gpo.gov/fdsys/pkg/CFR-2016-title14-vol1/pdf/CFR-2016-title14-vol1-part25-appC.pdf`

——, *Airworthiness Standards: Transport Category Airplanes*, Federal Aviation Administration Std. Part 25, Appendix O - Supercooled Large Drop Icing Condition, 2016. Retrieved from URL: `https://www.gpo.gov/fdsys/pkg/CFR-2016-title14-vol1/pdf/CFR-2016-title14-vol1-part25-appO.pdf`

G. Fortin, A. Ilinca, J.-L. Laforte, and V. Brandi, "New roughness computation method and geometric accretion model for airfoil icing", *Journal of Aircraft*, vol. 41, no. 1, pp. 119–127, Jan. 2004. DOI: `10.2514/1.173`

G. Fortin, J.-L. Laforte, and A. Ilinca, "Heat and mass transfer during ice accretion on aircraft wings with an improved roughness model", *International journal of Thermal Sciences*, vol. 45, no. 6, pp. 595–606, 2006. DOI: `10.1016/j.ijthermalsci.2005.07.006`

R. Gent, N. Dart, and J. Cansdale, "Aircraft icing", *Philosophical Transactions of the Royal Society of London A: Mathematical, Physical and Engineering Sciences*, vol. 358, no. 1776, pp. 2873–2911, 2000. DOI: `10.1098/rsta.2000.0689`

Hansman, "Investigation of surface water behavior during glaze ice accretion", *Journal of Aircraft*, vol. 26, no. 2, pp. 140–147, 1989. DOI: `10.2514/3.45735`

K. Hasanzadeh, E. Laurendeau, and I. Paraschivoiu, "Quasi-steady convergence of multistep navier–stokes icing simulations", *Journal of Aircraft*, vol. 50, no. 4, pp. 1261–1274, 2013. DOI: `10.2514/1.C032197`

——, "Grid-generation algorithms for complex glaze-ice shapes Reynolds-Averaged Navier-Stokes simulations", *AIAA Journal*, vol. 54, no. 3, pp. 847–860, 2016. DOI: `10.2514/1J054076`

T. Hedde and D. Guffond, "Onera three-dimensional icing model", *AIAA Journal*, vol. 33, no. 6, pp. 1038–1045, 1995. DOI: `10.2514/3.12795`

R. Honsek, W. G. Habashi, and M. S. Aubé, "Eulerian modeling of in-flight icing due to supercooled large droplets", *Journal of Aircraft*, vol. 45, no. 4, pp. 1290–1296, 2008. DOI: `10.2514/1.34541`

M. H. Hosni, H. W. Coleman, and R. P. Taylor, "Measurements and calculations of rough-wall heat transfer in the turbulent boundary layer", *International Journal of Heat and Mass Transfer*, vol. 34, no. 4/5, pp. 1067–1082, 1991. DOI: `10.1016/0017-9310(91)90017-9`

J. Hospers, "Eulerian method for super-cooled large-droplet ice-accretion on aircraft wings", PhD thesis, University of Twente, 2013. Retrieved from URL: `http://doc.utwente.nl/87847/1/thesis_J_Hospers.pdf`

J. Huang, S. Nie, Y. Cao, Y. Yao, and J. Yao, "Multistep simulation for three-dimensinal ice accretion on an aircraft wing", in *AIAA Modeling and Simulation Technologies Conference, AIAA SciTech Forum.* AIAA 2016-1918, 2016. DOI: `10.2514/6.2016-1918`

E. Iuliano, G. Mingione, F. Petrosino, and F. Hervy, "Eulerian modeling of large droplet physics toward realistic aircraft icing simulation", *Journal of Aircraft*, vol. 48, no. 5, pp. 1621–1632, 2011. DOI: `10.2514/1.C031326`

K. Jones, "The density of natural ice accretions related to nondimensional icing parameters", *Quarterly Journal of the Royal Meteorological Society*, vol. 116, no. 492, pp. 477–496, 1990. DOI: `10.1002/qj.49711649212`

R. Kind, M. Potapczuk, A. Feo, C. Golia, and A. Shah, "Experimental and computational simulation of in-flight icing phenomena", *Progress in Aerospace Sciences*, vol. 34, no. 5–6, pp. 257–345, July 1998. DOI: `10.1016/S0376-0421(98)80001-8`

P. Lavoie, E. Laurendeau, D. Pena, and Y. Hoarau, "Comparison of thermodynamic models for ice accretion on airfoils", *International Journal of Numerical Methods for Heat and Fluid Flow*, 2017. DOI: `10.1108/HFF-08-2016-0297`

A. T. Lévesque, A. Pigeon, T. Deloze, and E. Laurendeau, "An overset grid 2D/infinite swept wing URANS solver using recursive cartesian bucket method", in *53rd AIAA Aerospace Sciences Meeting.* AIAA Paper 2015-912, Jan. 2015. DOI: `10.2514/6.2015-0912`

C. Macarthur, J. Keller, and J. Luers, "Mathematical modeling of ice accretion on airfoils", in *20th Aerospace Sciences Meeting*, 1982, orlando, FL, USA. DOI: `10.2514/6.1982-284`

F. R. Menter, "Two-equation eddy-viscosity turbulence models for engineering applications", *AIAA Journal*, vol. 32, no. 8, pp. 1598–1605, 1994. DOI: `10.2514/3.12149`

B. L. Messinger, "Equilibrium temperature of an unheated icing surface as a function of airspeed", *Journal of the Aeronautical Sciences*, vol. 20, no. 1, pp. 29–42, Jan. 1953. DOI: `10.2514/8.2520`

A. F. Mills and X. Hang, "On the skin friction coefficient for a fully rough flat plate", *Journal of Fluids Engineering*, vol. 105, pp. 364–365, September 1983, technical Briefs. DOI: `10.1115/1.3241008`

G. Mingione and V. Brandi, "Ice accretion prediction on multielement airfoils", *Journal of Aircraft*, vol. 35, no. 2, pp. 240–246, 1998. DOI: `10.2514/2.2290`

E. Montreuil, A. Chazottes, D. Guffond, A. Murrone, F. Caminade, and S. Catris, "Enhancement of prediction capability in icing accretion and related performance penalties; part i: Three-dimensional cfd prediction of the ice accretion", in *1st AIAA Atmospheric and Space Environments Conference.* AIAA Paper 2009-3969, June 2009. DOI: `10.2514/6.2009-3969`

T. G. Myers, "Extension of the messinger model", *AIAA Journal*, vol. 39, no. 2, pp. 211–218, Feb. 2001. DOI: `10.2514/2.1312`

T. Myers and J. Charpin, "A mathematical model for atmospheric ice accretion and water flow on a cold surface", *International Journal of Heat and Mass Transfer*, vol. 47, no. 25, pp. 5483–5500, December 2004. DOI: `10.1016/j.ijheatmasstransfer.2004.06.037`

T. Myers, J. Charpin, and C. Thompson, "Slowly accreting ice due to supercooled water impacting on a cold surface", *Physics of Fluids*, vol. 14, no. 1, pp. 240–257, Jan. 2002. DOI: `10.1063/1.1416186`

2D zero pressure gradient flat plate verification case. NASA, Turbulence Modeling Resource. Retrieved from URL: `http://turbmodels.larc.nasa.gov/flatplate.html`

G. Naterer, "Eulerian three-phase formulation with coupled droplet flow and multimode heat transfer", *Numerical Heat Transfer, Part B: Fundamentals*, vol. 43, no. 4, pp. 331–352, 2003. DOI: `10.1080/713836223`

NTSB, "In-flight icing encounter and loss of control, Simmons Airlines, d.b.a. American Eagle flight 4184", National Transportation Safety Board, Aircraft Accident Report NTSB/AAR-96/01, 1996, revised Sept. 2002. Retrieved from URL: `https://www.ntsb.gov/investigations/AccidentReports/Reports/AAR9601.pdf`

S. Özgen and M. Canibek, "Ice accretion simulation on multi-element airfoils using extended messinger model", *Heat and Mass Transfer*, vol. 45, p. 305, Jan. 2009. DOI: `10.1007/s00231-008-0430-4`

M. Papadakis, S.-C. Wong, A. Rachman, K. E. Hung, G. T. Vu, and C. S. Bidwell, "Large and small droplet impingement data on airfoils and two simulated ice shapes", NASA, Tech. rep. TM 2007-213959, 2007. Retrieved from URL: `https://ntrs.nasa.gov/archive/nasa/casi.ntrs.nasa.gov/20070034950.pdf`

D. Pena, Y. Haorau, and E. Laurendeau, "A single step ice accretion model using level-set method", *Journal of Fluids and Structures*, vol. 65, pp. 278–294, Aug. 2016. DOI: `10.1016/j.jfluidstructs.2016.06.001`

D. Pena, Y. Hoarau, and E. Laurendeau, "Development of a three-dimensional icing simulation code in the NSMB flow solver", *International Journal of Engineering Systems Modelling and Simulation (IJESMS)*, vol. 8, no. 2, pp. 86–98, 2016. DOI: `http://dx.doi.org/10.1504/IJESMS.2016.075544`

A. Pigeon, A. T. Levesque, and E. Laurendeau, "Two-dimensional Navier-Stokes flow solver developments at École Polytechnique de Montréal", in *CFD Society of Canada 22nd Annual Conference.* CFDSC, Jun. 2014.

M. Potapczuk and C. Bidwell, "Numerical simnulation of ice growth on a MS-317 swept-wing geometry", NASA TM–103705, Tech. rep., 1991, also AIAA Paper 91-263. DOI: `10.2514/6.1991-263`

W. H. Press, S. A. Teukolsky, W. T. Vetterling, and B. P. Flannery, *Numerical Recipes in C: the art of scientific computing*, 2nd ed. Cambridge [Angleterre]: Cambridge University Press, 1992.

A. Pueyo, "Efficient 3D artificial ice shapes simulations with 2D ice accretion codes using a 3-level correction", in *SAE 2013 AeroTech Congress and Exhibition*, vol. 7. SAE Technical Paper 2013-01-2136, Sep. 2013. DOI: `10.4271/2013-01-2136`

P. Rauschenberger, A. Criscione, K. Eisenschmidt, D. Kintea, S. Jakirlić, Ž. Tuković, I. Roisman, B. Weigand, and C. Tropea, "Comparative assessment of volume-of-fluid and level-set methods by relevance to dendritic ice growth in supercooled water", *Computers & Fluids*, vol. 79, pp. 44–52, 2013. DOI: `http://dx.doi.org/10.1016/j.compfluid.2013.03.010`

J. Shin, B. Berkowitz, H. Chen, and T. Cebeci, "Prediction of ice shapes and their effect on airfoil performance", NASA, Tech. rep. TM–103701, 1991, also AIAA Paper 91-0264. Retrieved from URL: `https://ntrs.nasa.gov/archive/nasa/casi.ntrs.nasa.gov/19910009734.pdf`

D. Silva, T. Bortholin, J. A. Lyrio, and L. Santos, "Parametric evaluation of icing effects by a quasi-3d methodology for high-lift configurations", in *SAE 2015 International Conference on Icing of Aircraft, Engines, and Structures.* SAE Technical Paper 2015-01-2083, 2015. DOI: `10.4271/2015-01-2083`

P. Spalart, "Trends in turbulence treatments", in *Fluid Dynamics and Co-located Conferences.* American Institute of Aeronautics and Astronautics, Jun. 2000, pp. –. DOI: `10.2514/6.2000-2306`

P. Trontin and P. Villedieu, "Revisited model for supercooled large droplet impact onto a solid surface", *Journal of Aircraft*, 2016. DOI: `10.2514/1.C034092`

P. Verdin, J. Charpin, and C. Thompson, "Multistep results in ICECREMO2", *Journal of Aircraft*, vol. 46, no. 5, pp. 1607–1613, 2009. DOI: `10.2514/1.41451`

W. Wright, P. Struk, T. Bartkus, and G. Addy, "Recent advances in the lewice icing model", in *SAE Technical Paper 2015-01-2094*, 2015, doi:10.4271/2015-01-2094. DOI: `10.4271/2015-01-2094`

W. B. Wright, "User manual for the glenn ice accretion code lewice version 2.2.2", NASA, Tech. rep. CR 2002–211793, 2002. Retrieved from URL: `https://ntrs.nasa.gov/archive/nasa/casi.ntrs.nasa.gov/20020080990.pdf`

W. B. Wright and A. Rutkowski, "Validation results for LEWICE 2.0", NASA, Tech. rep. CR 1999–208690, 1999. Retrieved from URL: `https://ntrs.nasa.gov/archive/nasa/casi.ntrs.nasa.gov/19990021235.pdf`

W. B. Wright, "Further refinement of the LEWICE SLD model", NASA, Tech. rep. CR 2006–214132, 2006, also AIAA Paper 2006–0464. DOI: `10.2514/6.2006-464`

W. B. Wright, R. Gent, and D. Guffond, "DRA/NASA/ONERA collaboration on icing research part II - prediction of airfoil ice accretion", NASA, Tech. rep. CR–202349, May 1997. Retrieved from URL: `https://ntrs.nasa.gov/archive/nasa/casi.ntrs.nasa.gov/19970023937.pdf`

D. Yanxia, G. Yewei, X. Chunhua, and Y. Xian, "Investigation on heat transfer characteristics of aircraft icing including runback water", *International Journal of Heat and Mass Transfer*, vol. 53, no. 19–20, pp. 3702–3707, 2010. DOI: `10.1016/j.ijheatmasstransfer.2010.04.021`

D. A. Yoder, "Comparison of turbulent thermal diffusivity and scalar variance models", in *54th AIAA Aerospace Sciences Meeting.* AIAA Paper 2016-1561, 2016. DOI: `10.2514/6.2016-1561`

C. Zhu, B. Fu, Z. Sun, and C. Zhu, "3D ice accretion simulation for complex configuration basing on improved messinger model", in *International Journal of Modern Physics: Conference Series*, vol. 19. World Scientific, Jun. 2012, pp. 341–350. DOI: `10.1142/S2010194512008938`

APPENDIX A   PARAMETERS FOR THE ICING TEST CASES

Table A.1 Parameters for the icing cases

Case	Geometry	Chord [m]	AoA [°]	Velocity [m/s]	Static Temperature [K]	Static Pressure [kPa]	LWC [g/m³]	MVD [μm]	Icing Time [s]	Roughness (k_s) [μm]
D	NACA0012	0.53	0.0	102.80	228.15	100.00	1.00	20.0	2.0*	10.0*
W	NACA0012	0.53	0.0	102.80	288.15	100.00	1.00	20.0	2.0*	10.0*
M	Manufactured	0.53	0.0	58.10	269.10	95.61	1.30	20.0	480.0	673.2
27	NACA0012	0.53	4.0	58.10	245.20	95.61	1.30	20.0	480.0	124.3
28	NACA0012	0.53	4.0	58.10	253.20	95.61	1.30	20.0	480.0	308.0
29	NACA0012	0.53	4.0	58.10	259.10	95.61	1.30	20.0	480.0	443.5
30	NACA0012	0.53	4.0	58.10	266.30	95.61	1.30	20.0	480.0	608.9
31	NACA0012	0.53	4.0	58.10	269.10	95.61	1.30	20.0	480.0	673.2
32	NACA0012	0.53	4.0	58.10	270.20	95.61	1.30	20.0	480.0	698.5
33	NACA0012	0.53	4.0	93.89	242.50	92.06	1.05	20.0	372.0	76.7
34	NACA0012	0.53	4.0	93.89	256.40	92.06	1.05	20.0	372.0	469.5
35	NACA0012	0.53	4.0	93.89	260.80	92.06	1.05	20.0	372.0	593.8
36	NACA0012	0.53	4.0	93.89	266.40	92.06	1.05	20.0	372.0	752.0
401	NACA0012	0.53	3.5	102.80	265.37	100.00	0.55	20.0	420.0	756.5
403	NACA0012	0.53	3.5	102.80	262.04	100.00	0.55	20.0	420.0	658.0
405	NACA0012	0.53	3.5	102.80	250.37	100.00	0.55	20.0	420.0	312.9
421	NACA0012	0.53	3.5	67.10	268.40	100.00	1.00	20.0	360.0	695.0
425	NACA0012	0.53	3.5	67.10	244.51	100.00	1.00	20.0	360.0	114.7
Infinite Swept Wing ($\Lambda = 30.0°$)										
2	MS(1)-317	0.9144	2.0	67.06	268.69	100.00	1.03	20.0	1164.0	8513
3	MS(1)-317	0.9144	2.0	67.06	268.69	100.00	1.03	20.0	390.0	8513
4	MS(1)-317	0.9144	8.0	67.06	268.69	100.00	1.03	20.0	1164.0	8513
5	MS(1)-317	0.9144	8.0	67.06	268.69	100.00	1.03	20.0	390.0	8513
7	MS(1)-317	0.9144	2.0	67.06	253.13	100.00	1.03	20.0	390.0	1756

* Simulation performed over 0.5s, 1.0s, 1.5s and 2.0s; the surface is assumed to be smooth (k_s=1e-5).

APPENDIX B   BOUNDARY CONDITIONS

In NSCODE-ICE, the only wall boundary condition available is an adiabatic wall. New boundary conditions are needed to allow a better evaluation of the convective heat transfer (§3.1). First, a fixed wall temperature boundary condition is implemented then, a wall heat flux boundary condition is added. These two new boundary conditions are required to implement FENSAP-ICE and ONERA approaches. Also, the wall heat flux BC is necessary for anti-icing application. In this section the following definitions apply:

- the indices $a1$ and $a2$ represent the 1st and 2nd cell closest to the wall in the normal direction (in the air domain);

- the indices $h1$ and $h2$ are the 1st and 2nd halos;

- variables with an overbar $\overline{(\cdot)}$ are non-dimensional.

Figure B.1 illustrates the cell in the computational domain and the halos with respect to the wall.
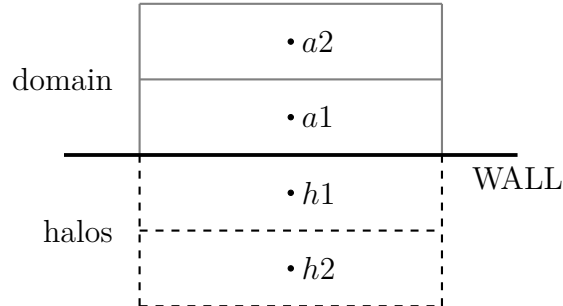

Figure B.1 Arrangement of the cells for the boundary conditions

Only the pressure, density and temperature will be covered here since only these variables are modified for the new boundary conditions. The remaining variables are treated normally (see for instance Blazek (2005)).

B.1 Non-Dimensionalisation in NSCODE

$$\overline{U} = \frac{U}{\sqrt{RT}} = \sqrt{\gamma} Mach \tag{B.1}$$

$$\overline{P} = \frac{P}{P_\infty} \tag{B.2}$$

$$\overline{\rho} = \frac{\rho}{\rho_\infty} \tag{B.3}$$

$$\overline{T} = \frac{\overline{P}}{\overline{\rho}} \tag{B.4}$$

B.2 Adiabatic Wall (_WAL) Boundary Condition

Pressure   A zero pressure gradient normal to the wall is applied (from the boundary layer theory).

$$\frac{\partial P}{\partial \vec{n}} = 0 \tag{B.5}$$

To respect this condition the 2 layers of halos are set as follows:

$$\overline{P}_{h1} = \overline{P}_{h2} = \overline{P}_{a1} \tag{B.6}$$

Temperature (or Density)   An adiabatic wall implies a zero temperature gradient normal to the wall.

$$\frac{\partial T}{\partial \vec{n}} = 0 \tag{B.7}$$

Which means the halos are to be set as follows:

$$\overline{T}_{h1} = \overline{T}_{h2} = \overline{T}_{a1} \tag{B.8}$$

In terms of conservative variables, the density (ρ) is set in the halos to impose the adiabatic wall. Applying Eqs. (B.4) and (B.6), the new boundary condition is found.

$$\frac{\overline{P}_{h1}}{\overline{\rho}_{h1}} = \frac{\overline{P}_{h2}}{\overline{\rho}_{h2}} = \frac{\overline{P}_{a1}}{\overline{\rho}_{a1}}$$

$$\overline{\rho}_{h1} = \overline{\rho}_{h2} = \overline{\rho}_{a1} \tag{B.9}$$

Verification The numerical implementation of the adiabatic wall condition is verified by evaluating T_{wall} and Q_{wall} at the end of the simulation using:

$$\overline{T}_{wall} = \frac{\overline{T}_{a1} + \overline{T}_{h1}}{2} \tag{B.10}$$

$$\overline{\dot{Q}}_{wall} = \overline{k}_{wall} \frac{\overline{T}_{wall} - \overline{T}_{a1}}{\overline{d}_{a1}} \tag{B.11}$$

Figure B.2 displays the error for the wall heat flux ($Q_{err} = \overline{\dot{Q}}_{wall} - 0.0$). For the verification the density residual is converged to 10^{-12} and the resulting error is of the order of machine accuracy (10^{-16}) which implies that the implementation of the _WAL boundary condition is correct.
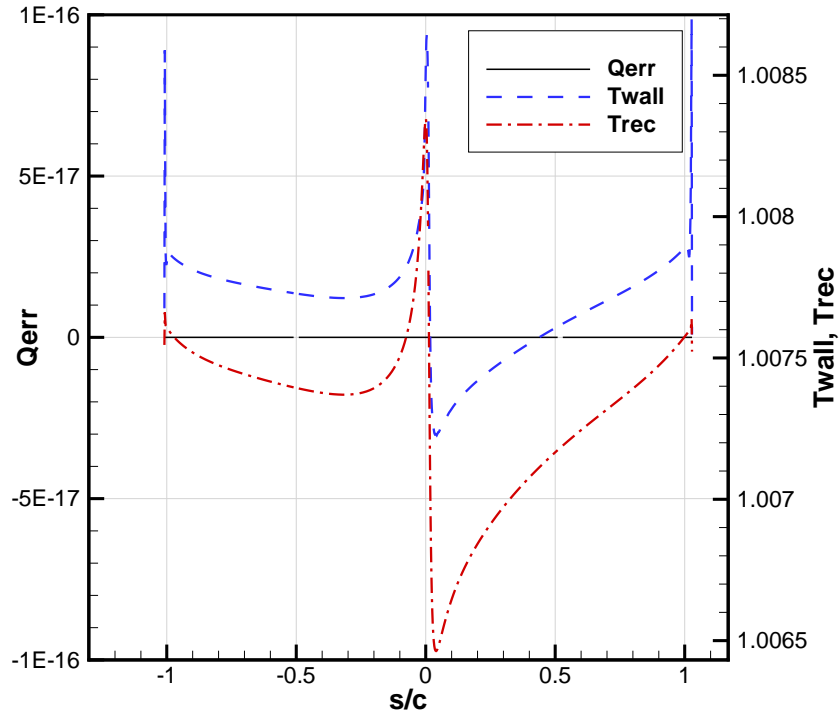

Figure B.2 Verification of the adiabatic wall boundary condition (_WAL)

B.3 Fixed Wall Temperature (_WAT) Boundary Condition

For the fixed wall temperature the pressure is updated as in section B.2. However, the temperature gradient is no longer zero and the wall temperature is know (T_{wall}). The halos

are set by linear extrapolation (Blazek (2005)).

$$\overline{T}_{h1} = 2\overline{T}_{wall} - \overline{T}_{a1} \tag{B.12}$$

$$\overline{T}_{h2} = 4\overline{T}_{wall} - 3\overline{T}_{a1} \tag{B.13}$$

First, Eq. (B.4) is applied.

$$\frac{\overline{P}_{h1}}{\overline{\rho}_{h1}} = 2\overline{T}_{wall} - \frac{\overline{P}_{a1}}{\overline{\rho}_{a1}}$$

$$\frac{\overline{P}_{h2}}{\overline{\rho}_{h2}} = 4\overline{T}_{wall} - 3\frac{\overline{P}_{a1}}{\overline{\rho}_{a1}}$$

Then applying Eq. (B.6), the boundary condition in terms of density is found.

$$\overline{\rho}_{h1} = \frac{\overline{P}_{a1}}{2\overline{T}_{wall} - \frac{\overline{P}_{a1}}{\overline{\rho}_{a1}}} = \left(\frac{2}{\rho_{wall}} - \frac{1}{\overline{\rho}_{a1}}\right)^{-1} \tag{B.14}$$

$$\overline{\rho}_{h2} = \frac{\overline{P}_{a1}}{4\overline{T}_{wall} - 3\frac{\overline{P}_{a1}}{\overline{\rho}_{a1}}} = \left(\frac{4}{\rho_{wall}} - \frac{3}{\overline{\rho}_{a1}}\right)^{-1} \tag{B.15}$$

Verification The numerical implementation of the fixed wall temperature is verified by evaluating T_{wall} at the end of the simulation using:

$$\overline{T}_{wall} = \frac{\overline{T}_{a1} + \overline{T}_{h1}}{2} \tag{B.16}$$

$$\tag{B.17}$$

For the verification, $\overline{T} = 1.05$ is specified at the wall, the error on the wall temperature can be computed from:

$$T_{err} = \overline{T}_{wall} - 1.05 \tag{B.18}$$

The density residual is converged to 10^{-12} and the resulting error is of the order of 4.6×10^{-8} (Fig. B.3), which suggests that the implementation of the _WAT boundary condition is correct.
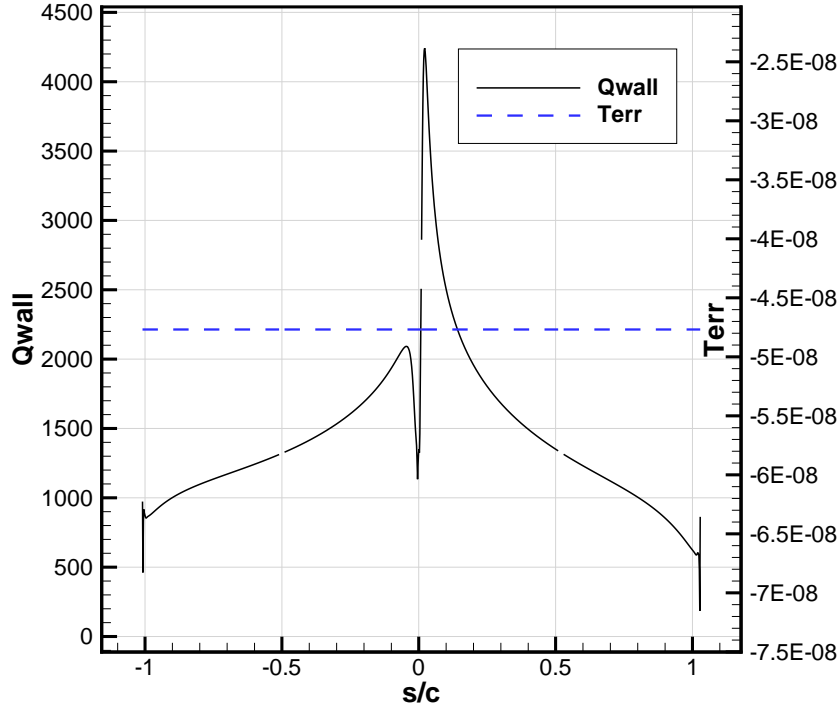
Figure B.3 Verification of the isothermal boundary condition (_WAT)

B.4 Fixed Wall Heat Flux (_WAQ) Boundary Condition

For the fixed wall heat flux the temperature gradient normal to the wall is imposed:

$$\dot{Q}_{wall} = \left(k \frac{\partial T}{\partial \vec{n}} \right)_{wall} \tag{B.19}$$

where k is the conductivity of the air and is computed in non-dimensional form with:

$$\overline{k} = \frac{\gamma}{\gamma - 1} \left(\frac{\overline{\mu}_l}{Pr_l} + \frac{\overline{\mu}_t}{Pr_t} \right) \tag{B.20}$$

$\overline{k}_{wall}$ is computed by averaging the first halo and the first wall cell.

$$\overline{k}_{wall} = \frac{\overline{k}_{a1} + \overline{k}_{h1}}{2} \tag{B.21}$$

The temperature gradient is evaluated by a first order finite difference, hence Eq. (B.19) becomes in non-dimensional form:

$$\overline{\dot{Q}}_{wall} = \overline{k}_{wall} \frac{\overline{T}_{h1} - \overline{T}_{a1}}{2\overline{d}_{a1}} \tag{B.22}$$

where $\overline{d}$ is the non-dimensional cell-centered wall distance. Hence the halo must be set using:

$$\overline{T}_{h1} = \frac{2\overline{d}_{a1}\overline{\dot{Q}}_{wall}}{\overline{k}_{wall}} + \overline{T}_{a1} \tag{B.23}$$

The equation is rewritten in terms of density and pressure by applying Eq. (B.4) and Eq. (B.6):

$$\frac{\overline{P}_{h1}}{\overline{\rho}_{h1}} = \frac{2\overline{d}_{a1}\overline{\dot{Q}}_{wall}}{\overline{k}_{wall}} + \frac{\overline{P}_{a1}}{\overline{\rho}_{a1}}$$

$$\overline{\rho}_{h1} = \overline{\rho}_{a1} \left(\frac{2\overline{d}_{a1}\overline{\dot{Q}}_{wall}\overline{\rho}_{a1}}{\overline{k}_{wall}\overline{P}_{a1}} + 1 \right)^{-1} \tag{B.24}$$

$$\overline{\rho}_{h2} = \overline{\rho}_{a1} \left(\frac{4\overline{d}_{a1}\overline{\dot{Q}}_{wall}\overline{\rho}_{a1}}{\overline{k}_{wall}\overline{P}_{a1}} + 1 \right)^{-1} \tag{B.25}$$

Verification The numerical implementation of the fixed wall heat flux is verified by evaluating T_{wall} and $\dot{Q}_{wall}$ at the end of the simulation using:

$$\overline{T}_{wall} = \frac{\overline{T}_{a1} + \overline{T}_{h1}}{2} \tag{B.26}$$

$$\overline{\dot{Q}}_{wall} = \overline{k}_{wall} \frac{\overline{T}_{wall} - \overline{T}_{a1}}{\overline{d}_{a1}} \tag{B.27}$$

For the verification, the heat flux from the _WAT boundary condition is specified at the wall. In theory the fixed wall temperature from the _WAT boundary condition should be recovered at the end of the simulation, hence the error on the wall temperature can be computed from:

$$T_{err} = \overline{T}_{wall} - 1.05 \tag{B.28}$$

The density residual is converged to 10^{-12} and the resulting error is of the order of 4.6×10^{-8} for the wall temperature and the heat flux is machine accurate (10^{-16}) for the wall heat flux (Fig. B.4), which suggests that the implementation of the _WAQ boundary condition is correct.
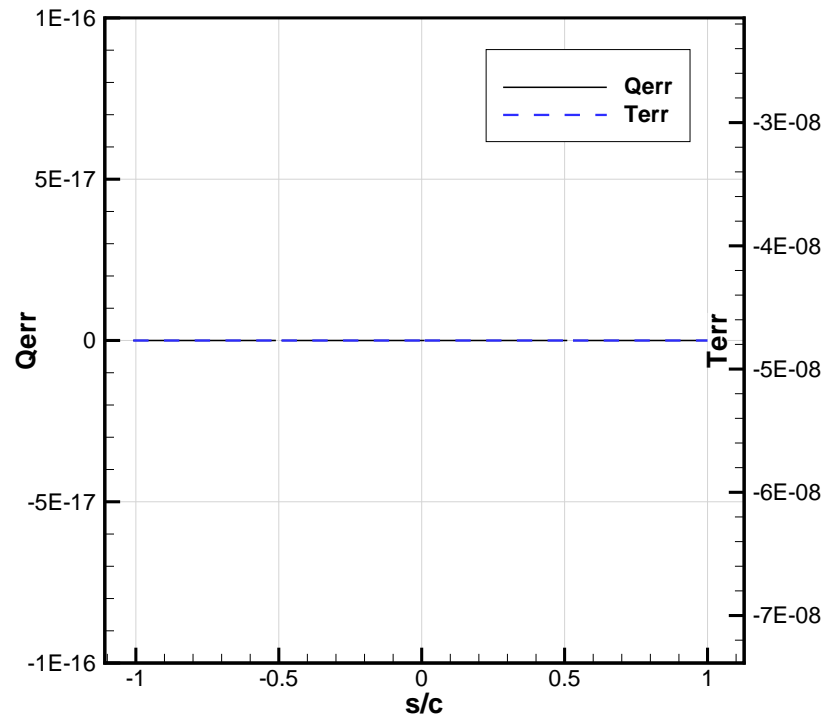
Figure B.4 Verification of the iso-heat-flux boundary condition (_WAQ)